Title
Multiband Circularly Polarized Patch Antenna Array for the Development of Direct-to-Earth Communications (DTE) in Mars Rovers

Author
Santos, Jean Paul Dytioco

Publication Date
2015

Peer reviewed|Thesis/dissertation

University of California
Los Angeles

Multiband Circularly Polarized Patch Antenna Array for the Development of Direct-to-Earth Communications (DTE) in Mars Rovers

A thesis submitted in partial satisfaction
of the requirements for the degree
Master of Science in Electrical Engineering

by

Jean Paul Dytioco Santos

2015

Abstract of the Thesis

Multiband Circularly Polarized Patch Antenna Array for the Development of Direct-to-Earth Communications (DTE) in Mars Rovers

by

Jean Paul Dytioco Santos

Master of Science in Electrical Engineering

University of California, Los Angeles, 2015

Professor Yahya Rahmat-Samii, Chair

Establishing reliable and direct communications links from Earth to Mars rovers, also known as Direct-to-Earth (DTE) communications, is a complex and challenging antenna design problem. The possibility of diminished UHF relay assets for the upcoming Mars 2020 mission requires a high performance antenna array system to enable substantial return of valuable scientific data. This thesis examined various subarray architectures and element geometries, including developing a feasible power dividing stripline network. After this comprehensive examination, a novel lightweight and low-profile X-band single feed circularly polarized antenna subarray comprised of half E-shaped elements is proposed. The proposed design was simulated, prototyped, and measured, showing good agreement between simulation and measurements. The design is also robust, shown by various sensitivity analysis such as the effect of fabrication tolerances. Through this novel design, the challenging NASA DTE system level requirements can be achieved.

The thesis of Jean Paul Dytioco Santos is approved.

Tatsuo Itoh

Yuanxun Ethan Wang

Yahya Rahmat-Samii, Committee Chair

University of California, Los Angeles

2015

To my loving father and mother Joey and Jamie who taught me the value of hard work and performed whatever was necessary to see me succeed in life

To my beautiful and sweet sisters Jacy and Jaylen who always brought a smile to my face when times were difficult

To my caring and dependable brothers Mario and Jimmy who pushed me when I wanted to give up and encouraged me when I lost hope

And to my loving Lord and God Jesus Christ for His everyday strength to make everything I do possible

Table of Contents

List of Figures

List of Tables

Acknowledgments

I would like to acknowledge and thank my valuable friend and colleague Joshua Kovitz from the UCLA Antenna Research, Analysis, and Measurement Laboratory. He has been such a great mentor in helping me understand all of the aspects of antenna design, fabrication, and measurements, especially during the duration of this Masters Thesis. His patience with me is truly commendable, and I truly appreciate his time when I found it difficult to continue. He really exemplifies Ecclesiastes 4:9-10. He has definitely been a great asset in my life and in this valuable field of expertise.

I am also forever thankful to Prof. Yahya Rahmat-Samii's support, wisdom, knowledge, and kindness towards me and helping me become not only a better student but a better engineer. His knowledge of the antenna field is immense, and I'm so thankful he shared and continues to share this wealth of knowledge with me. He has definitely encouraged me to continue to better myself, my community, and my world.

I am also thankful for contributions and assistance of our team at the Jet Propulsion Lab (JPL), specifically Dr. Neil Chamberlain and Dr. Richard Hodges. They have definitely aided in making this project possible and feasible.

CHAPTER 1

Introduction

1.1 Motivation

Space exploration has always been an exciting part of human evolution. Mankind has always sought to investigate the vast universe that surrounds the planet Earth. From Neil Armstrong's famous walk on the moon to the various NASA Apollo missions, space missions have been a great asset in understanding the world. Because of the nature of space exploration, novel technologies have been developed to necessitate these missions. One of those technologies have been in the area of wireless communications. Communications enable the transfer of data from one remote location to another without the physical presence of humans. Rather, communication systems allow space explorations to be achieved through the use of computers and robotics. More importantly, these can be supervised by engineers and scientists here on Earth without the need to launch astronauts into space.

Lately, NASA has relied on robotics such as rovers, shown in Figure 1.2, to capture scientific data through the use of a UHF antenna that communicate with an intermediate relay such as Mars Odyssey [1], shown in Fig. 1.1a. Currently, Mars rover transfer data at a rate of about 3-12 kbps [2]. Mars Odyssey, then sends the vast amounts of scientific data, at a maximum rate of 128 kbps, back to Earth through an X-band link. Through this process, the orbiter can only receive information from the Mars rover for 8 minutes a day. Because of this, only about 6 Mb of data can be received. The orbiter, on the other hand, can transmit information back to Earth for only about 16 hours a day. Any possible direct communication, shown in Fig. 1.1b, between the Mars rover and Earth

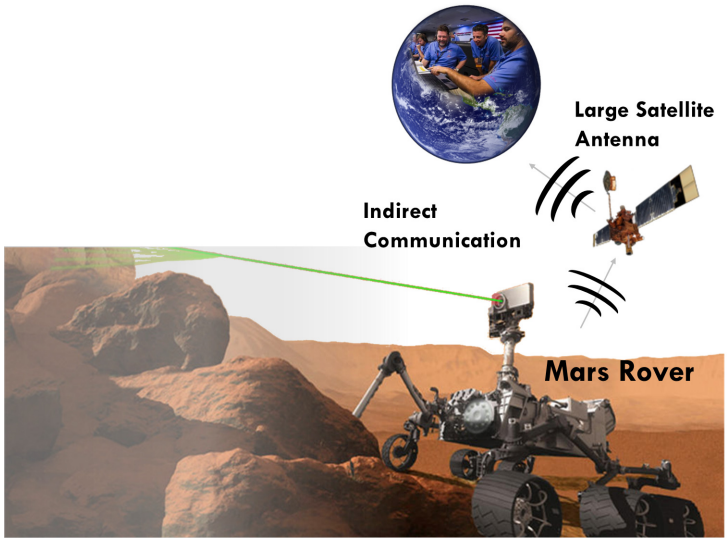

(a) Current Indirect Communication

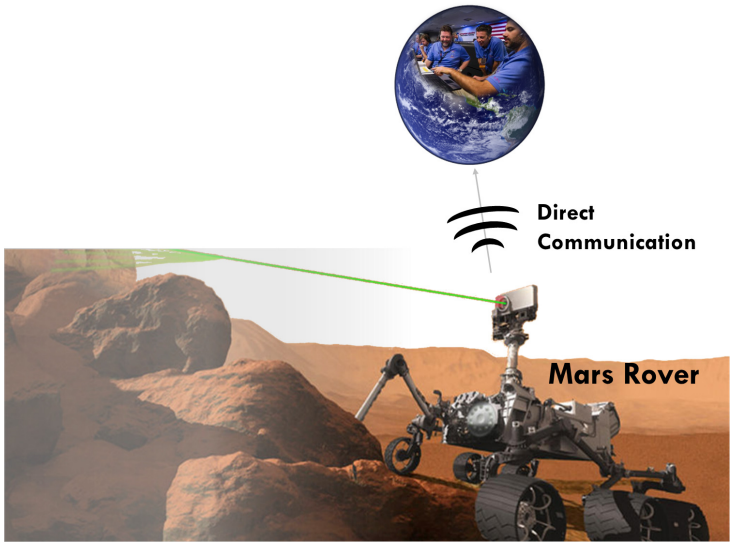

(b) Proposed Direct Communication

Figure 1.1: Courtesy NASA/JPL-Caltech. Currently, the Mars rover utilizes a intermediate relay (a) to transfer the data back to Earth. The proposed system (b) would allow the Mars rover to directly communicate to Earth.

can occur only 3 hours a day [2]. Because of growing technology, future Mars missions, such as Mars2020, may remove the need to use of these intermediate relays and utilize Direct-to-Earth (DTE) communications as its primary link instead. Another important reason to develop such technology is that these orbiting relays may become unavailable and non-existent in future missions. This augmented DTE capability would allow reliable

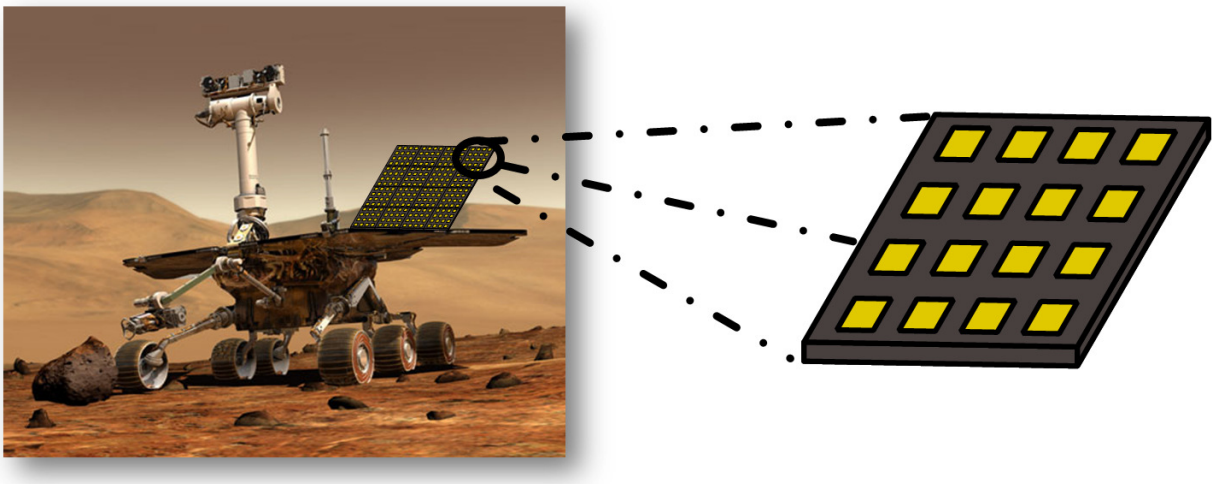

Figure 1.2: Courtesy NASA/JPL-Caltech. The goal of this thesis is to develop a compact antenna that can be used to augment current communications systems on Mars rovers to allow Direct-to-Earth communications. Above is a conceptualization of a possible antenna design that can be used.

transmission of valuable scientific data to Earth in the scenario that UHF orbiting assets are no longer available. However, current DTE capabilities are not very reliable, often containing high signal-to-noise ratios (SNR) variations on the order of 20 dB, preventing high volume returns of scientific data [3]. To facilitate such a reliable high data rate return to Earth from Mars similar to that of the orbiting relays, new high performance antenna designs must be investigated. The ability to communicate directly to Earth from a Mars rover is a challenging design problem.

1.2 JPL Mars Rover Goals and Specifications

In this thesis, the goal is to develop, design, and prototype a novel patch antenna element sub-array that can be integrated into an antenna array architecture that can be used to support DTE high data rate radio communications for future Mars rovers. The use of an array architecture, shown in Fig. 1.2, will enable improved directional characteristics than what would be obtained from single elements [4]. In addition to high gain benefit, an array

architecture allows a compact and simple to fabricate design that can be manufactured using printed circuit board (PCB) technology without the use of hand assembly. This advantage allows such a key component in the Mars Rover to be assembled easily that reduces risk in a future flight development. Moreover, this novel antenna, must have higher power handling than the current X-band high gain antennas on rovers such as Curiosity. In addition to this design challenge is the need to obtain a dual band circularly polarized antenna array. The circular polarization property of the antenna will allow a stable link between the transmitter and the receiver, overcoming possible polarization mismatches. This also helps avoid antenna polarization misalignments that can attenuate signal strength. Finally, beam steering will be achieved mechanically, through the use of a gimbal on the Mars rover antenna assembly.

In past NASA Mars missions, various frequency bands have been used. The two bands of interest that have been used for Mars Rovers are UHF and X bands. The X band is typically composed of two 50 MHz allocations, one defined around 7.2 GHz while the other at 8.4 GHz. The reason for this particular choice of frequency band is because it is the most used frequency in a majority of existing and planned deep space missions between spacecraft and Earth [5]. The superiority of the use of the X-band for direct-to-Earth communications has been shown in [5] which concluded that although UHF will be used as a primary link between local communications at Mars, large landers and rovers should utilize a X-band communications for high-rate local return links. Using the X-band, the transmit band is 8390 MHz to 8460 MHz (0.8% bandwidth at 8425 MHz) while the receive band is 7144 MHz to 7191 MHz (0.66% bandwidth at 7167 MHz). This requirement can be supported through the use of either dual band or wide band CP antennas. For a dual band antenna, that means that the frequency ratio between the TX and RX frequencies is 1.175. For a wide band antenna, that means that the total axial ratio (AR) and S_{11} bandwidth must be 16.8%. In either case, a good bandwidth, which includes both axial ratio and S_{11}, is achieved when the axial ratio is below 3 dB and the S_{11} is lower than -10 dB [6] simultaneously within the required frequenecy band. In this specific antenna,

the S_{11} at the TX band, must be below -15 dB to ease link budget requirements, such as transmit power, from the rover back to Earth.

Another important specification is the physical footprint of the antenna. Per physical area requirements, the antenna must be no greater than 38 cm by 38 cm by 5 cm in size. This means that at the RX frequency of 7.167 GHz, the size in wavelengths is 9.05λ by 9.05λ by1.19λ. At the TX frequency of 8.425 GHz, the size in wavelengths is 10.72λ by 10.72λ by 1.41λ. At first approximation, the effective area of an antenna is just assumed to be equivalent to the physical area of the antenna. This is appropriate when assuming the aperture efficiency is 100%. Therefore, it can be assumed that the directivity can be calculated through the use the antenna's physical area. As [7] states, the effective aperture area is the "ratio of the available power at the terminals of a receiving antenna to the power flux denesity of a plane wave incident on the antenna from that direction. The direction of maximum radiation intensity is implied." Because of this idea, the directivity can be calculated without prior knowledge of the electric and magnetic field distribution of an antenna through the use of the following equation 4.1,

$$D_0 = \frac{4\pi A_{em}}{\lambda^2} \tag{1.1}$$

where A_{em} is the effective area of the antenna, λ is the wavelength, and D_0 is the directivity. Using this formula in 4.1, the above specified physical antenna dimension can produce a maximum directivity D_0 = 30.57 dB at the RX frequency and a maximum directivity D_0 = 32.05 dB at the TX frequency.

Moreover, the radiation pattern specifications include that the antenna must be right hand circularly polarized (RHCP), with a gain of at least 30dBic. The half power beamwidth (HPBW) has to be approximately 4^o. Other specifications include a 100W power handling capability and a partial pressure requirement of 10 Torr to handle external pressures from the Mars atmosphere.

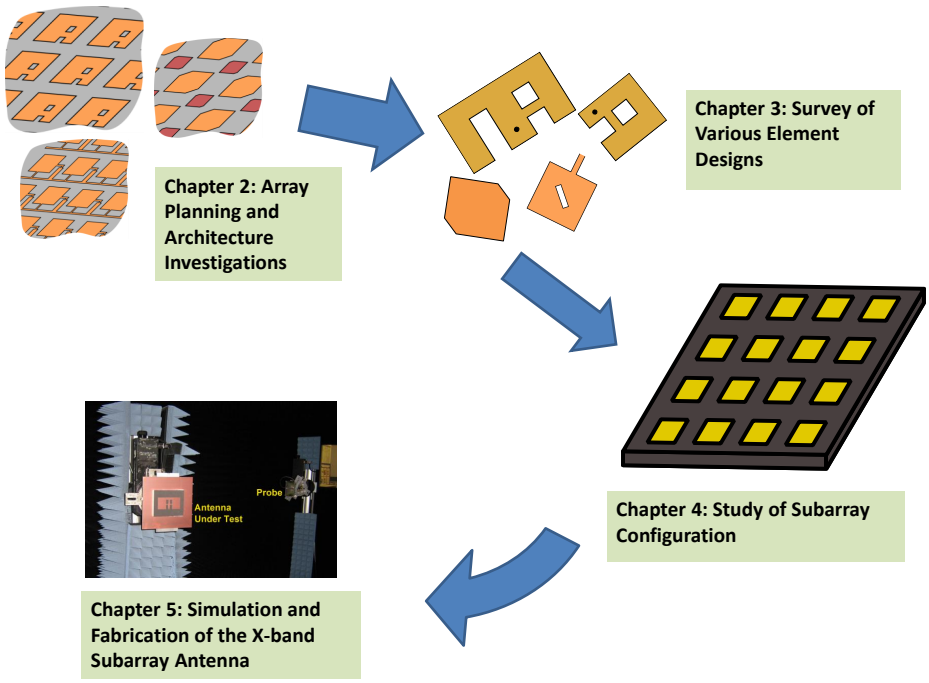

Figure 1.3: The organization of the thesis where each chapter addresses each major task of the thesis in developing a novel antenna array to support DTE Mars Rover communications.

1.3 Research Outline and Tasks

In order to facilitate this thesis, the tasks are divided into several tasks shown in Figure 1.3. The first part of the thesis is to investigate various array architectures and determine which of the array environments would support the required antenna characteristics. This investigation will require studying feed network layouts, choosing proper substrate material, determining how to properly assemble and layer the final prototype. Next, various potential element designs will be reviewed to see which can be best incorporated into an array environment to satisfy requirements. This review will include the U-slot antenna [8–10], E-shaped [11–17], L-shaped probe [18–20], and half E-shaped [21, 22] antennas. Other mechanisms to improve the antenna's performance and bandwidth such as corner truncation [23], the novel annular ring gap method [24, 25] will also be studied in these element candidates for an array. After this investigation, the subrrray configuration

will be chosen. In this section, the radiation pattern specifications will be discussed in depth along with delineating how to properly choose the subarray configuration [26]. Three possibilities are included in this investigation: 3x3, 3x3 without center, and 4x4 subarray. The chosen subarray architecture will then be examined through a traditional array theory analysis. This will be followed by a rigorous full-wave simulation using Ansys HFSS [27] and a discussion of its results. The antenna is then fabricated and measured using equipment available at UCLA's Center for High Frequency Electronics (UCLA CHFE). Simultaneous to the feed network/subarray architecture study, the chosen antenna element will be placed in an array environment and optimized using Particle Swarm Optimization [28–30]. The last task will be to simulate, fabricate, prototype, and assemble the final subarray that contains both the feed network and the element array. In order to complete this study and assembly, a comprehensive sensitivity analysis on the subarray antenna will be performed. This thesis will be concluded through a thorough discussion of the final prototype's specifications and future mission goals.

CHAPTER 2

Array Planning and Architecture Investigation

2.1 Modularization of the Array

The first task in this thesis is to determine the best array architecture that achieves high gain, high power handling, dual band, and circular polarized performance within a compact assembly. In general, large arrays are often difficult to design, simulate, and fabricate due to the large electrical size of the architecture. One technique to avoid this difficulty is to subdivide the array into several subarrays to create a design and assembly that is both simple and modular. Figure 2.1 presents the large array divided into subarrays. In this work, it is assumed that each subarray will be fed via a coaxial/probe connection. Within each subarray, a corporate waveguide feed network will divide the power to each subarray element.

2.2 Layer Architecture

The actual layering of the subarray prototype, shown in Figure 2.2, will have a separate feed network from the antenna layer. A coaxial interconnect is used to connect the feed network to the coaxial line connected from waveguide network. The elements are then connected using a via to the actual feed network. The maximum total prototype height will be $h_t \leq 3$ cm. A similar layer stackup with a simple feeding structure can be used to test this design both in simulation and fabrication. While the testing architecture is shown on a 4x1 subarray, this architecture can be extended to a 2x2 array with different

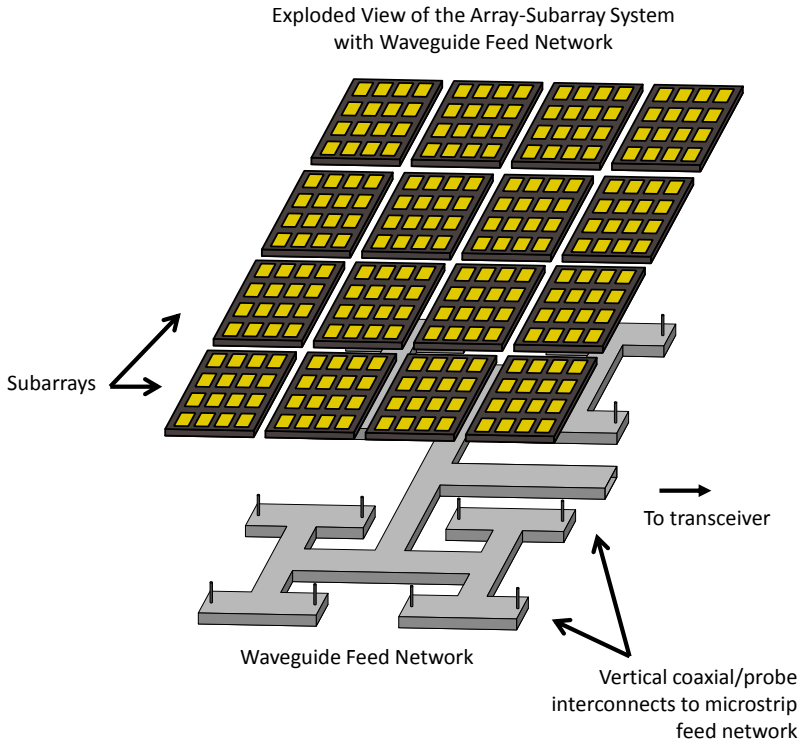

Figure 2.1: The array will be subdivided into modular subarray each fed by its own corporate waveguide feed network.

feed networks and other materials with different thicknesses.

2.3 Feed Network Consideration

In order to support the power handling capabilities needed to operate the array architecture, a corporate stripline feed network will be used in this design [31]. Because the stripline architecture has a homogeneous dielectric structure between two conductors [32], this feed network theoretically will not radiate beyond its structure, thus increasing radiation efficiency [33]. A stripline design contains comparable impedance bandwidth performance to typical microstrip feed network designs typically used for patch anten-

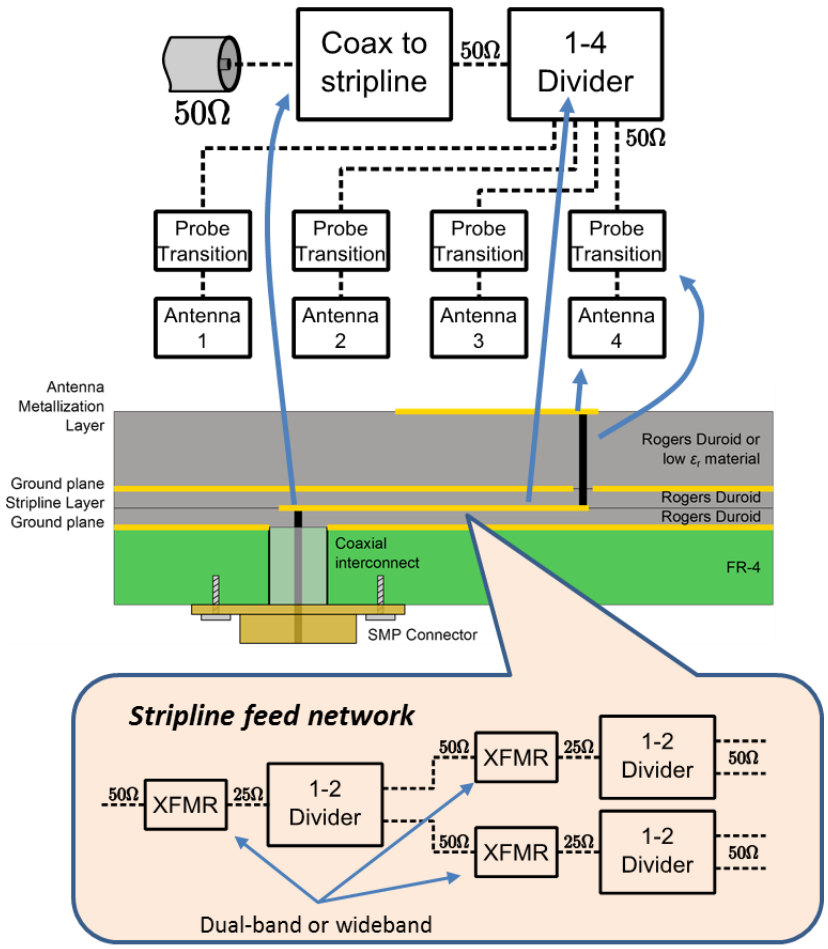

Figure 2.2: In order to support the subarray, the stripline feed network will consist of various 1:2 power dividers, dependent on the number of elements within the subarray. This will be placed below the antenna metallization layer and connected through the use of vias.

nas [34]. Still, in order to have an adequate design, the overall network must consist of a coaxial-stripline transition, an adequate equal power distribution scheme, a stripline to probe transition, and an equal phase distribution scheme. Moreover, good impedance matching (or S_{11}) at both the transmit and receive band, high efficiency, and good power handling can be achieved. Some of the more typical feed designs for patch antennas such as the E-shaped patch antenna is a coaxial line or a microstrip feed network [35].

Thus, a similar feed network known as the "Scales of Justice" design like in Figure 2.3 can be implemented. Although this introduces a multilayer design that may be

unattractive, the feed network may nonetheless achieve proper design requirements.

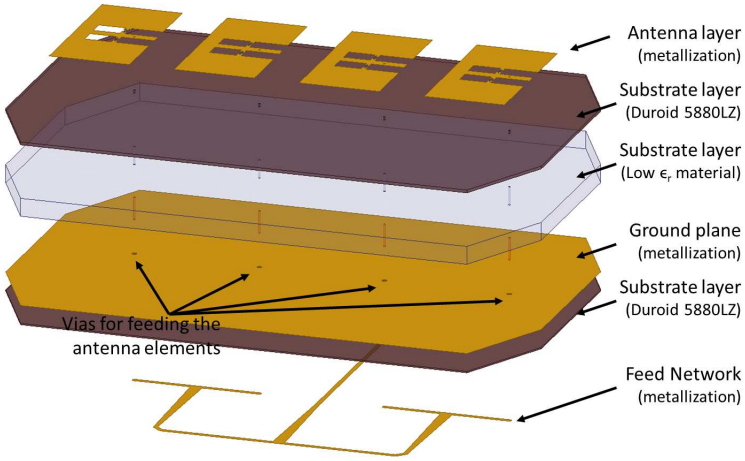

Figure 2.3: The multilayer deesign approach can be used as a testing architecture. Note that this is only an example of a 4x1 linear subarray. The final design will be a 4x4 subarray.

To maintain the simplicity, T-junction power dividers are used. In addition to this, dual band or wide band impedance transformers are implemented to provide 50Ω impedance. While there are some interesting dual band transformers [32], most of them require roughly λ_g length. A quarter wave transformer network, shown in Figure 2.4a, is adequately wide-band [36], so it can be tested to determine whether reasonable S_{11} can be obtained as in Figure 2.4b

Another area of interest in the feed network considerations is how to design the subarray architecture. One of the ways is through an integrated transmit/receive approach. In this design, patch elements that resonate in the higher frequency will be combined with patch elements that resonate in the lower frequency (Figure 2.5a). The main advantage of this design is that the layout is straightforward. However, this design would require two feed networks. Also, grating lobes may appear due to spacing. And the overall architecture is not easily scaled. Another alternative is to use a dual band CP element approach (Figure 2.5b). In this design, the elements themselves are dual-band. This would require only one feed network design. Because of this, the architecture would then be easily scaled for future missions if the choice of frequency varies. However, the difficulty lies

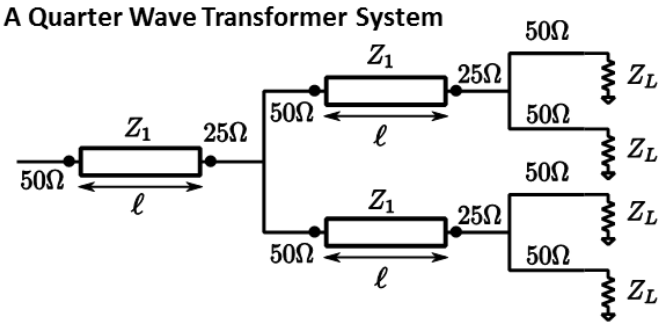

(a) Quarter Wave Transformer System

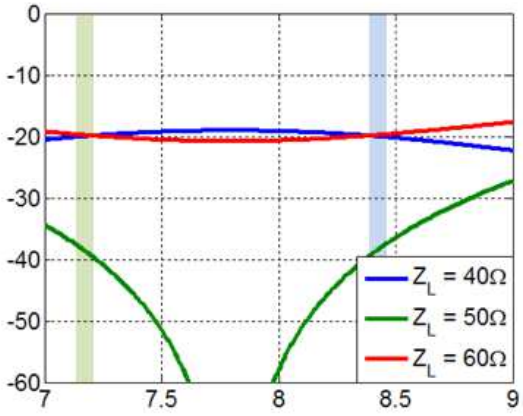

(b) S_{11} performance of quarter wave transformers between 7GHz to 9 GHz.

Figure 2.4: Quarter wave transformers are adequately wideband so a good S_{11} can be obtained. In fact, when a quarter wave transformer wave transformer was designed for X-band, good performance can be obtained for both the RX and TX bands for Z_L near 50Ω.

in the challenging element optimization. And if the patch element geometry is complex, the radiation patterns may be adversely affected. And finally, another architecture to consider is the dual-band dual-polarization feed network (Figure 2.5c). This would allow the use of simple element geometries. The tradeoff is now with the complex feed network design. The overall design would not be easily scalable, and the element design itself would become a challenge to attain both dual band and dual polarization characteristics. In this work, the primary direction for the subarray architecture was to pursue the dual-band element approach because the scalability of this design will save time and cost as this design becomes much more standardized. The disadvantages mentioned above can

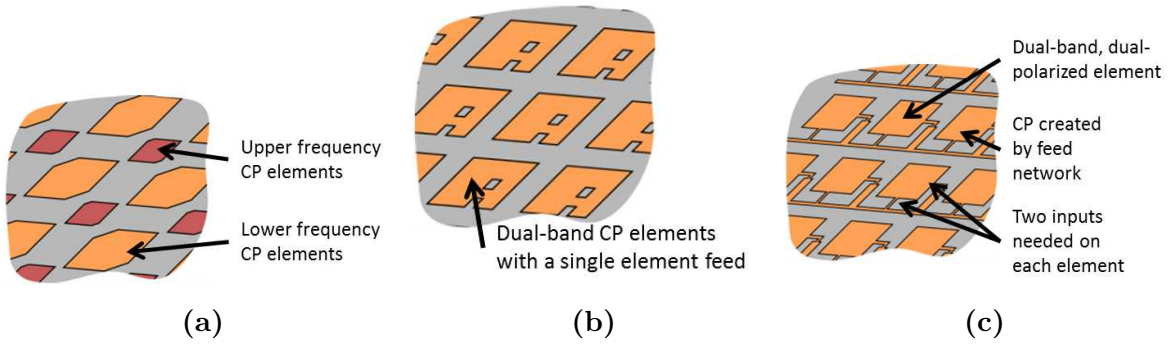

Figure 2.5: These are the various subarray architectures that can be used for this design such as the (a) Integrated TX/RX Approach (b) Dual band CP Element Approach and (c) Dual band Dual Polarization Feed Network Approach. Each offers various advantages and disadvantages.

be overcome in the element through rapid simulation and prototype testing. Moreover, similar solutions to problems can be used for other future missions which would improve scalability.

2.4 Substrate Consideration

In order to achieve better bandwidth performance, a low Q factor is necessary. This can be achieved through the use of thicker substrates. The Rogers Duroid 5880LZ, Figure 2.6, was used with a thickness of 4.32mm. This was the thickest sample that can be obtained from Rogers. Its electrical specification are as follows: its permittivity is $\epsilon = 1.96$ with a loss tangent of $tan\delta = 0.0019$ at 10GHz. Its electrical strength is measured at 285V/mil, equivalent to 1.12kV/mm.

2.5 Other Possible Feed Network Issues

In this work, a coaxial-to-stripline transition, Figure 2.7, was also implemented in HFSS. To make this fabrication simpler, the transition was built by using a vertical mount SMA connector, a small microstrip line, and a microstrip-stripline transition. The design/modeling process, Figure 2.8, is important in order to understand all the components

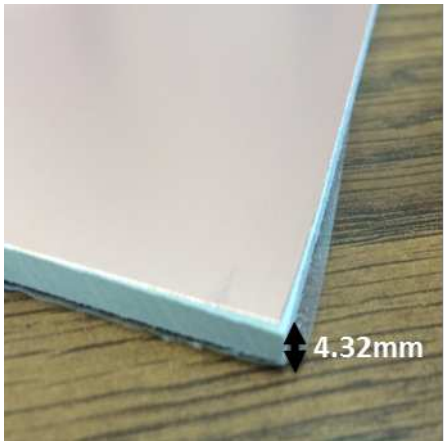

Figure 2.6: The Rogers Duroid 5880LZ will be used for this design.

and their effect on the performance

First, the SMA vertical launch design was incorporated into a full-wave solver Ansys HFSS [27]. This model is then validated by testing with a microstrip line, and then

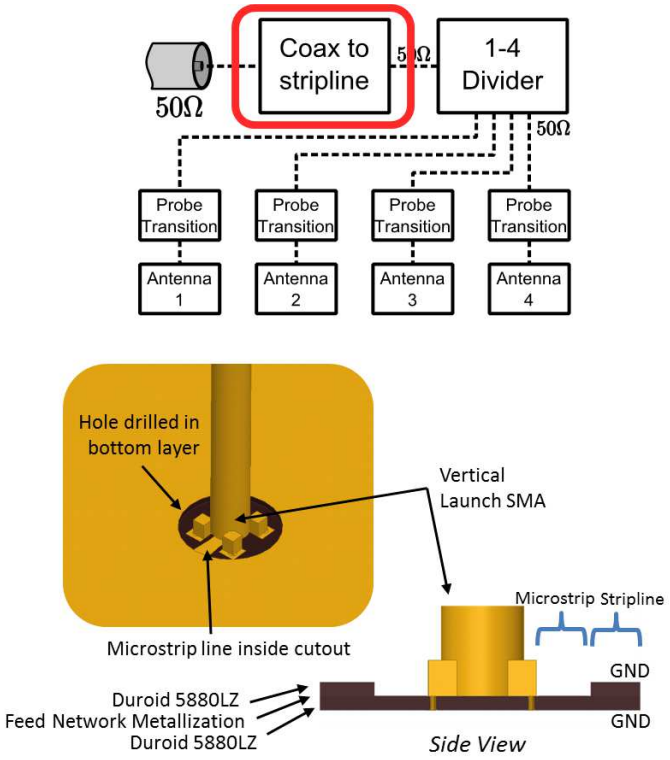

Figure 2.7: A coaxial to stripline connector was designed in HFSS by using a vertical mount SMA connector.

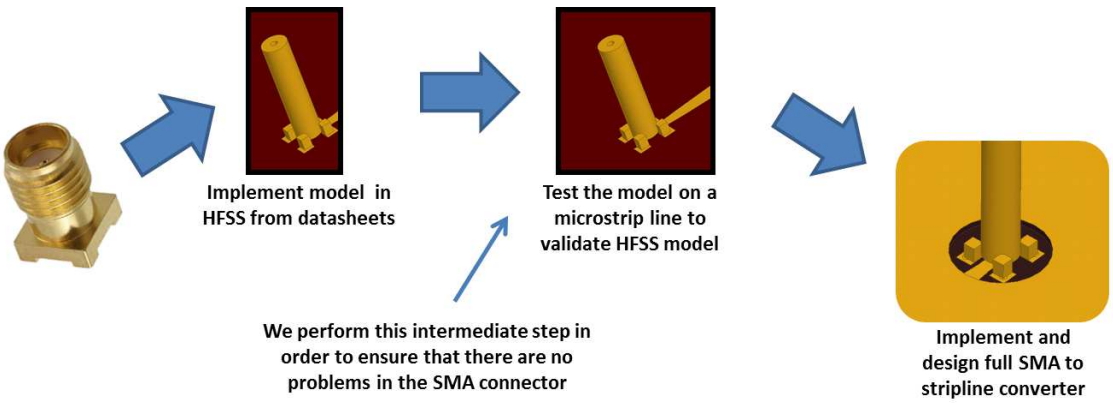

Figure 2.8: These are the steps used to design the transition in HFSS.

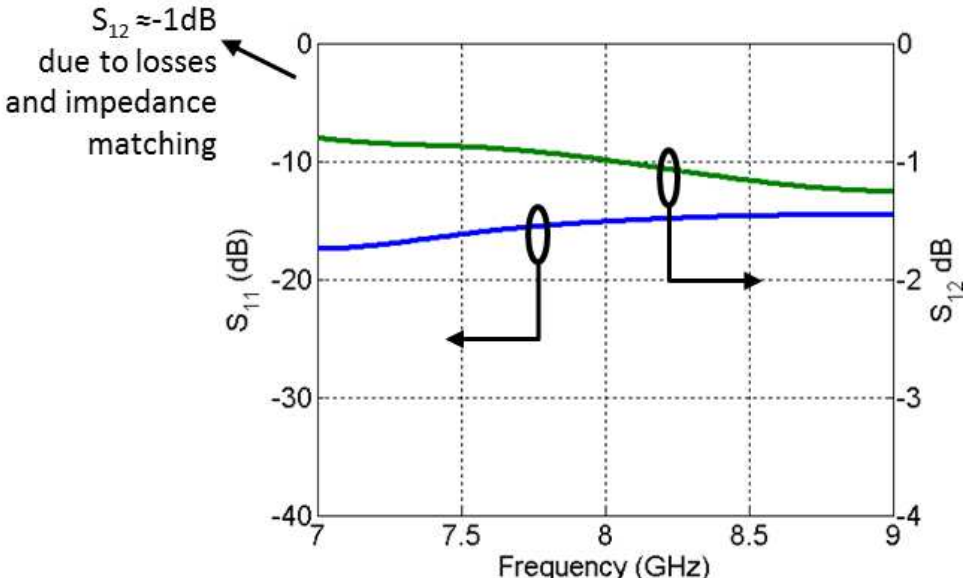

Figure 2.9: The S_{11} and S_{12} characteristics of this transition were adequate.

implement the final SMA to the stripline converter. The design was modeled using specifications by several manufacturers of vertical launch SMA connectors. The pads were also placed in the HFSS model with specifications given by the same manufacturers. Since a 50Ω line is a little large to fit in between the pads, a small linear taper was added to obtain 50Ω microstrip line. This assembly will have similar performance to the direct coaxial-to-stripline approach, but will not require difficult soldering.

Next, the full SMA-to-stripline transition with the SMA vertical launch model was

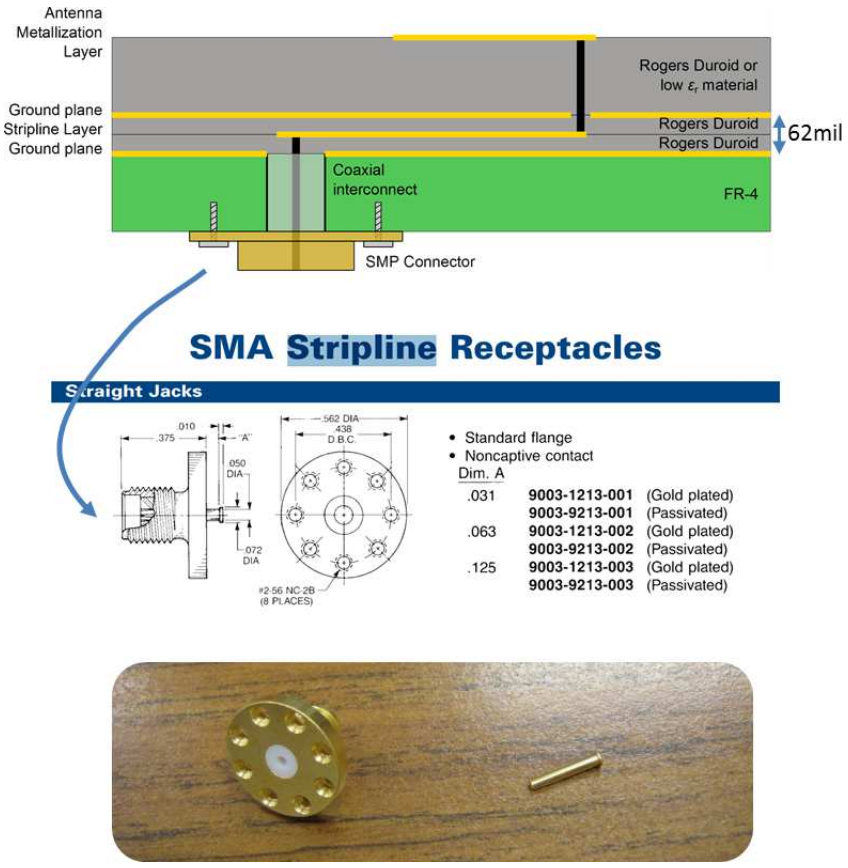

Figure 2.10: A Radiall 9003 connector was used for the SMA connector.

designed as well. The same model for the vertical launch SMA was used, assuming that hole would be drilled in the top layer. Currently the results show that the impedance matching and power distribution performance are $S_{11} = -15$ dB and $S_{12} = -1$ dB respectively in Figure 2.9. This can be improved with some slight changes in the geometry such as a tapered slot in the upper ground.

Now that the performance was shown adequately in the simulations, a specific SMA connector needs to be found. After much searching, a connector that can mount nicely to the stripline with minimal mechanical complexity was found. The connector is a Radiall 9003-1213-001 connector as seen in Figure 2.10. This connector is found adequate since two 31 mil boards will be used in the assembly. These are non-captive contacts which come in two pieces: the inner conductor and the flange.

CHAPTER 3

Survey of Various Element Designs

3.1 Review of Possible Element Candidates

Designing a compact novel antenna array architecture can be a difficult challenge. The requirements of higher performance, higher gain, and higher power handling, can be a daunting task. In addition to this challenge is the need to incorporate CP into the antenna design because of the difficulty of exciting two equal magnitude and orthogonal modes within a wide frequency band. This antenna array will be used to augment Direct-to-Earth (DTE) radio communications for newer Mars Rover designs such as the one to be used in the Mars2020 mission. This design can enable higher data rates in order to return larger amounts of scientific data to Earth without UHF relay mechanisms. In order to support these high performance requirements, a hybrid assembly of CP microstrip patch antenna element in a subarray topology operating in X-band frequency will be used. These will then be fed with a waveguide network to reduce loss and increase power handling capabilities.

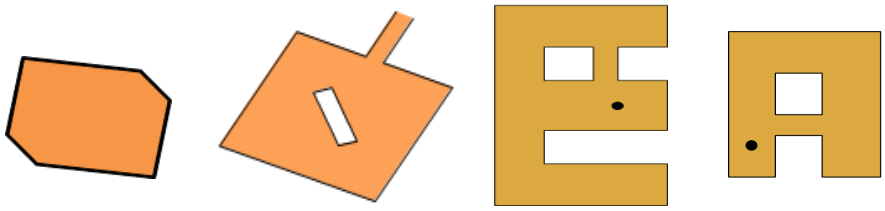

Figure 3.1: Microstrip patch antennas are popular choices for compact and high gain array antenna architectures. Their geometries can be modified in order to create desired performances such as circular polarization or high bandwidth.

Microstrip patch antennas, Fig 3.16, offer various advantages. First, they are compact and can easily be incorporated with integrated circuit networks. This enables the ability to incorporate them into robotic structures such as Mars rovers. Moreover, patch antenna elements can be designed to be single layer and single fed, reducing the complexity in their fabrications due to multiple layer construction, but still able to provide adequate bandwidth [37]. More importantly, when incorporated in an array environment, patch antennas can allow for greater gain comparable to those of reflector antennas [38]. The main disadvantage with microstrip patch antennas is that they are narrowband [4], on the order of about 5% [9]. When incorporating CP, typical patch antenna designs yield a S_{11}/AR bandwidth of only 1% as well [25]. Various geometry modifications have been adopted to increase the S_{11} bandwidth such as the U-slot element [8–10], L-probe [18,19], and E-shape element [14,17,21]. Other mechanisms such as corner truncations will also be considered as these have in the past provided acceptable performance [39]. These designs are often advantageous because they do not require a complex feeding network or a stacked/multilayer configuration. These various designs will be discussed in this chapter and will be investigated to see if adequate S_{11}/AR performance can be attained in the X-band region where Mars rovers typically operate for DTE communications. For the first part of this chapter, each of the patch geometry candidates will be discussed in detail how radiation is achieved in the frequency they were initially designed for. The reason for this is to understand the physics and the performance of each of the candidates. This will allow adequate background information so as to tune the candidates in the required X-band frequencies. Then, mechanisms to add CP into the geometry will be explored. This means that only the S_{11}, AR, directivity, and radiation pattern performance for the element candidate's CP design will be shown. At the end of that discussion, elements that achieve dual-band CP characteristics will be tested in the required X-band frequencies. The chosen candidate will be optimized through the use of Particle Swarm Optimization (PSO) [28], to obtain adequate X-band RF performance.

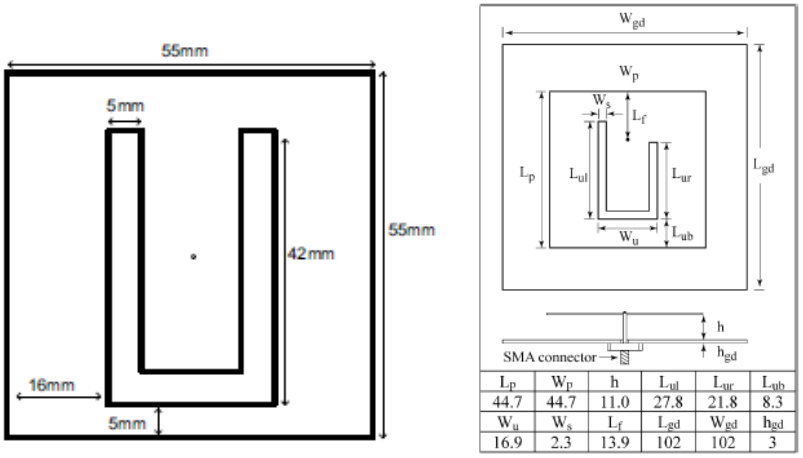

L_p	W_p	h	L_{ul}	L_{ur}	L_{ub}
44.7	44.7	11.0	27.8	21.8	8.3
W_u	W_s	L_f	L_{gd}	W_{gd}	h_{gd}
16.9	2.3	13.9	102	102	3

(a) **(b)**

Figure 3.2: U-slot antennas are a popular choice for achieve high bandwidth and high gain characteristics. Both LP (a) [9] and CP (b) [8] characteristics are possible.

3.2 U-Slot Patch Antenna

One popular patch antenna geometry is the U-slot antenna [10]. One of its advantages is its ability to operate with adequate performance with a single layer single patch assembly. The U-slot antenna is a rectangular patch antenna where the shape of the letter U is cut around the center of the rectangular patch. One of the examples its performance is in [10]. The rectangular patch had dimensions of 8.65" x 4.90" with a 0.4" - 0.35" wide U-shaped slot with dimensions of 2.70" x 3.235" cut at the center of the rectangular patch. In this experiment, the bandwidth achieved was 47% at 900 MHz using a criteria of VSWR ≤ 2. The measured radiation patterns showed better performance than a much simpler rectangular geometry. The half power beamwidth in the XZ plane was 59^o and in the YZ plane 65^o at 812 MHz. Similar results were achieved at 1.1 GHz. The novelty of this antenna is that wide bandwidths are achieved without the need to incorporate parasitic patches through a multilayer architecture or within the element layer. Instead, the performance is improved because of the current introduced at the edge of the slot which creates a new resonance that combines with the main resonance of the main rectangular patch. Moreover, the capacitive reactance of the slot also compensates for the inductive

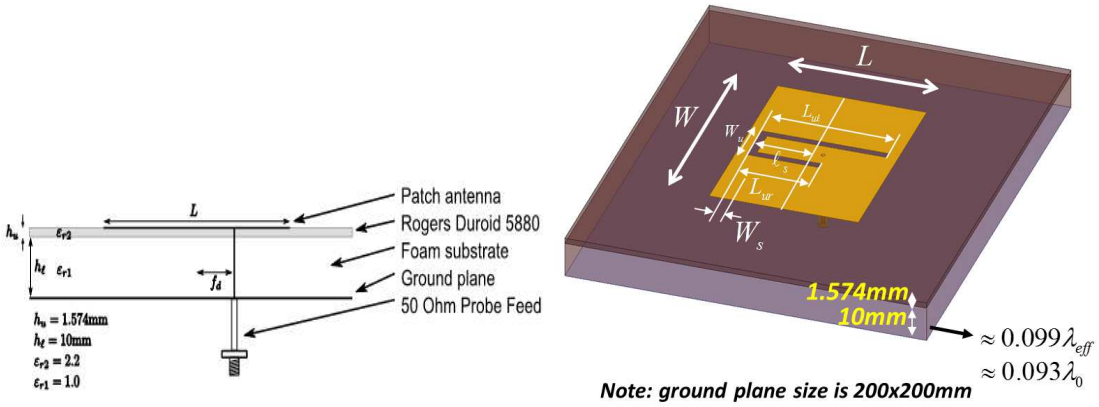

(a) Side View **(b)** 3D View

Figure 3.3: In order to improve the performance found in [8], PSO techniques found in [28] were implemented to see if the S_{11} and AR bandwidth performance can be improved.

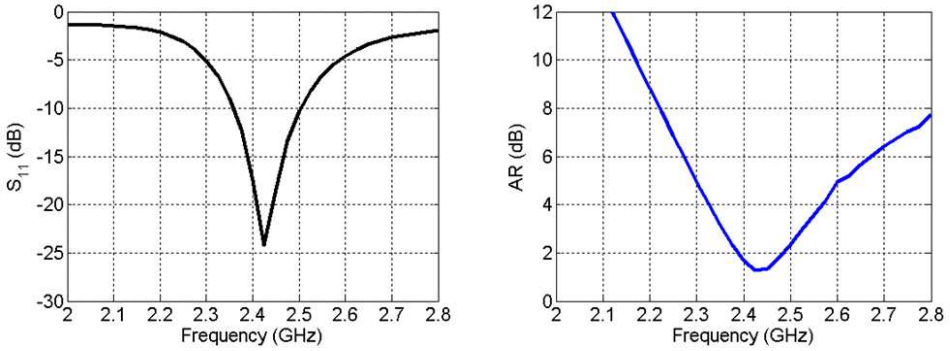

(a) $|S_{11}|$ Bandwidth **(b)** AR Bandwidth

Figure 3.4: After the PSO technique was used on this U-slot geometry, the final bandwidth was 145MHz, 6% at 2.4GHz.

reactance of the probe thus increasing bandwidth because thick substrates are obtained.

In another recent study, [9] shows that at 2.4 GHz, the U-slot antenna, Fig 3.2a, was able to achieve a bandwidth of 24%, using a criteria that $S_{11} \leq$ -10 dB. The square patch was 55 mm by 55 mm with a 5 mm wide 42 mm long U-shaped slot. The U-shape was cut 5 mm above the bottom edge and 16 mm to the right of the left edge of the square patch. Again, the performance is improved through the dual-resonant behavior. Because the slots are effectively parallel to the non radiated edges of the patch, currents are able to follow two different paths on the surface. This offers a dual-mode, wide-band operation.

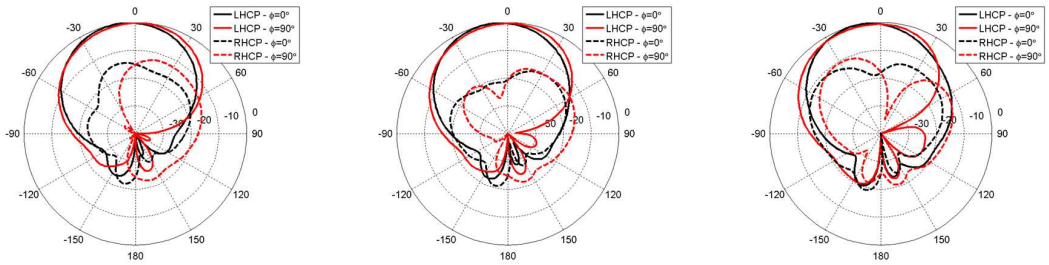

(a) $f = 2.35$ GHz **(b)** $f = 2.4$ GHz **(c)** $f = 2.5$ GHz

Figure 3.5: After using PSO, decent radiation patterns for the U-slot antenna are observed throughout this frequency band.

The above two examples show linear polarized antennas (LP) in which both antennas were able to achieve substantial bandwidth. This is in comparison to a square patch that [9] shows, only attains a 5% bandwidth at 2.4 GHz. Because of this decent RF performance, further investigations were made to attempt at creating a CP U-slot element. In [8], one of the arms of the U-slot was curtailed to achieve circular polarization so as to excite two orthogonal modes. This removes the need to curtail the edges of the rectangular patch or other complex mechanisms to achieve CP characteristics. In fact, the authors in [8] suggested that by adjusting the length of the U-slot to an optimum position along the y-dimension, one can obtain desired AR characteristics. The results are promising, a 9% impedance bandwidth ($|S_{11}| \leq$ -10dB) and a 4% axial ratio bandwidth (AR $\leq$ 3dB). Therefore, the overall S_{11}/AR bandwidth is 4%. This antenna also attains an average gain of 8dBi across the frequency of operation with beamwidths of 58^o in both XZ and YZ planes.

Table 3.1: Dimension of the U-Slot CP Patch Antenna (in mm) After [28] was Used

	W	L	Ls	Ws	Ps	f_s	l
OptimizedDesign	78.8	43.7	35.1	9.84	7.46	8.97	14.1

Since the above cited literature showed that the U-slot geometry for patch antennas showed promise, an optimization through the use of PSO methods found in [28, 30] were developed for this architecture. Table 3.1 below shows the dimensions of the U-slot patch

Table 3.2: Directivity (in dB) of the Optimized CP U-Slot Patch Antenna

2.35 GHz	2.4 GHz	2.5 GHz
9.2 dB	9.0 dB	8.0 dB

antenna after PSO was used.

Using a full-wave solver [27], the S_{11}/AR bandwidth was measured to be 145 MHz, 6% at 2.4 GHz. This bandwidth, as can be seen by Fig 3.4a, is limited by the narrow impedance bandwidth. Even though other researchers had higher bandwidth such as [8], the AR bandwidth after optimization is higher.

Now to further prepare this element candidate for comparison later, the CP U-Slot's radiation patterns were also obtained through [27] shown in Fig. 3.5. The directivity, shown in Table 3.2, that at 2.4 GHz, the directivity was 9.0 dB. In looking at the $\phi = 0^o$ plane, there is a slight beam tilt towards the $\theta = -11^o$. Overall, the radiation patterns observed using the full-wave solver were adequate. And a higher AR bandwidth was achieved. The U-Slot patch antenna will still be used as a candidate to be used for the overall patch subarray.

3.3 Thick Substrate Patch Antennas (TCPA) with Ring Capacitors

Microstrip patch antennas are advantageous in that they are low profile and fairly easy to fabricate. However, they inherently suffer from narrow bandwidth, typically less than 5% [18]. One of the ways used to broaden bandwidth is through the use of thick substrates. However, for thick substrates, additional probe inductance must be considered. As the height of the probe increases, the probe inductance increases to an amount that would never allow good impedance matching. One of the ways to eliminate this is through a series capacitor which would allow thicker substrates for broadening bandwidth. In [40],

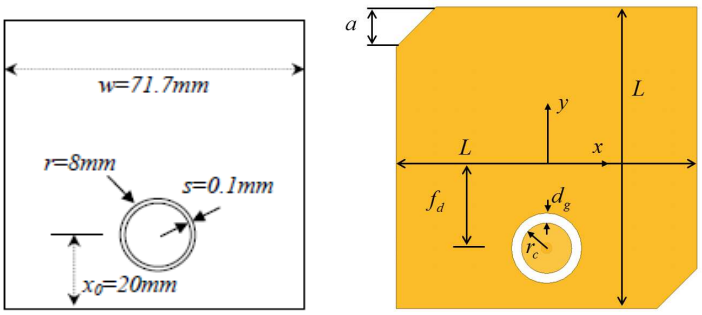

Figure 3.6: Thick substrates are used to extend the bandwidth of traditional rectangular patch antennas. LP (a) and CP (b) designs are possible.

a series capacitor through the use of a circular disk and a circular gap is used. The author shows that good bandwidth characteristics are achievable as the additional inductance is cancelled by the series capacitor. In fact, in [41], the optimum return loss for a given thickness and feed position were studied based on a certain thickness of substrate. In retrospect, these bandwidth extending techniques using a rectangular patch antennas, though useful and easily understood based on the patch antenna's circuit model, are often not as wide-band as the other patch geometries such as the LP E-shaped or U-slot patch antennas. In the case of using ring capacitors for LP patch antennas, the difficulty on achieving the small gaps in fabrication far outweigh its intended benefits.

The strength of the thick substrate patch antenna technique using the ring capacitors is more evident when trying to achieve CP using microstrip patch antennas. [25] shows how ring capacitors can extend the S_{11}/AR bandwidth. In their design, the typical truncated corners patch design, used to excite CP, is used. The annular gap is placed to act as a capacitor. The height and the resonant frequency were kept constant and the parameters L, r_c, d_g, and f_d shown in Fig 3.6b, were tuned to get good S_{11}/AR bandwidth. In this work, increasing the parameter r_c increases capacitance while increasing the gap parameter, d_g decreases the capacitance. Using the manually tuned parameters shown in Table 3.3, a broadband S_{11}/AR bandwidth of 5.8% at 2.4 GHz shown in Fig. 3.7 was achieved.

Table 3.3: Dimensions of the CP TCPA with Ring Capacitor

L	a	r_c	d_g	f_d
47	15	3	0.25	19

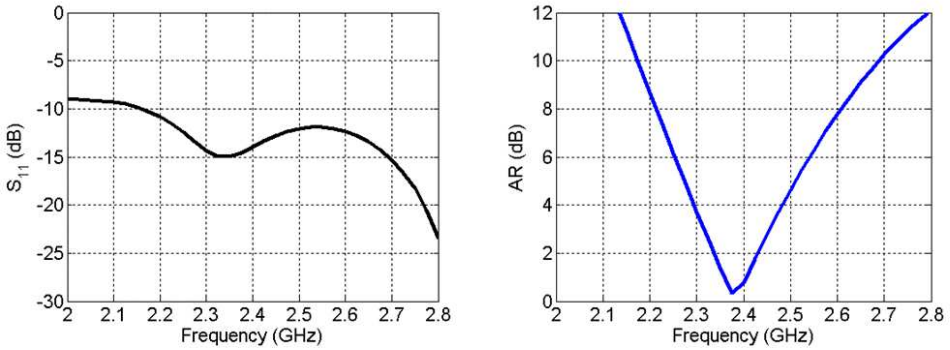

(a) $|S_{11}|$ Performance **(b)** AR Performance

Figure 3.7: Through the use of the ring capacitor, a truncated corner patch antenna (TCPA) can achieve a S_{11}/AR bandwidth of 5.8% at 2.4 GHz.

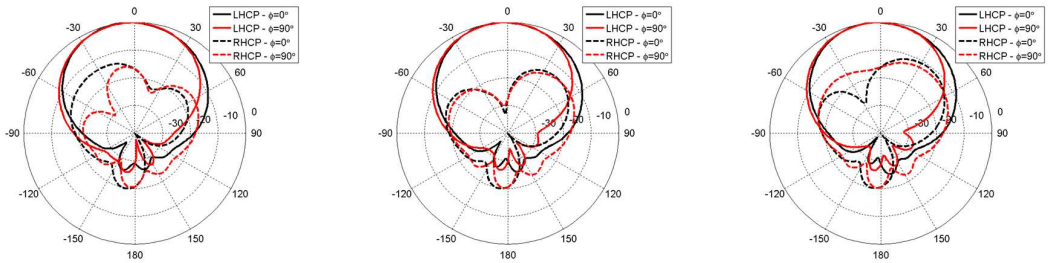

(a) f = 2.35GHz **(b)** f = 2.4 GHz **(c)** f = 2.5 GHz

Figure 3.8: The radiation patterns for the TCPA with ring capacitors are fairly reasonable even with the slight pattern tilt.

The design is fairly comparable to the CP U-slot antenna. This was achieved without the need of exotic slots or probe feeds. In fact, the design was straightforward. The simulated radiation patterns were obtained and were fairly reasonable with low cross-polarization levels shown in Fig. 3.8. The patterns do exhibit a small pattern tilt, but the effect is minimal and can be improved for higher frequencies.

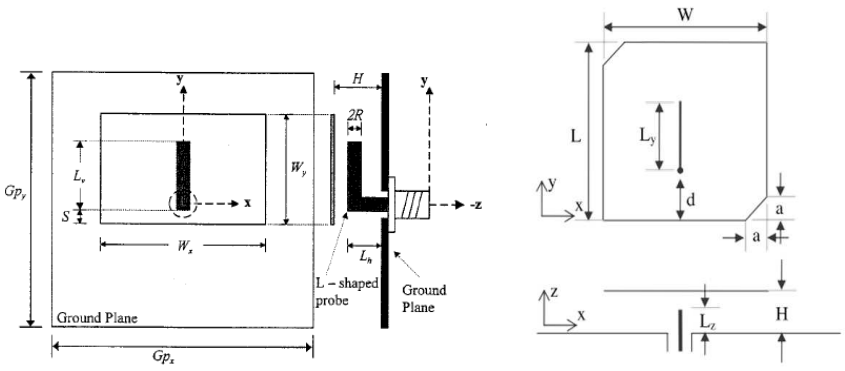

(a) **(b)**

Figure 3.9: L-Shaped Probe Patch Antennas allow the use of thick substrates by suppressing additional inductances by the probe itself. Thus, creating a wideband design. LP (a) and CP (b) designs are possible.

3.4 L-Shaped Probe Patch Antenna

As mentioned in the beginning of this chapter, thicker substrates are often used to overcome the inherent narrowband performance of patch antennas. However, the increase of the feed reactance with height limits the possible bandwidth to less than 10%. To overcome this extra parasitic effect, L-shaped probes can be used. These L-shaped probes add capacitance that cancel the inductance added by the longer probe feed. In [20], a rectangular patch with a width of 30 mm and length 25 mm was fed with a 50Ω SMA connected with a L-shaped probe. The patch was supported with a foam layer, containing a dielectric constant near 1, with a thickness of 6.6 mm. The author points out that these dimensions are chosen close to the optimum broadband operation. Using this idea, the achieved bandwidth was 28% between 3.76-5.44 GHz with a gain of 7.5 dBi, slightly lower than a U-slot patch antenna with a 32% bandwidth when both have the same thickness of 5 mm. Another design in [19] cites a a 36% bandwidth with an average gain of 7 dBi.

The effectiveness of the L-Shaped probe comes from two parts, its vertical and horitzontal portions. The vertical portion is an open circuit stub that is less than a quarter of wavelength long, creating a capacitive component. The horizontal portion is inductive. The combination of the two creates a resonant element with a frequency close to that of

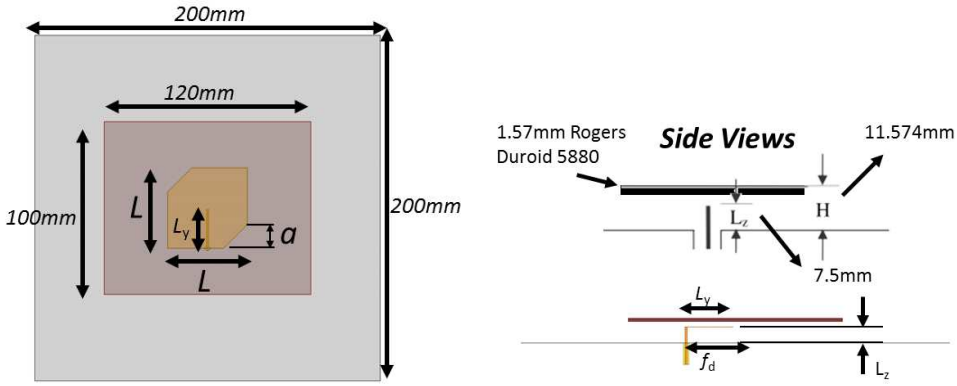

(a) Top View **(b)** Side View

Figure 3.10: CP L-Shaped Probe design at 2.4 GHz

Table 3.4: Dimensions of the CP L-Shaped Probe

L	L_y	a	f_d
46.5	22.0	14.0	-23.0

the TM_{01} mode excited in the patch. Thus, broad bandwidth can be achived through the use of L-shaped probe [20].

Like its previous counterparts, the L-shaped probe can achieve circular polarization. This was done through a truncated corner square shaped geometry to excite two orthogonal modes [39]. Whereas before, the patch geometry is a rectangular shape for linear polarization. An air substrate was used through the use of foam to support the patch in the measurements. Manual tuning of the parameters used in [23], was performed in order to get good AR performance, and S_{11} performance at 2.4 GHz. The geometry shown in Fig. 3.10 with the final design parameters are listed below in Table 3.4. This design was able to yield 5.5% bandwidth at 2.4 GHz. As can be seen from Fig. 3.19, this L-shaped probe patch antenna is able to achieve a wideband S_{11} performance yet is mainly restricted by the AR performance. In looking at this patch antenna's radiation patterns in Fig. 3.12, no beam tilt occurs within its frequency band. Overall, the L-shaped probe patch antenna is a good candidate for consideration because of its good CP performance.

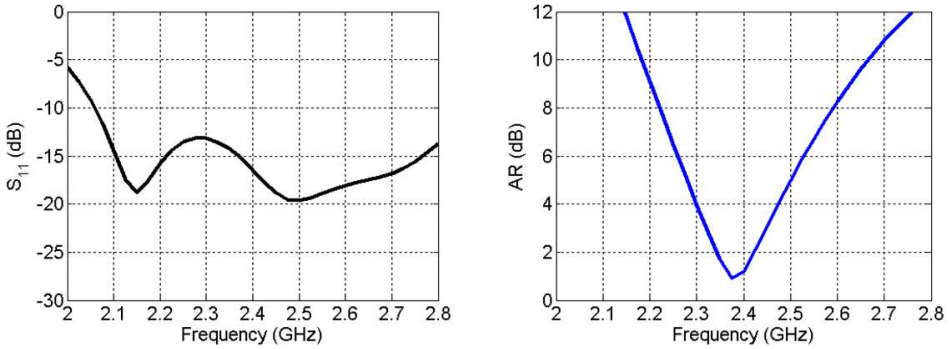

(a) $|S_{11}|$ Performance **(b)** AR Performance

Figure 3.11: Through the use of the L-shaped Probe, a S_{11}/AR bandwidth of 5.5% can be achieved around 2.4 GHz.

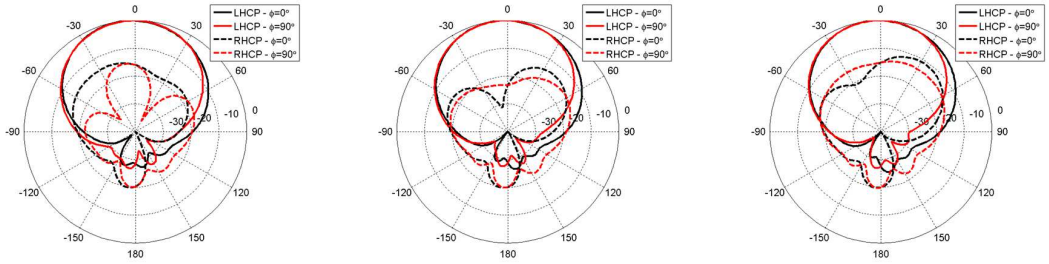

(a) f = 2.35GHz **(b)** f = 2.4 GHz **(c)** f = 2.5 GHz

Figure 3.12: The radiation patterns for the L-shaped probe show that no beam tilt occurs within its frequency band.

3.5 E-Shaped Patch Antenna

Another novel geometry for a microstrip patch antenna that has dominated literature in recent times is the E-shaped patch antenna shown in Fig. 3.13. The geometry typically involves two parallel slots incorporated into a patch antenna. According to [13], the impedance bandwidth can reach upwards of 30%, comparable to the U-slot antenna. The advantage is that the E-shaped patch antenna is much simpler to fabricate and its characteristics can be adjusted by only three simple parameters: the length, the width, and the position of the slots. The design in [13], used to operate between 1.9-2.4 GHz, was 70 mm long, 50 mm wide, and 15 mm thick. The length of the slot was 40 mm and a width of 6 mm. This design was able to achieve 30.3% impedance bandwidth. This

same antenna was able to achieve a directivity of 8.5 dB at 2.4 GHz. One of the unique characteristics of the E-shaped patch antenna is its ability to support both a wide-band and a dual-band performance. [13] observes that as the slot position, P_s, is increased, two distinct resonances can occur. In their research, resonances occurred at 1.9 GHz and 2.4 GHz, showing S_{11} levels lower than -10 dB. This parameter can be useful in designing either a wide-band or dual band performance.

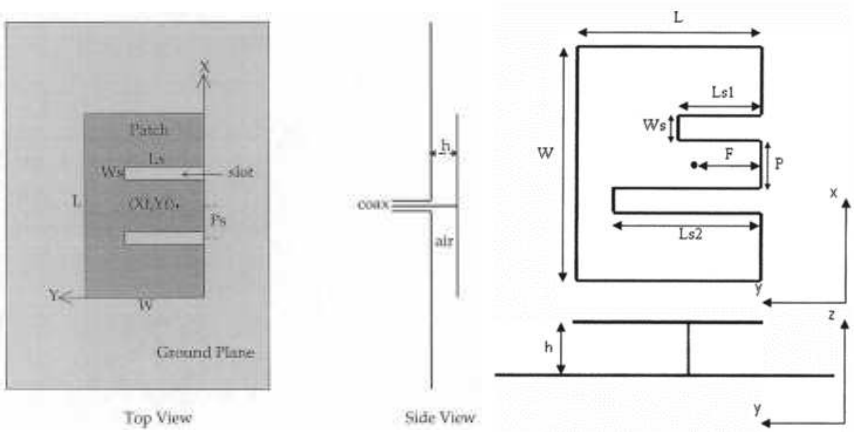

Figure 3.13: E-Shaped Patch Antennas also offer a wide-band or dual-band LP (a) or CP (b) operation while maintaining a single-feed and single-layer architecture.

The idea behind the wide-band mechanism of the E-shaped patch antenna is because of the current flow on the top of the patch. Because of the introduction of the slots on the geometry, dual resonance is observed. As the patch is fed from its center, the currents flow like a typical rectangular patch. This phenomenon can be modeled using an equivalent parallel inductance and capacitance circuit, creating the initial resonance. However, when the two slots are introduced into the system, a new resonance occurs because of the behavior of the current flow at the edge part of the slots. These currents have to flow around the slot, which therefore increase the length of the current path. This increase can be modeled as an additional series inductance that creates a lower resonance than if the patch never had the slots. Therefore, dual resonance occurs because these two resonant circuits couple and form the wide bandwidth performance of the E-shape patch

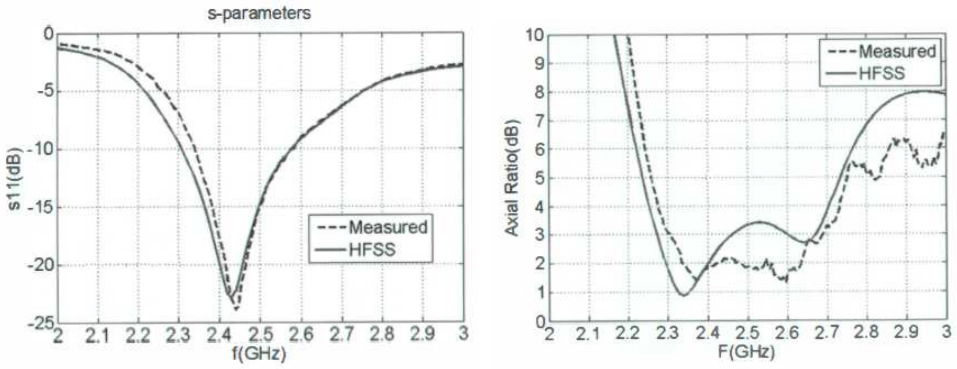

(a) $|S_{11}|$ Performance **(b)** AR Performance

Figure 3.14: The CP E-Shaped Patch Antenna was able to achieve a 9.26% S_{11}/AR bandwidth using a dielectric with $\epsilon = 2.2$.

antenna [13].

To obtain circular polarization from the E-shaped patch geometry, asymmetrical slots are used as shown in [12]. These slots can be adjusted using their length, width, and position, so as to excite orthogonal and equal magnitudes current components. To objective is to find a length of the slots that create an electrical path length so as to create a phase difference between current components of 90^o. The probe position, typically used for improving impedance matching performance, also improves axial-ratio levels to create circular polarization within the band of interest. Using an air substrate, [12] was able to attain a 6.5% axial ratio bandwidth within 2.38-2.54 GHz. This is quite a wideband design for a single-layer single-feed microstrip patch antenna. This was compared to the unequal-arms U slot which achieved 4% bandwidth and the truncated-corner U-slot antenna which achived a 4.5% bandwidth.

[12] also showed that circular polarized design is achievable using a material substrate. The S_{11}/AR bandwidth for this design was 9.27% between 2.34-2.57 GHz as shown in Fig. 3.14. This antenna is also a good broadside radiator at 2.45 GHz with a maximum gain of 8.3 dBi, shown in Fig. 3.15, with low cross-polarization levels. Again, such a design is quite wideband for a single-feed single-layer patch antenna.

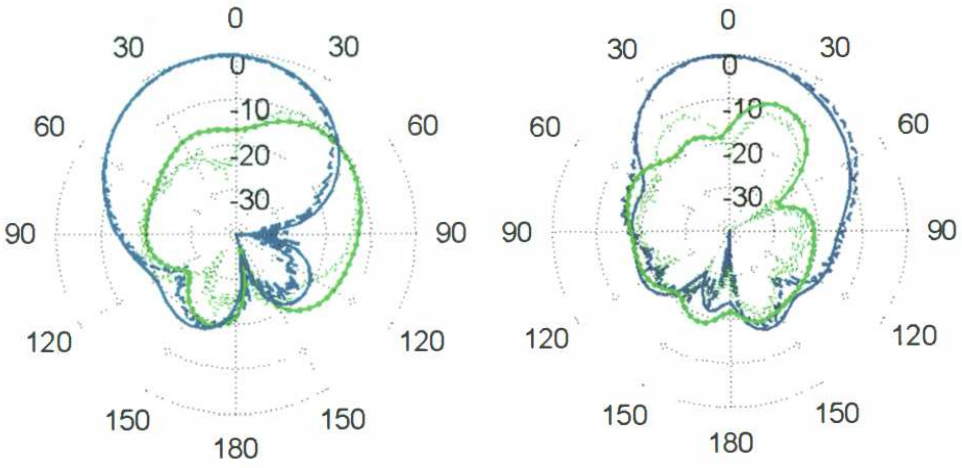

(a) YZ Plane **(b)** XZ Plane

Figure 3.15: The radiation pattern of the CP E-Shaped Patch Antenna at 2.45 GHz. The blue curve is the RHCP pattern and the green curve is the LHCP pattern.

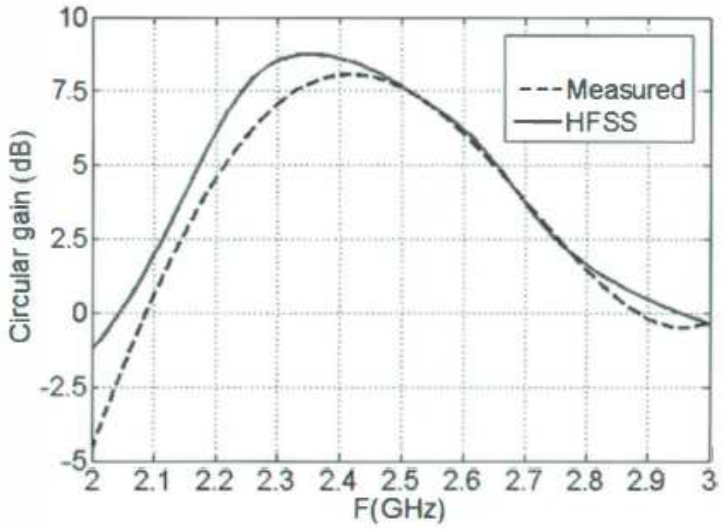

Figure 3.16: The gain of the CP E-Shaped Patch Antenna is also very wideband, achieving a 3dB 15.5% bandwidth between 2.27-2.65 GHz. The maximum gain 8.3 dBi.

3.6 Half E-Shaped Patch Antenna

As was seen from section 3.5, the E-shaped patch antenna is a novel patch geometry that can achieve both wide-band and dual-band LP or CP characteristics. The half E-shaped patch antenna, shown in Fig. 3.17, mimics some of its full E-shaped counterpart's behavior in that it still utilizes the slots to create CP. However, the halved structure is

advantageous because it is not as electrically large and can make for a compact design. In [21], a half E-shaped design for 2.6 GHz is investigated. It has length 45 mm and a width of 35 mm. It is compared with a full E-shaped with a width that is twice as long and with a length equal as the half E-shaped patch. Both are supported by a foam substrate with a height of 10mm. The results show that 25.2% S_{11} bandwidth, 2.25-2.9 GHz, was achieved for the half E-shaped compared to 24.5% for the full E-shaped patch. Similar results have been found in [42] which show that measured impedance bandwidth was able to reach 24.2%. The gain achieved for the half E-Shaped antenna was 8 dBi compared to 9 dBi for the full E-shaped patch. The half E-shaped antenna maintains the wide-band characteristics of the full E-shaped patch yet the size is reduced by 49%.

In another study, [22] shows that a cavity structure added to the half E-shaped patch antenna can increase the impedance bandwidth and gain while reducing backward radiation of the antenna. The half E-shaped patch geometry was 53.2 mm by 53.2 mm with a height of 10 mm. A cavity structure was placed around the half E-shaped patch and connected to the edges of the square ground plane with dimension. Because the cavity structure has its own resonance, this adds to the two resonance that occur for the half E-shaped patch. In this case, the resonance is controlled by the height of the cavity and the size of the ground plane. If these can be properly adjusted, coupling the resonances together can result in a wider bandwidth. Using a cavity with a height of 0.5λ (λ at 2.05 GHz) and a square ground plane sized at 0.9λ, 22.37% bandwidth was achieved [22]. This bandwidth is similar to that of [21]. When the ground plane size was extended to 1.6λ was chosen, the half E-shaped patch achieved 10 dBi to 12.6 dBi gain.

From the previous research cited above, the half E-shaped patch antenna's wide-band characteristics with its small profile is advantageous. If the half E-shaped patch antenna's wide-band characteristics can be maintained while simultaneously meeting CP specifications, this patch geometry can also be an excellent candidate for DTE communications. In recent literature, mechanisms to add CP functionality to the half E-shaped patch antenna have remained unknown. However, this research has shown that by adding a bar

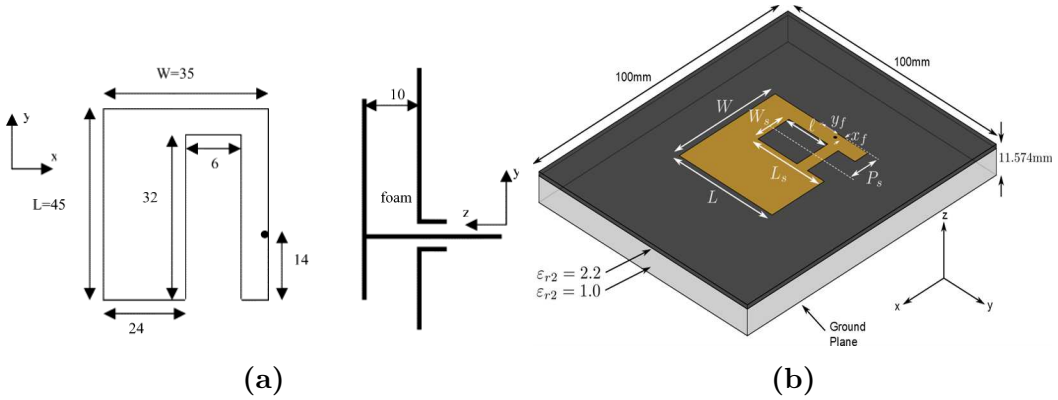

Figure 3.17: Half E-shaped patch antennas are similar to their E-shaped counterparts but have almost a 50% reduction in their size. LP (a) and CP (b) designs are possible.

between the slot, as shown in Fig. 3.17b, wide S_{11}-AR bandwidth can be achieved. Good performance can be achieved through the use of PSO, a similar process utilized for the U-slot antenna in the previous section, 3.2. To create a baseline for comparison, a CP full E-shaped antenna has also been optimized through PSO. The results of the optimized parameters are shown in Table 3.5. A comparative drawing of the two patch geometries is also shown in Fig. 3.18. The simulatons showed that the CP half E-shaped patch antenna can obtain a very wide-band S_{11} response shown in Fig. 3.19a, similar to the performance offered by the CP full E-shaped design. However, the limitation occurs when comparing the AR performance. The CP half E-shaped design achieves 5% AR bandwidth at 2.4 GHz. With the original E-shaped patch, much broader AR bandwidth was possible as can be seen in Fig. 3.19b. When looking at the radiation patterns in Fig. 3.20, slight beam tilt occurs within its bandwidth. The directivity achieved is about 8.79 dB at 2.4 GHz where cross-pol levels is -10.27 dB at 2.4 GHz. The cross-pol level is taken as the boresight directivity versus the maximum LHCP component. With these results, the CP half E-shaped patch antenna still offers great S_{11}/AR and radiation performance while offering a compact design without requiring small gaps.

Table 3.5: Dimension of the full E-shaped and half E-shaped Patch Antennas (in mm) After [28] was Used

	W	L	Ls	Ws	Ps	y_f	x_f	l
E-shape	89.0	45.0	36.0	9.25	7.47	10.5	0	15.1
Half-E	55.1	49	43.3	11.8	10.66	10.7	2.17	11.5

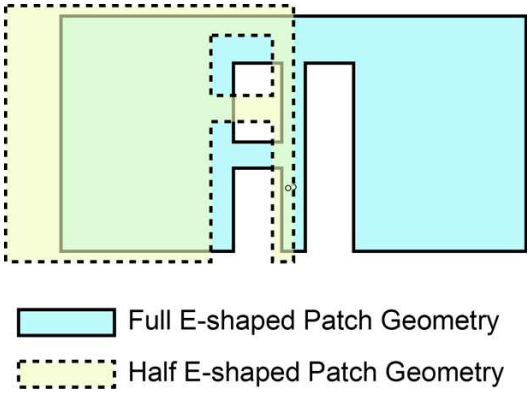

Figure 3.18: Comparison of the two E-shaped geometries. This shows that the half E-shaped patch occupies only 50% of the area required for its full E-shaped counterpart.

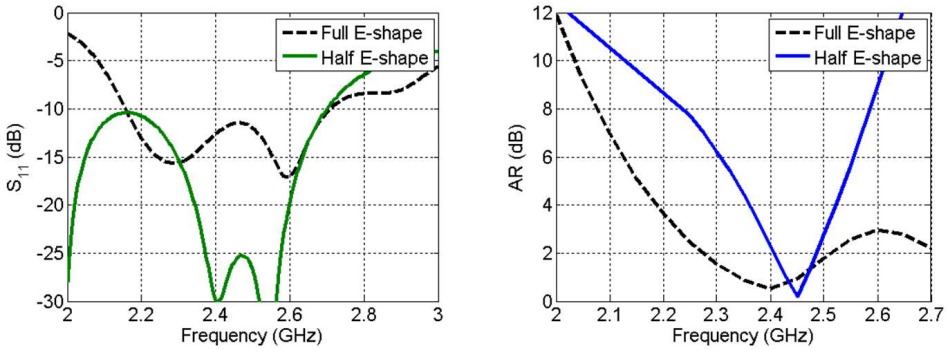

(a) $|S_{11}|$ Performance **(b)** AR Performance

Figure 3.19: The CP half E-shaped patch is able to achieve 5% S_{11}/AR bandwidth, similar to other designs.

3.7 Element Comparison in S-band

The previous patch elements offer various advantages for utilization in Mars rover DTE communications. In this section, a quick comparison of the five elements will be discussed. Only a few of the element candidates will be tested into the X-band in order to optimize

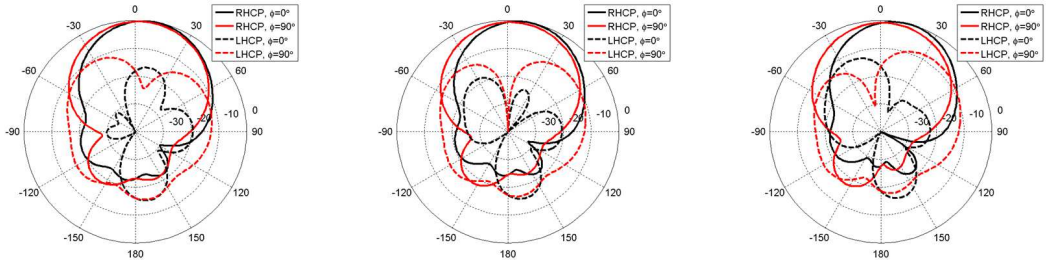

(a) $f = 2.4$ GHz **(b)** $f = 2.45$ GHz **(c)** $f = 2.5$ GHz

Figure 3.20: The radiation patterns for the CP half E-shaped patch show slight beam tilt within its frequency band.

Table 3.6: Comparison of the Patch Elements in the S-band

	S_{11}/AR Bandwidth	Height	Size
CP U-slot Patch	6%	$0.1\lambda_{eff}$	$0.63\lambda_0$ x $0.34\lambda_0$
Ring Capacitor Thick CP Patch	5.8%	$0.1\lambda_{eff}$	$0.38\lambda_0$ x $0.38\lambda_0$
CP L-shaped Probe Patch	5.5%	$0.1\lambda_{eff}$	$0.37\lambda_0$ x $0.37\lambda_0$
CP half E-shaped Patch	5%	$0.1\lambda_{eff}$	$0.44\lambda_0$ x $0.39\lambda_0$
CP E-shaped Patch	9%	$0.1\lambda_{eff}$	$0.71\lambda_0$ x $0.36\lambda_0$

the best possible candidates. First, all the previous candidates were tested around 2.4 GHz in order to adequately compare their performance. Also, the thickness for all five candidates were adjusted to $0.1\lambda_{eff}$. In looking in Table 3.6, it can be seen that the CP E-shaped patch, Fig. 3.21d, yields the widest bandwidth out of all the candidates. It also has a proven ability to have dual resonance in axial ratio through the adjustment of its design parameters. However, it does have the largest profile out of all the candidates, containing an electrically large width. The CP U-slot patch, Fig. 3.21a, is moderately compact in size, featuring the second largest bandwidth among the candidates. Still, it also is the second largest electrically among the groups and can only provide a single resonance in axial ratio. The CP L-shaped probe patch, Fig. 3.21c, is also a solid candidate featuring a bandwidth similar to its counterparts and yielding the smallest profile. Like the CP U-slot patch, it can only provide single resonance in axial ratio. Moreover, 3D fabrication may become difficult in assembling the L-shaped probe. The TCPA design, Fig. 3.21b, is compact in size and quite straightforward to design. The difficulty lies in fabricating these

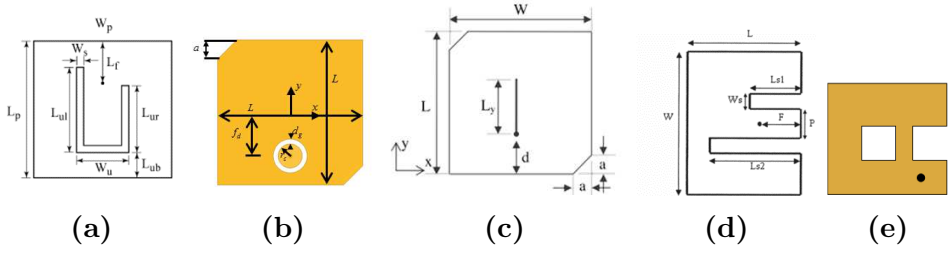

Figure 3.21: The element candidates for use in Mars rover DTE communications.

small gaps in higher frequencies. Also this patch can only provide single resonance in axial ratio. Finally, the CP half E-shaped patch, Fig. 3.21e, containing almost 50% of the size of its full E-shaped counterpart, yet still able to achieve adequate CP characteristics is a good candidate for Mars rover X-band communications. The CP half E-shaped patch is compact in size and has possible dual-resonance in axial ratio. From these results, the L-shaped probe patch was eliminated because of its difficult 3D fabrication. Moreover, the CP U-slot antenna was also removed from consideration because of its inability to achieve dual resonance in axial ratio. Therefore, the ring capacitor thick CP patch, E-shaped, and half E-shaped will be tested in the X-band frequencies to determine a final candidate. For the designs that had a single axial ratio resonance, higher bandwidth may be possible with thicker substrates.

3.8 Shifting from S-band to X-band

From the previous section, only the three of the remaining candidates will be tested in the X-band. The truncated corner patch antennas with a ring capacitor was chosen because their popular and simple design. An annular gap ring was introduced in order to remedy the narrow S_{11}/AR bandwidths the truncated corner antennas have. The S-band design was able to obtain roughly 140 MHz S_{11}/AR bandwidth (5.8% at 2.4 GHz). If this design was frequency scaled and increase the thickness, good performance may be obtained in both TX/RX bands in the required frequency range. The design was relatively straightforward, therefore, the design was frequency scaled, the probe size changed, the

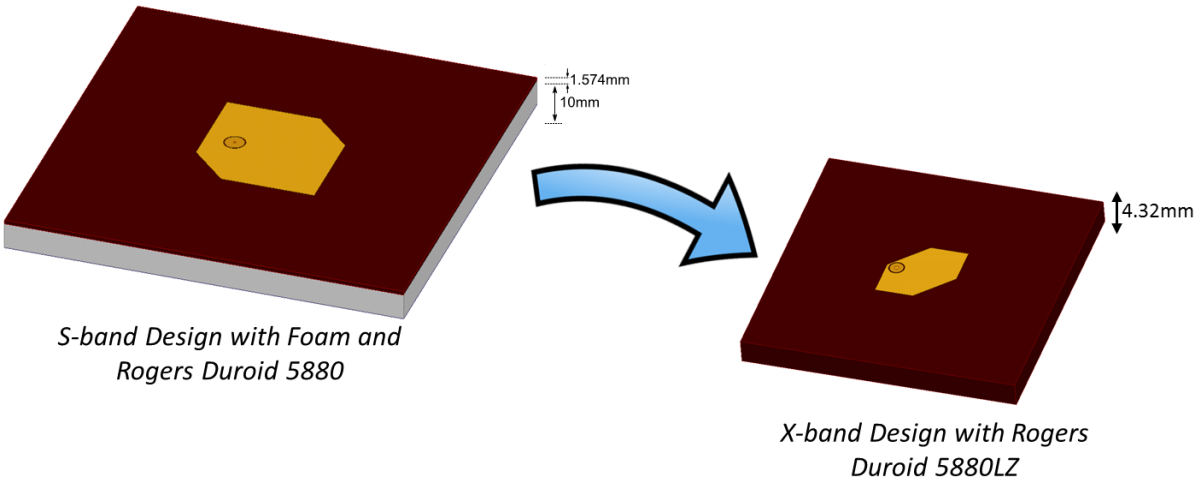

Figure 3.22: The simple design of the TCPA with annular ring allows for it to be easily frequency scaled to the X-band.

Table 3.7: Dimensions of the X-band CP TCPA in mm ($\epsilon = 1.96$)

L	W_g	L_g	h	a	d_f	r_p	d_g
11.9	51	51	4.32	4.25	3.5	1.22	0.25

height increased, and the design was retuned, shown in Fig. 3.22. The resulting design is electrically thick, with a thickness of $0.17\lambda_g$ for 8.425 GHz. The tuned parameters are shown in Table 3.7 and a respective drawing is shown on Fig. 3.23. As shown in Fig. 3.24a, the annular ring was able to produce a wide impedance bandwidth in both the required frequencies. In fact at 8.425 GHz, the S_{11} level is less than -15 dB. In looking at the AR performance of the patch element, Fig. 3.24b shows that the annular ring was able to produce desired CP characteristics at 8.425 GHz. Since the $S_{11} \leq$ -10 dB and the AR $\leq$ 3 dB, the patch element meets desired criteria. However, at the other desired frequency of 7.167 GHz, CP characteristics were not achieved where the AR is $\geq$ 3 dB even after much lengthy tuning. In addition to this, the CP TCPA with annular gap has good broadside radiation as shown in Fig. 3.25, but at the higher frequency of 8.4 GHz, the patterns suffer from high cross polarization levels and beam bifurcation. The directivity and cross-pol ratio are shown in Table 3.8.

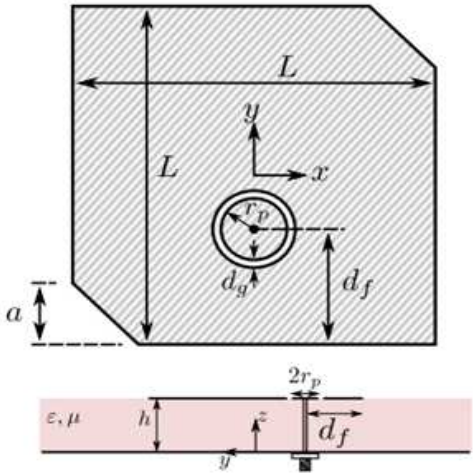

Figure 3.23: CP TCPA with Annular Ring.

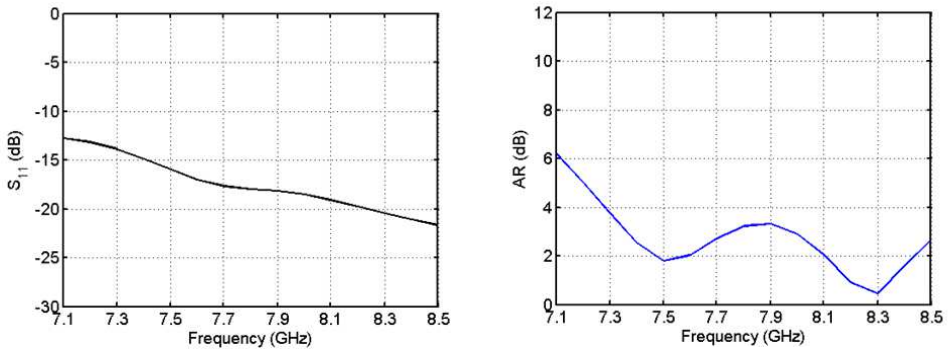

(a) $|S_{11}|$ Performance **(b)** AR Performance

Figure 3.24: The X-band design for the CP TCPA is able to achieve characteristics at TX (8.425 GHz).

Table 3.8: Directivity and X-Pol Ratio of the CP TCPA at the X-band

Directivity at Broadside	Directivity	X-Pol Ratio
XZ Plane (7.1 GHz)	7.4 dB	-9 dB
YZ Plane (7.1 GHz)	7.4 dB	-9 dB
XZ Plane (8.4 GHz)	3.8 dB	-2.8 dB
YZ Plane (8.4 GHz)	3.8 dB	-2.8 dB

The truncated corner with annular gap ring was able to achieve the desired S_{11}/AR bandwidth requirements only for a single desired frequency. Unfortunately because of the small dimensions of the annular gap necessary in the X-band frequencies, fabrication of

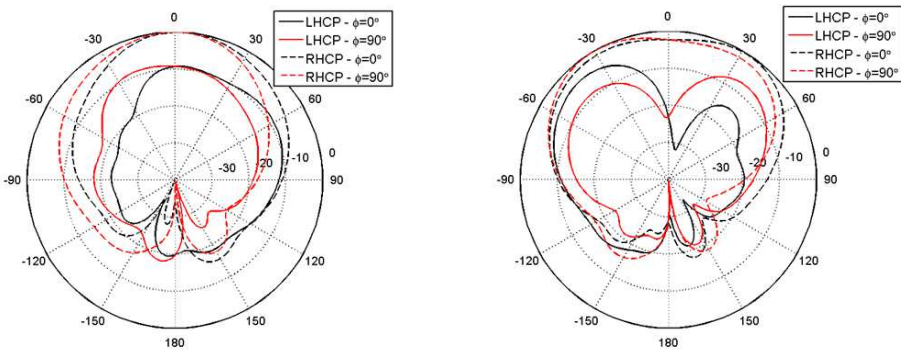

(a) $f = 7.167$ GHz **(b)** $f = 8.425$ GHz

Figure 3.25: The broadside radiation of the annular gap TCPA is good, but it suffers from high cross polarization levels and beam bifurcation.

the patch element may become too difficult. Therefore, a similar design was implemented using a parallel plate capacitor with similar dimensions. A sheet of Rogers Duroid 5870 was used for the parallel plate because it was readily available. The dimensions of this design is shown in Table 3.9 and with a top view of the element in Fig. 3.26. As shown in Fig. 3.27a, this configuration was able to also achieve a wide-band impedance bandwidth, with the S_{11} levels reaching $\leq$-15 dB at 8.425 GHz. Again like its counter part, this parallel plate capacitor design was able to produce desired CP characteristics at 8.425 GHz (AR $\leq$ 3 dB shown in Fig. 3.27b). Again, at the other required frequency of 7.167 GHz, the AR levels are quite high, reaching levels above 3 dB. This was the case even after much laborious tuning. When examining Fig. 3.28, good broadside radiation is achieved, and like the annular gap design, at 8.4 GHz, the design suffers from high cross polarization levels and beam bifurcation. Because of this, the CP TCPA in the X-band cannot meet adequate Mars rover DTE system-level requirements because of its inability of meeting S_{11}/AR bandwidth. The design also suffers from high cross polarization levels and low directivity even though it features a moderately compact patch profile.

From the two remaining candidates, the CP E-shaped patch provided the widest bandwidth in the S-band (2.4 GHz). The scaling procedure is outline in Fig. 3.29. The antenna will be redesigned in two steps. First, the antenna will be frequency scaled

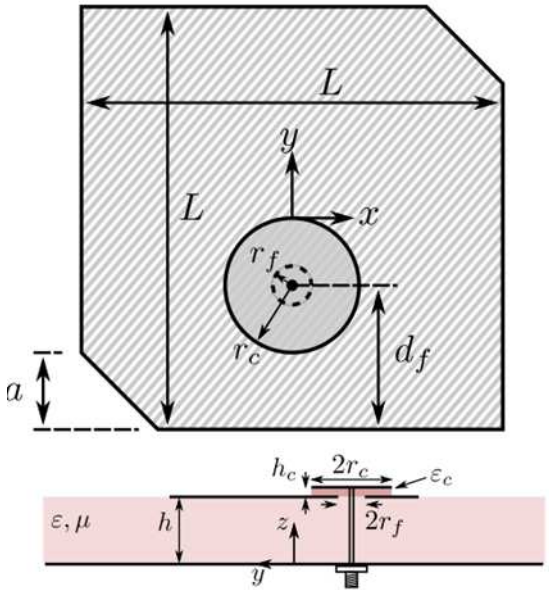

Figure 3.26: CP TCPA with Parallel Plate Capacitor.

Table 3.9: Dimensions of the X-band CP TCPA w/ Parallel Plate Capacitor in mm ($\epsilon = 1.96$ and $\epsilon_c = 2.33$)

h	L	W_g	L_g	a	d_f	r_f	r_f	h_c
4.32	11.9	51	51	5.1	4.93	0.96	0.85	0.17

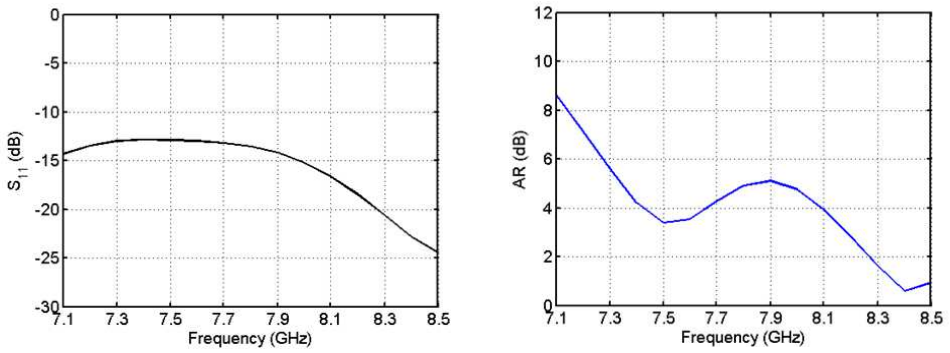

(a) $|S_{11}|$ Performance **(b)** AR Performance

Figure 3.27: The X-band design for the CP TCPA with Parallel Plate is again able to achieve characteristics at TX (8.425 GHz) like the annular gap design.

directly from the S-band to the X-band using a foam design. This will allow for a direct frequency scale of size. Next, this frequency scaled foam design will be changed to a

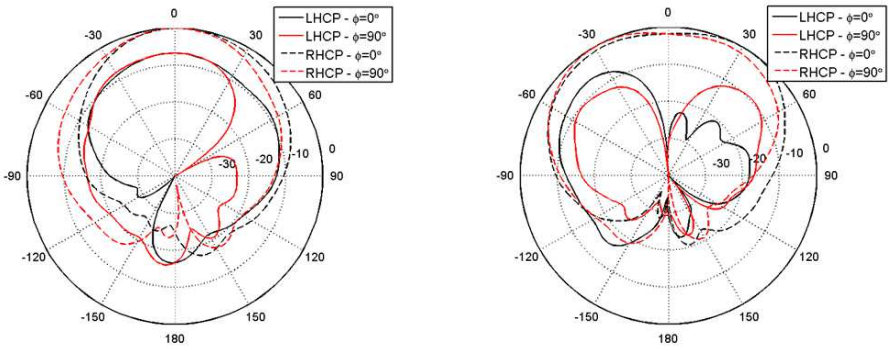

(a) $f = 7.167$ GHz **(b)** $f = 8.425$ GHz

Figure 3.28: The broadside radiation of the CP TCPA with Parallel Plate is also good but again suffers from from high cross polarization and beam bifurcation, like the annular ring design.

Table 3.10: Directivity and X-Pol Ratio of the CP TCPA with Parallel Plate Capacitor at the X-band

Directivity at Broadside	Directivity	X-Pol Ratio
XZ Plane (7.1 GHz)	6.88 dB	-6.75 dB
YZ Plane (7.1 GHz)	6.88 dB	-6.75 dB
XZ Plane (8.4 GHz)	4.31 dB	-3.7 dB
YZ Plane (8.4 GHz)	4.31 dB	-3.7 dB

Table 3.11: Final Design Parameters of E-shaped Patch at X-band (in mm)

Design	W	L	L_s	W_s	P_s	f_d	l
Small Probe	22.8	13.5	12.0	2.1	3.15	1.95	6.9
Typical Probe	22.8	13.5	12.0	1.7	4.25	2.15	7.3

Rogers Duroid 5880LZ, the substrate to be used for the final design. As shown in Section 3.5, Khidre's design was able to achieve wide bandwidth characteristics. Therefore, the first attempt is to scale this 2.4 GHz design into the X-band. The frequency scaling worked, but the scaled probe dimensions were much smaller than the typical probes used in measurements. The result is a design that contains poor S_{11} levels within the frequency band of operation. Therefore, the overall design was retuned to accommodate electrically larger probes.

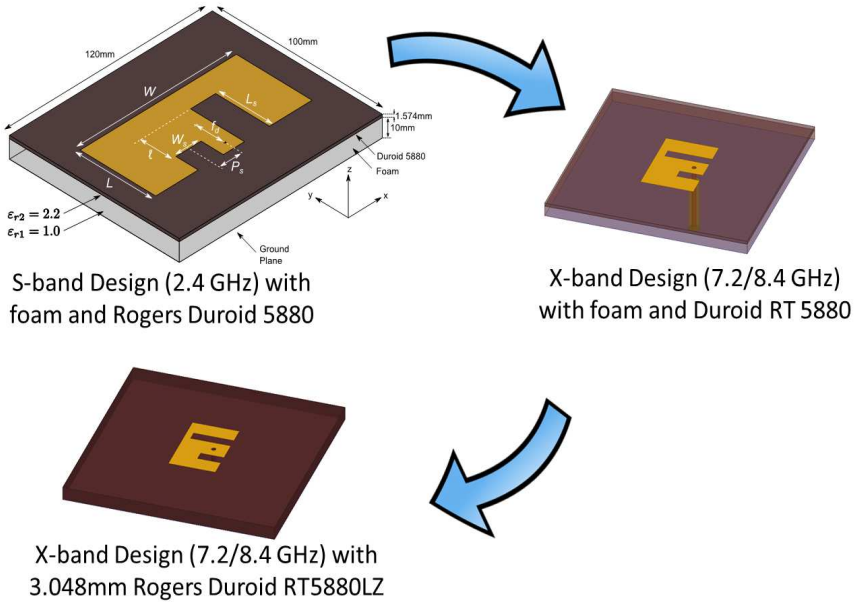

Figure 3.29: The CP E-shaped patch will be redesigned for use in the X-band in two steps.

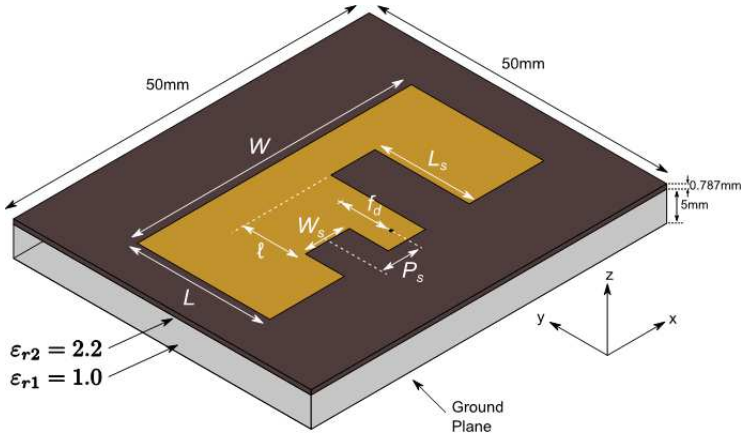

Figure 3.30: The CP E-shaped patch design, which was directly scaled from 2.4 GHz, had to be retuned to incorporate larger probes.

The final design parameters are listed in Table 3.11. As can be seen in Fig. 3.31, the S_{11} performance of the directly scaled design did not have good S_{11} performance because typical probes are much larger electrically than the probe included with the scaled E-shaped patch. After retuning, good S_{11} performance was achieved again. In looking at Fig. 3.33b, the X-band E-shaped design only contains a single AR resonance.

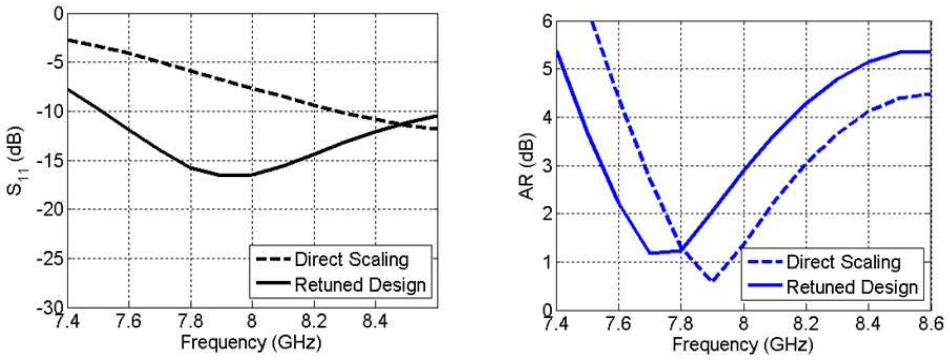

(a) $|S_{11}|$ Performance **(b)** AR Performance

Figure 3.31: Based on the S_{11} performance of directly scaled E-shaped design, retuning was necessary to achieve good S_{11} performance.

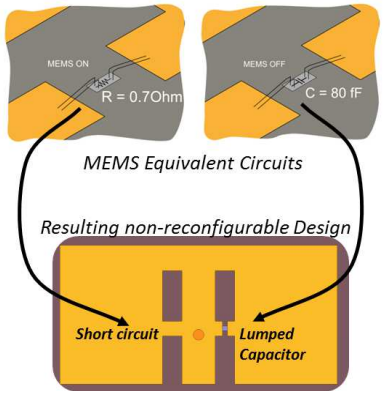

Figure 3.32: The concept of reconfigurability can aid in extending the AR bandwidth of the CP E-shaped patch element.

If this is the case, the design is again limited by the same limits as the previous TCPA with annular gap design which also only contained a single AR resonance. However, in literature, AR dual-resonance was possible through the use of a reconfigurable E-shaped patch antenna using MEMS switches [43]. In this application, reconfigurability is not needed, but this mechanism can be used to scale the E-shaped design to get wider bandwidth.

The reconfigurability was performed in [43] through the MEMS switches. The authors use two switches, assuming one switch was OFF and the other ON. In this Mars rover design, the non reconfigurability can be removed by replacing MEMS switches with their

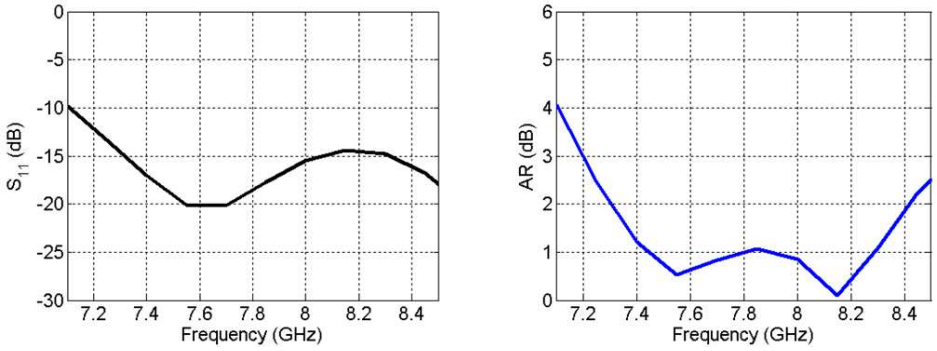

(a) $|S_{11}|$ Performance **(b)** AR Performance

Figure 3.33: Decent S_{11}/AR performance was achieved through the use of the lumped capacitor.

Table 3.12: Design Parameters of E-shaped Patch with Lumped Capacitor (in mm)

Design	W	L	L_s	W_s	P_s	f_d	l
With Capacitor	28.57	13.47	11.56	1.7	4.25	2.15	7.3

equivalent circuits, a short circuit for an ON switch, and a lumped capacitor for an OFF switch. This is shown graphically in Fig. 3.32. The resulting design should operate similarly to the previously shown design and can easily be scaled in length and capacitance. After manually tuning the design, decent performance was achieved through the use of the capacitor as shown in Fig. 3.33.

This design was also retuned after the frequency scaling to allow the use of typical sized probes. The dimensions of this design is shown in Table 3.12. The disadvantage of this design is that the width W is electrically large $0.8\lambda_0$ at 8.425 GHz. From these simulations, two types of of CP E-shaped patch antenna exist: a dual-resonance and a single-resonance type. It appears that the extra capacitance provides a little bandwidth boost for both AR and S_{11}. However, the goal is to create a design that avoids the use of a lumped element while maintaining proper dual-resonance capabilities.

The final candidate for consideration for X-band communication in Mars rovers is the CP half E-shaped patch antenna. Similar to the design of the full E-shaped patch

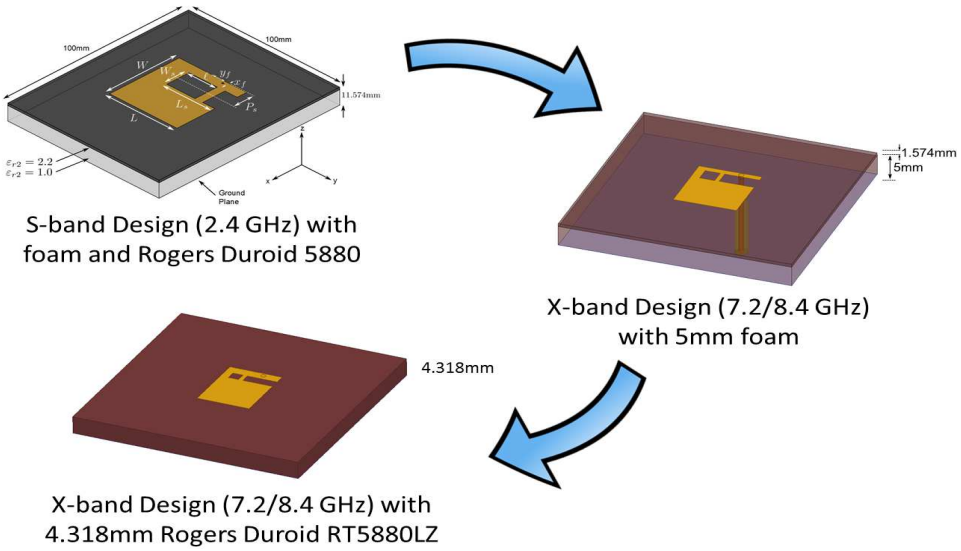

Figure 3.34: The CP E-shaped patch will be redesigned for use in the X-band in two steps.

Table 3.13: Dimension of the half E-shaped Patch in S and X Bands (in mm)

Design	W	L	L_s	W_s	P_s	y_f	x_f	l
S-Band	55.1	49.0	43.3	11.8	10.66	10.7	2.17	11.5
X-Band	15.0	13.5	11.7	3.3	3.03	2.56	0.7	3.29

antenna, the element will be redesigned using two steps.

First, the antenna will be redesigned by direct frequency scaling using a 5 mm foam design. Next, the foam design will be replaced with a Rogers RT 5880LZ. The disadvantage of the half E-shaped patch in the S-band design is that though it had a very wide-band S_{11} response, only a single resonance in AR was observed. When the S-band design was frequency scaled to X-band, a foam substrate was used. The height was arbitrarily set to 5mm. The design comparisons are listed below in Table 3.13.

As can be seen from Fig. 3.35, both the TX and RX bands were supported with good performance. A dual band feature of the CP half E-shaped is seen, which leads to a wide-band CP design, 24% S_{11}/AR bandwidth. In fact, the TX band contains very good CP performance, the $S_{11} \leq -15$dB and AR $\leq$ 3dB.

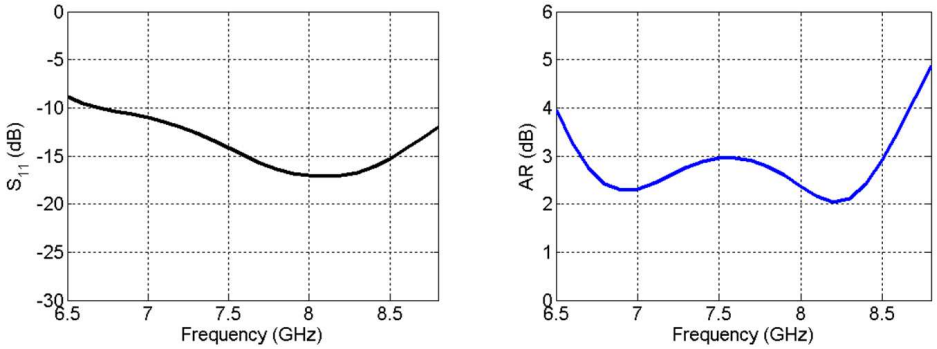

(a) $|S_{11}|$ Performance **(b)** AR Performance

Figure 3.35: The half E-shaped patch antenna was able to have good performance in the X-band, 24% CP bandwidth.

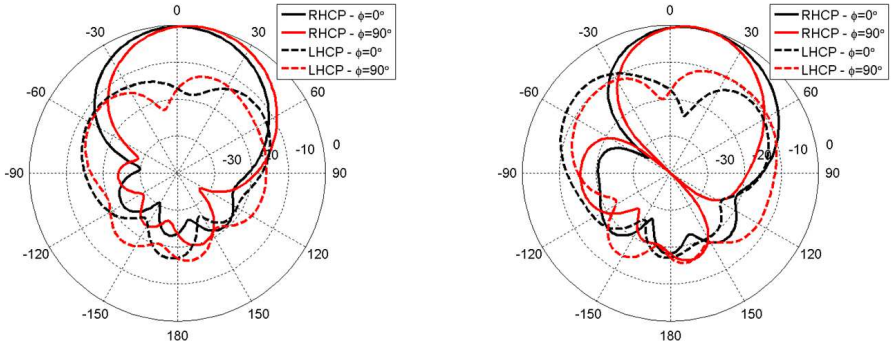

(a) $f = 7.167$ GHz **(b)** $f = 8.425$ GHz

Figure 3.36: The CP half E-shaped patch element using a foam substrate performs well in the X-band, even with a slight beam tilt.

Table 3.14: Directivity and X-Pol Ratio of the CP half E-shaped in the X-band using Foam Substrate

Directivity at Broadside	Directivity	X-Pol Ratio
7.167 GHz	8.87 dB	-11.41 dB
8.425 GHz	7.29 dB	-6.25 dB

In looking at the radiation patterns, decent radiation is observed. As can be seen from Fig. 3.36, good radiation is achieved in the broadside, but as shown in Fig. 3.38b, slight beam tilt exists. This phenomenon is similar to that observed for the CP E-shaped patch antenna in [15].

Table 3.15: Comparison of the Foam and 5880LZ Substrate Design of CP half E-shaped Patch (in mm)

Design	W	L	L_s	W_s	P_s	y_f	x_f	l
Foam	15.0	13.5	11.7	3.3	3.03	2.56	0.7	3.29
5880LZ	15.1	11.5	9.8	3.0	3.3	1.6	0.9	2.3

The author points out that the beam tilt is likely due to the abrupt phase shift in the electric field components observed above the antenna aperture. This represents a quasi TM_{11} modal distribution. Notice also that this occur in the higher frequency of the dual-band operation. Therefore, it may be noted that the beam tilt in the half E-shaped patch in the higher frequency in 8.425 GHz, is most likely due to the phase variations of the fields above the half E-shaped patch. While the cross-polarization is somewhat high, it will also be lower in the array environment.

As can be seen from the previous results, the X-band CP half E-shaped patch element provided good performance characteristics. Unfortunately, foam is not easily deployed in space, and thus, it is necessary to employ another low permittivity material. Rogers Duroid 5880LZ provides $\epsilon_r = 1.96$, and has good mechanical characteristics. To maximize bandwidth, we use thick substrates. Rogers' thickest substrate was 4.318 mm, so this was used. Again, the parameters were tuned to the dielectric constant of 1.96 until good AR and S_{11} performance was obtained. The final design dimensions are listed in Table 3.15.

Even with the RT Duroid 5880LZ material, good S_{11}/AR performance is still achieved in both TX/RX bands. In looking at Fig. 3.37, a dual-band feature of the CP half E-shaped patch antenna is observed, similar to that of the foam substrate. The advantage using this substrate is that the dual-band feature is much more distinct that its foam substrate counterpart. For the radiation patterns, as shown in Fig. 3.38, good radiation patterns are observed in both TX/RX bands. Although higher cross polarization levels are observed for the TX frequency, it will likely be decreased in an array environment. The beam tilt still exists as the foam substrate design, and the cause is mostly likely due

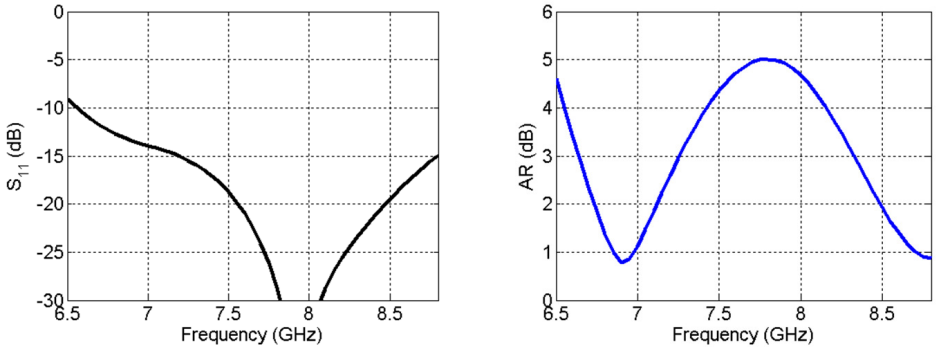

(a) $|S_{11}|$ Performance **(b)** AR Performance

Figure 3.37: The half E-shaped patch antenna using a Rogers Duroid 5880LZ substrate was able to provide a CP dual-band feature.

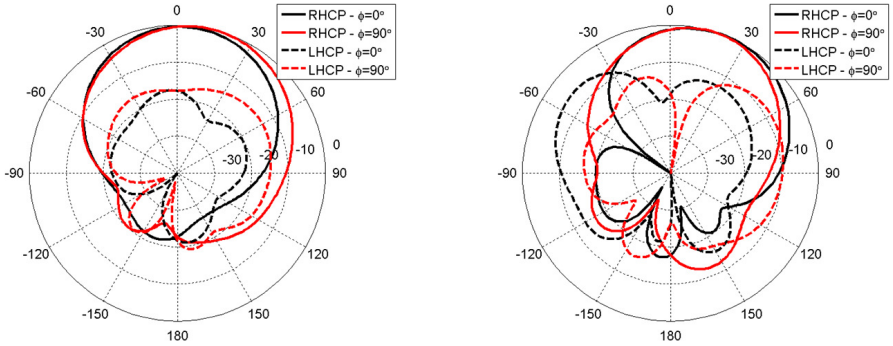

(a) $f = 7.167$ GHz **(b)** $f = 8.425$ GHz

Figure 3.38: Again, the radiation patterns of the CP half E-shaped patch element using a Rogers 5880LZ are decent, even in the presence of a beam tilt.

Table 3.16: Directivity and X-Pol Ratio of the CP half E-shaped in the X-band using Rogers 5880LZ Substrate

Directivity at Broadside	Directivity	X-Pol Ratio
7.167 GHz	8.13 dB	-13.02 dB
8.425 GHz	5.63 dB	-4.7 dB

to the same higher order mode shown in [15].

3.9 Development of the Chosen Patch Element

Overall, the three candidates, CP TCPA with annular gap, CP E-shaped patch, and CP half E-shaped patch contain various advantages and disadvantages. First, the CP TCPA using an annual gap was moderately compact in size. However, the S_{11}/AR requirements were only met for a single desired frequency. It was also difficult to fabricate the small annular gap. In terms of its radiation patterns, this design had high cross polarizations levels and low directivity. Therefore, the TCPA with annular gap is not a good candidate for X-band DTE Mars rover communications. For the CP E-shaped patch, dual resonance was achieved through the use of a lumped capacitor. The problem with this design is that the use of lumped capacitors can add other parasitic effects in higher frequencies. Moreover, the CP E-shaped patch is electrically large in width. The last candidate, CP Half E-shaped patch, was able to achieve dual resonance characteristics in the X-band. Also, it is compact in size. The disadvantage lies in the lower directivity in the TX band. In comparing each of these elements, the CP half E-shaped patch provides the best performance with minimal issues. The other elements do not meet the performance requirements as well as the half E-shaped patch and were a little too large for use in an array environment. Therefore, the goal is to continue to optimize, tune, fabricate, and measure the CP half E-shaped patch.

In order to validate the simulation results of the half E-shaped patch element, the design was fabricated using a chemical etching process available at the UCLA Center for High Frequency Electronics (CHFE). Because of the small dimensions associated with the design, as can be seen in Table 3.15 for the 5880LZ design, some of the metal was removed, seen in Fig. 3.40a, when the probe hole was being drilled. An attempt was made to repair the connection using solder, but the performance was lackluster as shown in Fig. 3.40b. Therefore, in order to improve the fabrication process, the bar that connects to the probe was widened.

Because impedance matching is primarily guided by the longitudinal location of the

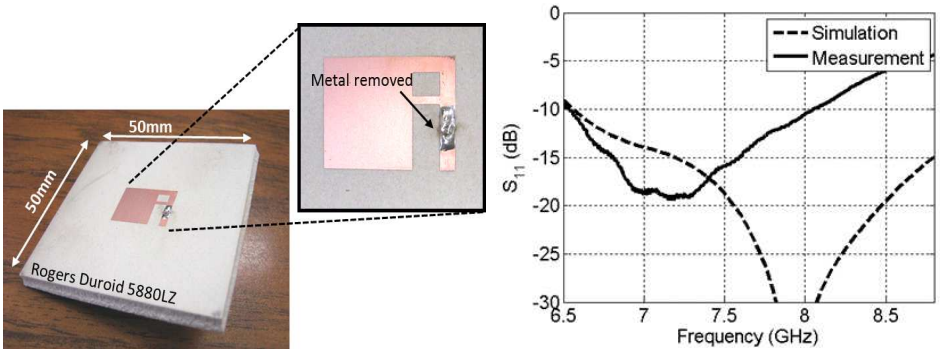

(a) **(b)** $|S_{11}|$ Performance

Figure 3.39: The bar is quite thin which caused some of the metal to be removed during the drilling process. Because of this, poor impedance matching was observed with this prototype.

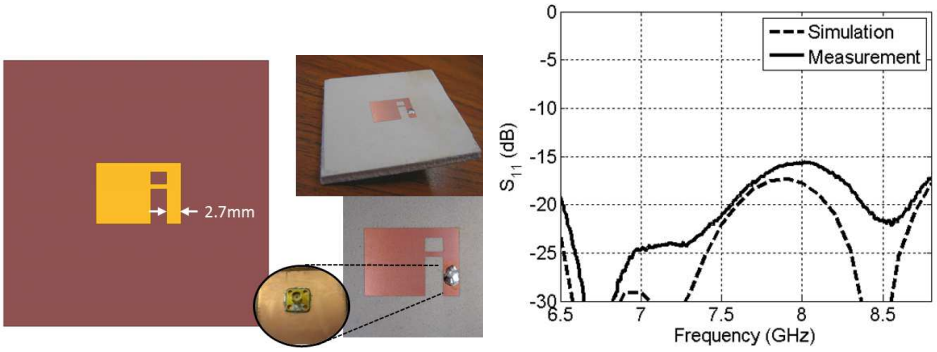

(a) **(b)** $|S_{11}|$ Performance

Figure 3.40: By extending the bar, the fabrication of the element was eased and good S_{11} performance was observed.

probe within the bar, widening had minimal effects on the overall AR/S_{11} performance. Next, the axial ratio was measured through the use of two measurement techniques: spinning linear and near-field measurement. While the S_{11} matched the simulation fairly well, the axial ratio was quite different. It appears that the AR is shifted slightly higher in frequency as can be seen in Fig. 3.41. This means that the design may need to be scaled larger.

The AR can also be observed by the decrease in cross-pol for the RX band and increase in cross-pol in the TX band radiation patterns as shown in Fig. 3.42. In comparing Fig.

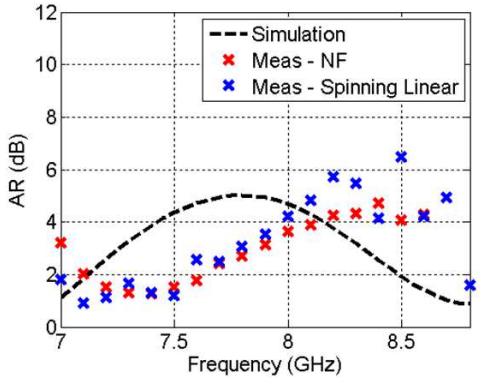

Figure 3.41: The axial ratio measurements did not match well with those of measurements. The design may need to be scaled larger.

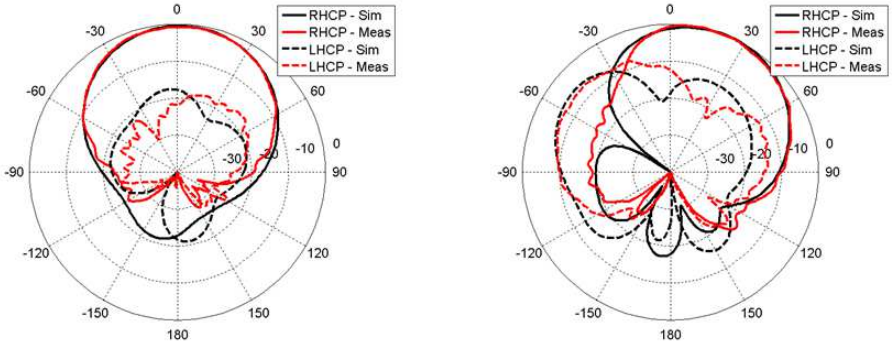

(a) $f = 7.167$ GHz **(b)** $f = 8.425$ GHz

Figure 3.42: Both the simulation and measurement radiation patterns, $\phi = 0^o$ cut, show that higher cross-polarizations are leading to higher AR levels.

Table 3.17: Comparison of Dimensional Changes Between Simulation and Fabrication (in mm)

Design	W	L	L_s	W_s	P_s	y_f	x_f	l
5880LZ	15.1	11.5	9.8	3.0	3.3	1.6	0.9	2.3
Fabrication	15.77	11.3	9.55	3.05	4.01	2.77	1.27	2.21
% Error	4.43%	-1.74%	-2.55%	1.67%	21.5%	73.1%	41.1%	-3.91%

3.42a with Fig. 3.42b, higher cross polarization levels are achieved in the higher frequency. This matches well with the measured results of the AR in Fig. 3.41. Overall, the patterns have fairly good agreement when looking at the co-polarization patterns.

Because of these discrepancies and mismatches between simulation and measurement

Figure 3.43: The actual dimensions of the parameters in the CP half E-shaped patch element were measured and compared with simulation data.

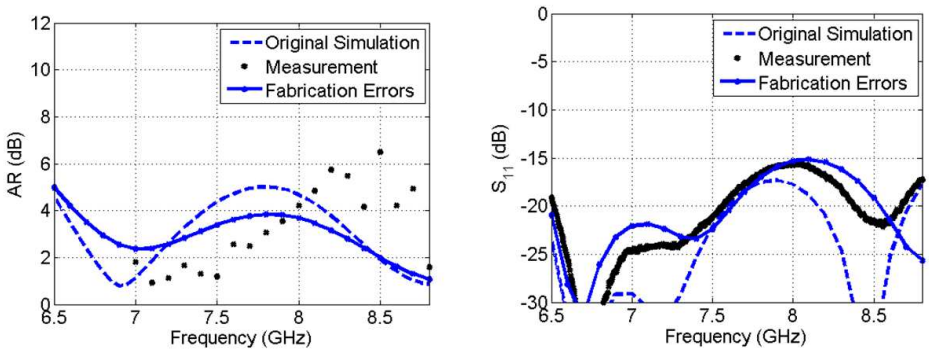

(a) $|S_{11}|$ Performance **(b)** AR Performance

Figure 3.44: Both the S_{11} and the AR performance of the fabrication were in agreement with previous results.

data, the fabrication tolerances on the antenna dimensions were studied. This was done under a microscope through the use of a caliper to measure the actual dimensions of the CP half E-shaped patch antenna. As can be seen from Table 3.17, the fabrication dimesnsions are slightly different from the design dimensions where the largest change occurred for y_f, P_s, x_f. These parameters contain the largest percent error and are often difficult to measure accurately. Regardless, these dimensions were inserted into HFSS to see what kind of effects these had into the S_{11} and the AR of the patch element.

As can be seen in Fig. 3.44, the S_{11} simulation results due to the fabrication dimensions, shown in Table 3.17, are in agreement with those of previous results. The AR levels

at the required frequencies are also similar to those of past measurements. Therefore, more investigation may be necessary to fully characterize the effects of the dimension in the antenna. Overall, the CP half E-shaped patch element is a good candidate to achieve proper Direct-to-Earth (DTE) system level requirements for use in an array environment.

CHAPTER 4

Study of Subarray Configuration

4.1 Design Candidates and Procedure for Comparison

Now that the individual element has been chosen and has been optimized to obtain the best X-band performance, a proper array configuration must be chosen to meet the gain requirements of the Mars rover DTE communication system. Often, the directivity, which is measured as the radiation intensity in a given direction from the antenna to the radiation intensity averaged over all directions [7], can be calculated through the use of the physical area of the array and the wavelength of operation. The gain can then be calculated from the directivity based on the antenna's aperture efficiency. In this design, the nominal footprint required is 38 cm by 38 cm by 5 cm. Assuming a 100% aperture efficiency, the directivity can be calculated using

$$D_0 = \frac{4\pi A_{em}}{\lambda^2} \tag{4.1}$$

where A_{em} is the effective area of the antenna, λ is the wavelength, and D_0 is the directivity [7]. Through a first order approximation, the effective area of the antenna can be assumed to be equal to the physical area of the antenna. If this was the case, a directivity, of about 32.05 dB can be achieved in the TX and 30.57 dB can be achieved in the RX using this antenna topology. One of the ways to achieve these directivity and gain requirements within this compact size requirement is through the use of an array architecture. Because of this, careful selection of the array topology and the required element spacing is necessary to avoid grating lobes. Also, subdividing the whole array into subarrays creates a more

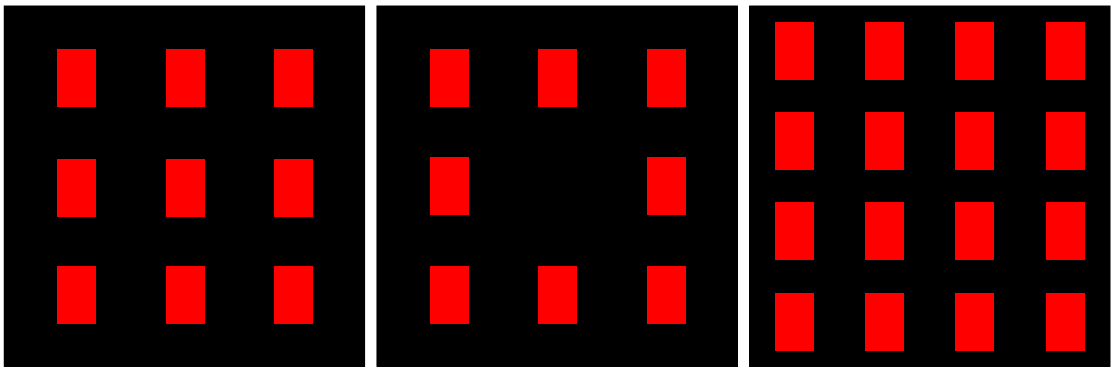

(a) (b) (c)

Figure 4.1: The following subarray topologies will be compared in order to choose the topology that meets requirements: 3x3 subarray, 3x3 without center subarray, and 4x4 subarray.

modular design that can be fabricated through the use of a chemical etching process available at the facilities in UCLA such as the Center for High Frequency Electronics. Dividing the overall array into various subarrays can also help create a scalable design in case additional modifications are necessary or for use in future missions. Therefore, this chapter will first discuss what available subarray topologies are available that can avoid grating lobes while still meeting gain requirements. For each of these subarray topologies, the UCLA DUAL program will be used to simulate the radiation patterns from these subarray topologies and understand the appropriate spacing between elements. At the end of this discussion, the proper subarray topology will be chosen and a feed network will be designed to support the topology. And finally, the optimized patch element will be simulated in the subarray architecture in preparation for integration of all the components in this antenna system.

The given aperture size is electrically large, almost 10λ's in the TX frequency. To help ease the simulation process, create a more modular and scalable design, and allow fabrication in nearby facilities, the overall array is going to be subdivided into subarrays. The reason for broadside radiation is because this allows for ease of design. Electronic steering of the beam often requires complex feed networks that provide the required progressive phase shift within a band of interest [7]. To allow for beam steering, the

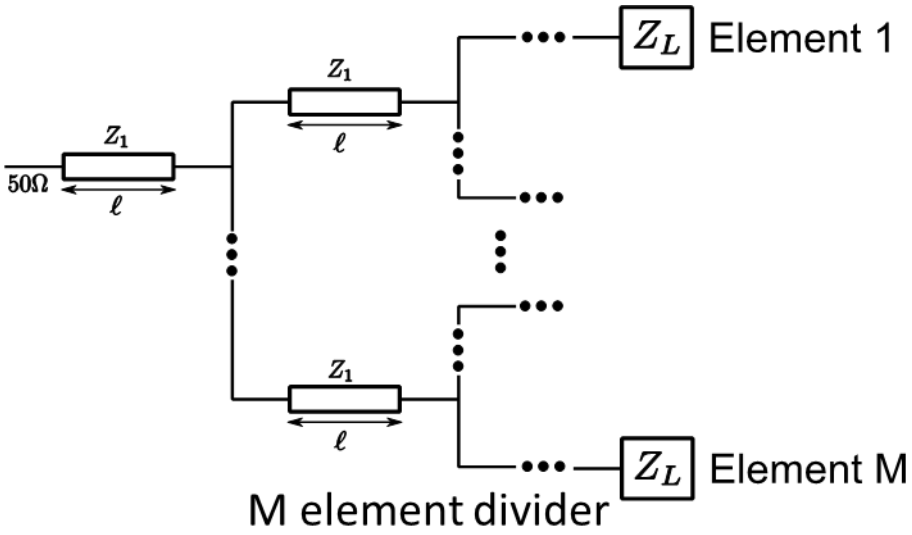

Figure 4.2: The feed network is going to consist of an M element power divider depending on the subarray topology.

antenna array will be connected through a mechanical gimbal, that allows for rotation to point the beam properly so as to create a link between the Mars rover and one of the deep space networks on Earth. Overall, the use of a 2x2 subarray topology would have resulted in the appearance of grating lobes because the element spacing would have been too large. Thus, a subarray topology that incorporates a higher number of elements must be used without the elements in direct contact with each other. Three of the design candidates are available: 3x3 subarray, 3x3 without center subarray, and 4x4 subarray. Each of these subarray topologies will be investigated in a methodical manner such as comparing the directivity each of the subarray topologies achieve. Other aspects of the subarray topology will require more effort to adequately compare among the candidates such as the effect of mutual coupling. Feed networks, radiation patterns, and directivity are aspects that will be investigated extensively. However, the effect of mutual coupling indirectly affects the performance. Because of this, the arrays will be compared based on the minimal element spacing. Therefore, for each subarray topology, the following parameters of interest: design of the feed network, grating lobes, directivity, and mutual coupling.

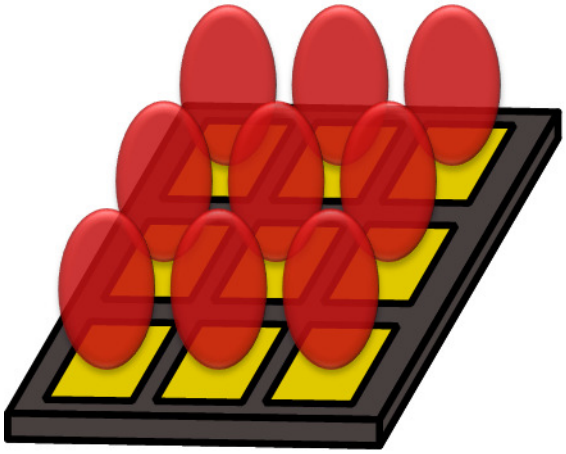

Figure 4.3: A $\cos^q(\theta)$ element pattern for each of the element is assumed. The array pattern and directivity will be calculated for the configurations.

For the feed network design, striplines will be used in order to avoid unwanted radiation. One of the most important aspect when comparing feed network design among the subarray topologies is whether a logical and systematic design can be achieved. Specifically, this means that within the given required space within the dimension, the feed network must provide equal amplitude, equal phase, and good impedance matching. Therefore, when comparing the topologies, the design that meets these criteria will be recommended.

Moreover, to compare the radiation pattern for each subarray topology, the UCLA DUAL program will be used to simulate the radiation performance. It was assumed that each of the elements has a $\cos^q(\theta)$ element pattern because the elements are going to consist of patch antennas which typically have good broadside radiation. The DUAL program computes the radiation using a brute force method for each (θ, ϕ) point on the pattern, where the path length from each element is computed and then all element contributions added with the proper phase. From here, the array pattern and directivity for the three topologies will be calculated.

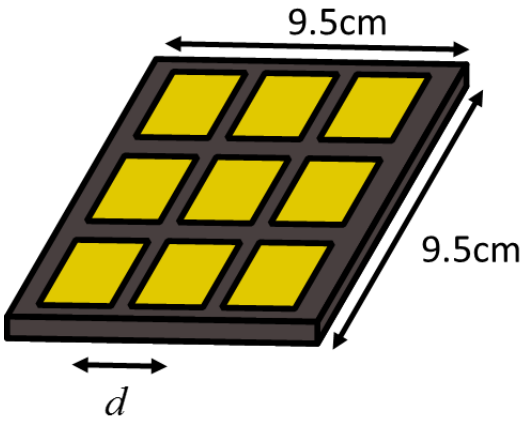

Figure 4.4: The first subarray topology to be studied is the 3x3 subarray.

4.2 3x3 Subarray

Based on the discussion on the past sections, one of the ways to evaluate the feasibility of a subarray topology is through the design of the feed network. When deciding the feasibility of the feed network design for the 3x3 subarray topology, the feed network is non-intuitive and difficult. Obtaining equal phase and equal magnitude on each element remains a challenge. Therefore, only the radiation pattern and directivity were investigated.

The UCLA DUAL program was used to simulate the radiation pattern and calculate the directivity assuming a $\cos^q(\theta)$ element pattern for each element. Also, the element spacing has been studied to determine an element spacing that gives the maximum directivity without the appearance of grating lobes. According to [4], the element spacing can be determined for any phased array to avoid grating lobes.

$$d \leq \frac{\lambda}{1 + |cos\theta_0|} \tag{4.2}$$

where θ_0 is the direction of the maximum of the radiation. Since the array is designed to radiate in the broadside, the element spacing required, based on this formula, must be less than $d < \lambda$. Not only is grating lobes important, but also the choice of element spacing is critical in order to avoid unwanted effects such as mutual coupling. And

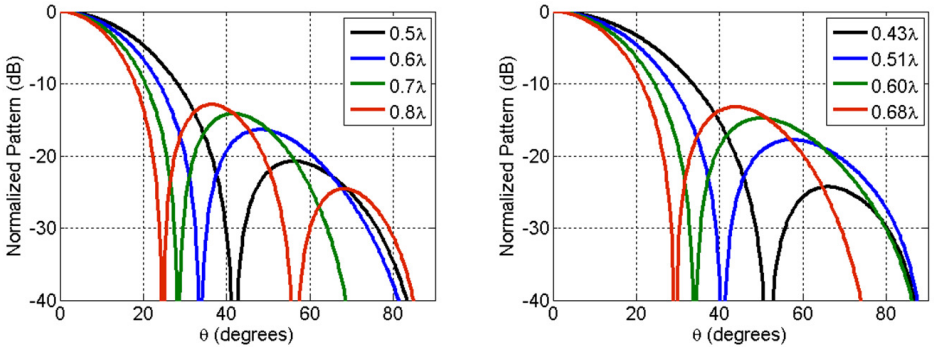

(a) **(b)**

Figure 4.5: The radiation pattern, $\phi = 0^o$ cut, of the 3x3 subarray topology was simulated using the UCLA DUAL program. Various element spacings were simulated in both the TX (a) and RX (b) frequencies.

Table 4.1: Directivity (in dB) of the 3x3 Subarray Topology with Various Element Spacing

Spacing RX/TX	Directivity at RX	Directivity at TX
0.42λ/0.5λ(17.97mm)	14.09 dB	15.52 dB
0.51λ/0.6λ(21.32mm)	15.37 dB	16.74 dB
0.59λ/0.7λ(25.08mm)	16.38 dB	17.79 dB
0.68λ/0.8λ(28.42mm)	17.31 dB	18.72 dB

finally, the physical area of the antenna also dictates the proper element spacing, thus determining directivity. Moreover, for the edge elements, it is important to have adequate spacing between the edge of the structure and the edge elements to avoid asymmetry when combined with other subarrays to form the full array. This allows the spacing between edge elements of one subarray with another to have the same element spacing as the other elements. This idea is called uniform spacing of elements.

The radiation patterns were plotted using the same physical spacing in both RX and TX bands. Based on Fig. 4.5, decent side lobe performance was observed through all the cases. Typically, grating lobes would begin to appear at around 0.8λ, but because of the element patterns, grating lobes are not present [4]. As can be seen from Table 4.1, as the element spacing is increased, the directivity increases based on equation 4.1. Of course,

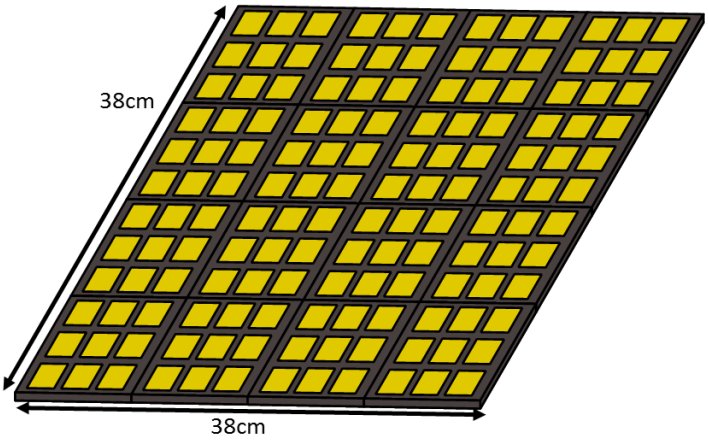

Figure 4.6: The 3x3 subarray has been configured and placed into a full array environment to determine its overall radiation characteristics.

the increase in directivity by increasing element spacing is limited by the appearance of grating lobes based on equation 4.2.

In order to determine if the subarray achieves the required directivity, the subarray must be inserted into a full array environment. The radiation pattern and directivity can still be calculated through the use of the UCLA DUAL program. However, when considering the full array, it may be of interest to consider the spacing assuming that the size is set. At both the RX and TX bands, the physical subarray spacing will be set to 9.5 cm. The change in distance between elements can help optimize the performance. Overall, the best configuration occurs when the elements are uniformly spaced, especially between subarray edge elements. In looking at both the patterns in Fig. 4.7 and the directivity in Table 4.2, the element spacing that achieves the requirements is when the elements among the array are uniformly spaced within a subarray and within the whole array topology. The maximum gain that is possible is therefore 31.50 dB in the TX and 30.1 dB in the RX. Smaller element spacing feature higher side lobe levels and have lower directivity levels. The reason for this is because the non uniformity of the element spacing between edge elements of each subarray tile. For smaller element spacing, the elements may be uniformly spaced within a subarray, but within the whole array topology, edge elements from one subarray to a different subarray are not spaced with the same element

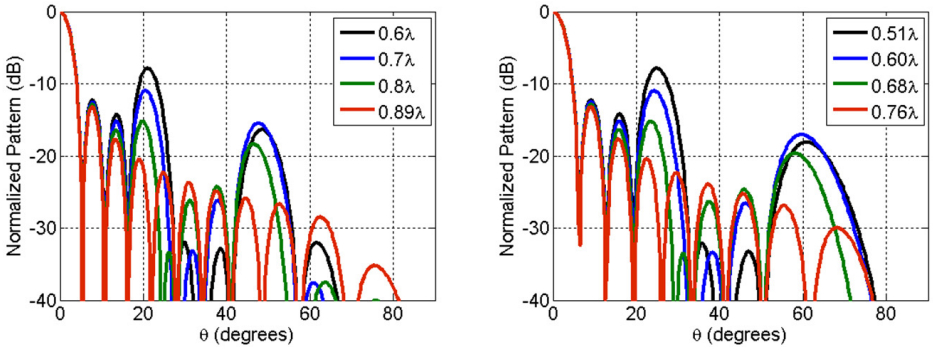

(a) (b)

Figure 4.7: The radiation pattern, $\phi = 0^o$ cut, of the 3x3 array topology was also simulated using the UCLA DUAL program. Various element spacings were simulated in both the TX (a) and RX (b) frequencies.

Table 4.2: Directivity (in dB) of the 3x3 Array Topology with Various Element Spacing

Spacing RX/TX	Directivity at RX	Directivity at TX
$0.51\lambda/0.6\lambda$ (21.36mm)	27.35 dB	28.73 dB
$0.60\lambda/0.7\lambda$ (24.93mm)	28.50 dB	29.88 dB
$0.68\lambda/0.8\lambda$ (28.49mm)	29.58 dB	30.98 dB
$0.75\lambda/0.89\lambda$(31.69mm)	30.12 dB	31.50 dB

spacing. This can be seen in Fig. 4.8. Overall, if a large spacing is chosen (> 28.4 mm), good directivity and decent radiation characteristics can be obtained in both RX and TX bands for the 3x3 subarray topology.

4.3 3x3 Without Center Element Subarray

Another topology that can be studied is the 3x3 subarray without the center element. The reason why this configuration may be appropriate is because the design of the feed network is possible. Using the average frequency between the RX and TX frequencies, the feed network has been designed at $f_c = 7.797$ GHz. The wavelength can be calculated using that the stripline network is designed using a RT Rogers 5880LZ material with a relative permittivity of $\epsilon = 1.96$.

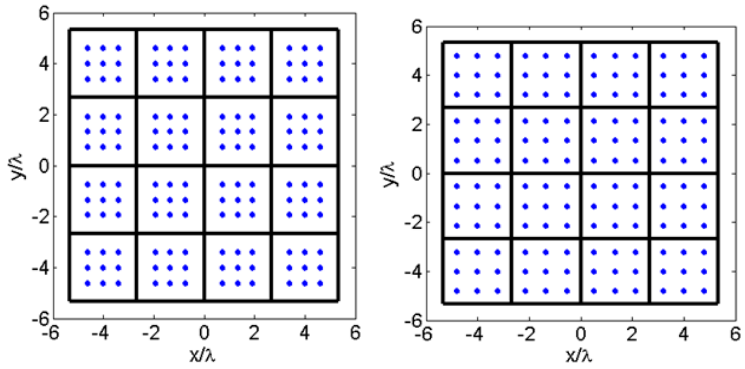

(a) **(b)**

Figure 4.8: As can be seen, the element spacing between subarray edge elements using d = 0.6λ at TX (a) and d = 0.8λ at TX (b) are not the same as the element spacing within a subarray. This introduces higher side lobe levels. Thus, increasing the element spacing until uniform spacing is achieved would produce optimal results.

$$\lambda = \frac{c}{f\sqrt{\varepsilon_r}} \tag{4.3}$$

Based on equation 4.3, the wavelength in this structure is 2.748 cm. A quarter wavelength transformer will then be 0.687 cm long. In looking at Fig. 4.10, the stripline to SMA connector will be placed in the center of the structure. Because of this, the feed network is symmetric, simplifying the design. After this design, the bandwidth of the feed network can be calculated using transmission line analysis. By calculating the input impedance of the stripline network, the impedance matching performance can be determined based on equation 4.4.

$$Z_{in}(-l) = Z_0 \left(\frac{Z_L + jZ_0 tan(\beta l)}{Z_0 + jZ_L tan(\beta l)} \right) \tag{4.4}$$

where Z_0 is the characteristic impedance of the line typically 50Ω, Z_L is the load impedance, and β is the propagation constant in the medium. Because of the symmetrical design of the feed network and the equidistance from the SMA connector to each element, the calculation was simplified. The S_{11} performance was then calculated by through the reflection coefficient.

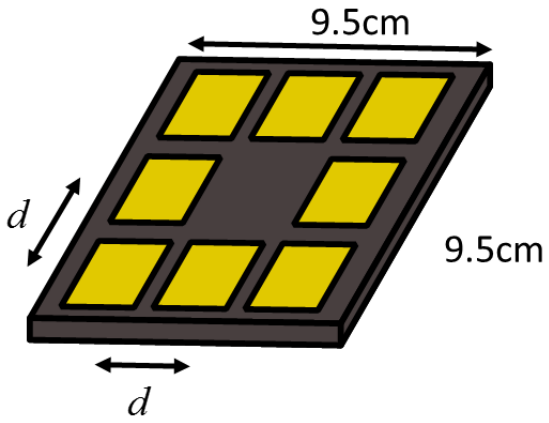

Figure 4.9: The 3x3 subarray without the center element is an appropriate design because a feed network design is possible.

Table 4.3: Directivity (in dB) of the 3x3 Subarray Without Center Element Topology with Various Element Spacing

Spacing RX/TX	Directivity at RX	Directivity at TX
0.42λ/0.5λ(17.97mm)	14.56 dB	15.86 dB
0.51λ/0.6λ(21.32mm)	15.52 dB	16.73 dB
0.59λ/0.7λ(25.08mm)	16.12 dB	17.42 dB
0.68λ/0.8λ(28.42mm)	16.72 dB	18.13 dB

$$S_{11} = \Gamma = \frac{Z_L - Z_0}{Z_L + Z_0} \tag{4.5}$$

Based on equation 4.5, the S_{11} performance was graphed and is shown in Fig. 4.11. The feed network is overall quite wide-band, where the S_{11} levels are below -10 dB for the whole frequency range between 6.5-9 GHz. The stripline network definitely achieves desired S_{11} levels at both RX (-20.6 dB) and TX (-27.3 dB). Therefore, the feed network design is successful.

As was done for the 3x3 subarray configuration, the radiation patterns using the UCLA DUAL program will be simulated for the 3x3 subarray without the center element. In this simulation, the element spacing again is changed until good radiation characteristics were obtained. In looking at Fig. 4.12, decent sidelobe levels are obtained. Low radiation

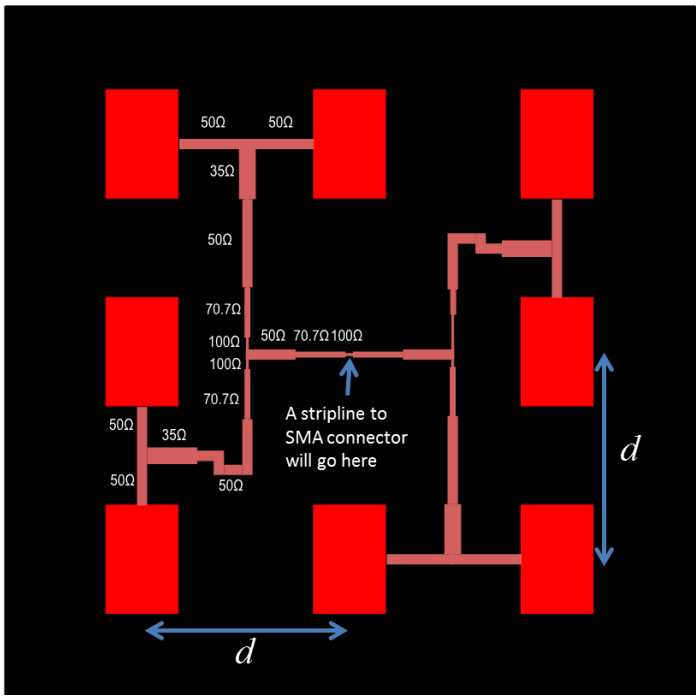

Figure 4.10: The feed network was designed around the average frequency between RX and TX. A RT Rogers 5880LZ substrate was used.

is also achieved towards the horizon ($\theta = 90^o$). This is observed for both RX and TX frequencies. The directivity achieved in this subarray topology is also listed in Table 4.3. Again, in order to adequately determine if the subarray topology meets the requirements of the Mars rover DTE requirements, the subarray must be considered in a full array environment shown in Fig. 4.13 . Again both investigations will be done in RX and TX frequencies and the subarray spacing used will be 9.5 cm. This full array configuration will also test whether the use of multiple subarrays will help lower side lobe levels. As shown in Fig. 4.14, high sidelobe levels are achieved leading to smaller directivity. The reason for the high side lobe levels is because of the missing element in the center of each subarray. The absence of the center element causes the element spacing between center elements to be greater than d $\geq \lambda$. Grating lobes begin to appear with this excess of spacing. The results show that the maximum directivity is achieved when uniform spacing is achieved. This is shown in Table 4.4, where 30.88 dB is the maximum directivity achieved in the TX and 29.53 dB is the maximum directivity achieved in the RX. Unlike the 3x3 subarray,

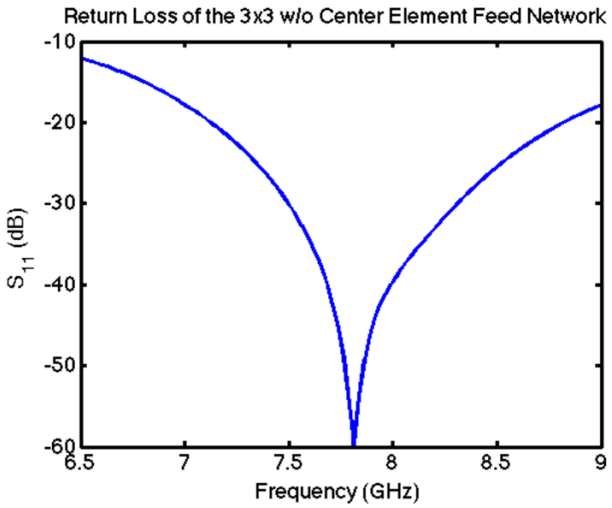

Figure 4.11: The S_{11} performance shows a resonance at the center frequency where the feed network is designed.

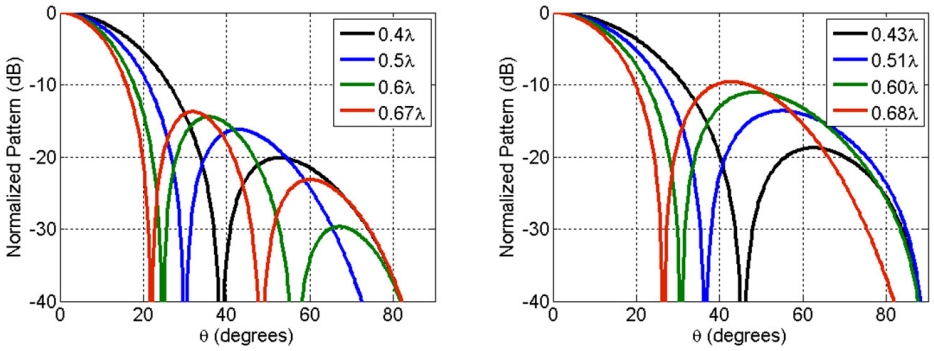

Figure 4.12: The radiation pattern, $\phi = 0^o$ cut, of the 3x3 subarray without center element topology was simulated using the UCLA DUAL program. Various element spacings were simulated in both the TX (a) and RX (b) frequencies.

the 3x3 subarray without the center element does not achieve at least 30 dB directivity in both frequency bands. However, as was shown previously, a systematic and symmetric feed network design for this subarray topology can be achieved.

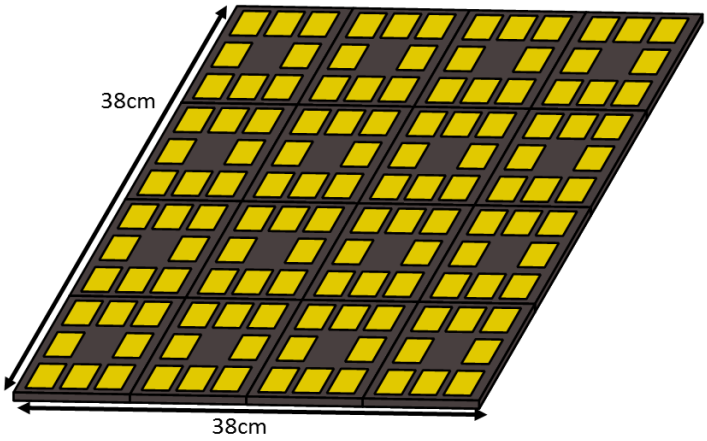

Figure 4.13: The 3x3 subarray has been configured and placed into a full array environment to determine its overall radiation characteristics.

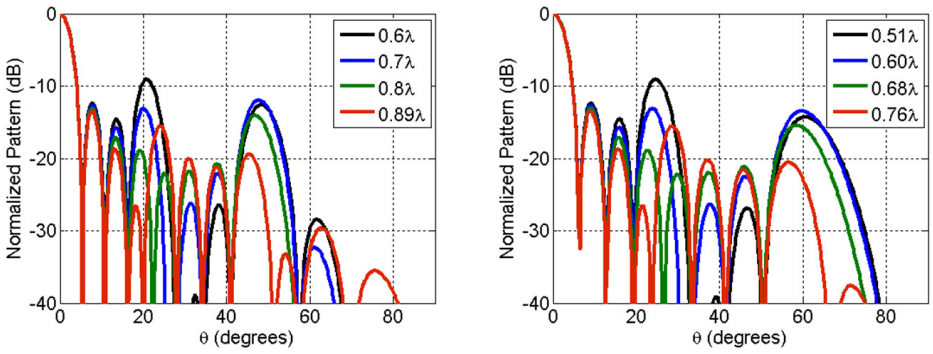

(a) **(b)**

Figure 4.14: The radiation pattern, $\phi = 0^o$ cut, of the 3x3 array without center element topology was also simulated using the UCLA DUAL program. Various element spacings were simulated in both the TX (a) and RX (b) frequencies.

4.4 4x4 Element Subarray

The subarray topology to be tested is the 4x4 subarray. Like the 3x3 subarray without center topology, the 4x4 subarray allows for a systematic feed network design as well. The placement of the elements in a 4x4 subarray topology allows a symmetrical feed network design as well. The reason for this is two fold. First, there are $2^4 = 16$ number of elements. A 1:2 power divider can be used multiple times and branched until 16 branches exist. Therefore, a 1:2 power divider can be used in four stages to feed 16 elements. And

Table 4.4: Directivity (in dB) of the 3x3 without Center Element Array Topology with Various Element Spacing

Spacing RX/TX	Directivity at RX	Directivity at TX
0.51λ/0.6λ (21.36mm)	27.47 dB	28.67 dB
0.60λ/0.7λ (24.93mm)	28.27 dB	29.49 dB
0.68λ/0.8λ (28.49mm)	29.09 dB	30.41 dB
0.75λ/0.89λ(31.69mm)	29.53 dB	30.88 dB

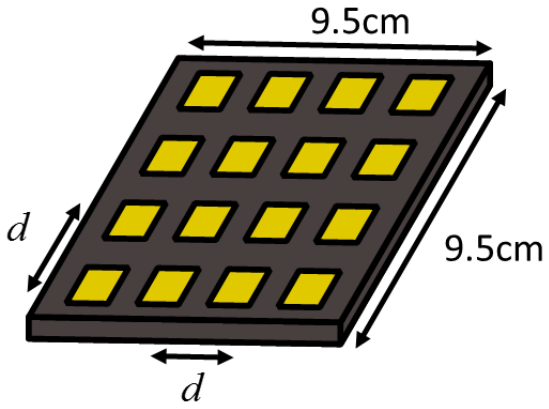

Figure 4.15: Another suitable candidate for Mars rover DTE communications is the 4x4 subarray topology.

secondly, a stripline to SMA connector can be placed in the center. This simplifies the design to allow for equidistance (enabling equiphase) and symmetric design.

Because the feed network design was possible, the bandwidth of the stripline network can be calculated using a similar transmission line analysis for the 3x3 subarray without center topology. Again because the feed network is symmetric and ports are equidistant from the input port, the calculation can be simplified. Through the use of equations 4.4 and 4.5, the S_{11} can be calculated. The results are shown in Fig. 4.17. Two designs were created, using the center frequency of 7.796 GHz and other using the TX frequency of 8.425 GHz. Both are good designs featuring a wide -10 dB S_{11} bandwidth. For now, both will be considered in the future designs and will be tuned appropriately to create the best design.

Next, the 4x4 subarray topology was simulated using the UCLA DUAL program to

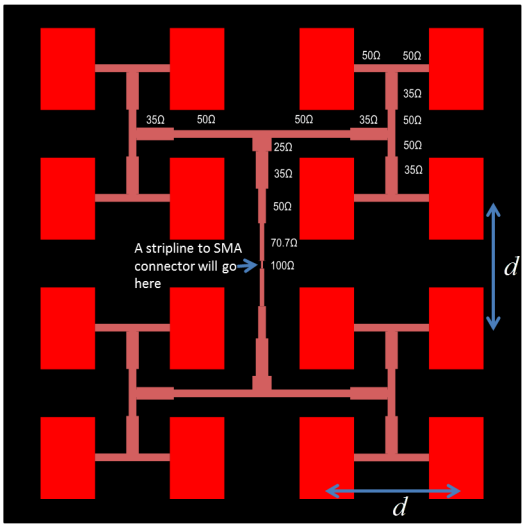

Figure 4.16: The 4x4 subarray topology is a feasible design because a feed network can be designed to specifications through its systematic approach.

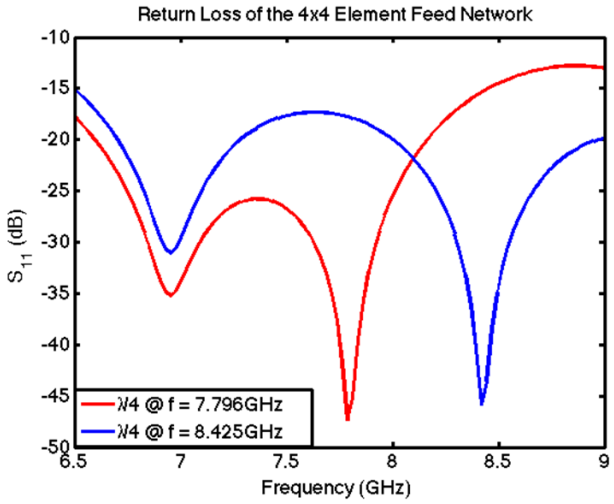

Figure 4.17: The S_{11} performance shows a resonance at the center frequency where the feed network is designed.

determine its radiation characteristics in both frequency of interest. As was done for previous topologies, the element spacing was studied to determine which gives the best directivity without grating lobes and minimizing side lobe levels. In looking at Fig. 4.18, the use of smaller spacing allows good sidelobe levels with minimal radiation towards $\theta = 90^o$. This is true for both TX and RX frequencies. When looking at Table 4.5, the directivity is higher compared to the 3x3 topologies due to the overall larger size. Again,

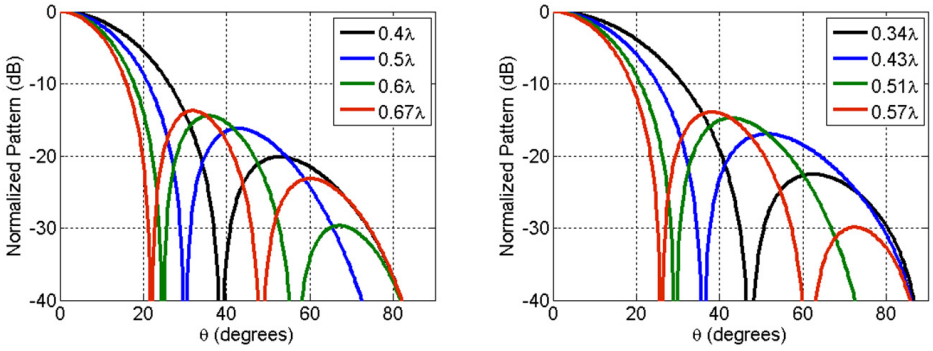

(a) **(b)**

Figure 4.18: The radiation pattern, $\phi = 0^o$ cut, of the 4x4 subarray element topology was simulated using the UCLA DUAL program. Various element spacings were simulated in both the TX (a) and RX (b) frequencies.

Table 4.5: Directivity (in dB) of the 4x4 Subarray Topology with Various Element Spacing

Spacing RX/TX	Directivity at RX	Directivity at TX
0.34λ/0.4λ (17.97mm)	14.72 dB	16.14 dB
0.42λ/0.5λ (21.32mm)	16.31 dB	17.72 dB
0.51λ/0.6λ (25.08mm)	17.64 dB	19.07 dB
0.57λ/0.67λ(28.42mm)	18.49 dB	19.89 dB

the 4x4 subarray was considered in a full array context. The investigation will again be at both RX and TX bands. The subarray spacing is set to 9.5 cm. The element spacing that gives uniform spacing is found to be 0.67λ at TX. As shown in Table 4.5, the largest gain that can be achieved with this configuration is 31.6 dB when using uniform spacing. This design results in an edge-to-edge distance of 4.4mm between the edge elements and the subarray edge. Fig. 4.18 shows that decent sidelobe levels are achieved with this uniform spacing in both RX and TX frequencies. Also, higher sidelobe levels are shown when using lower element spacings. Mutual coupling will definitely have an impact on this array performance, but an optimizer can be applied to provide good performance. Overall the 4x4 subarray topology offers great directivity and allows for a systematic feed network design.

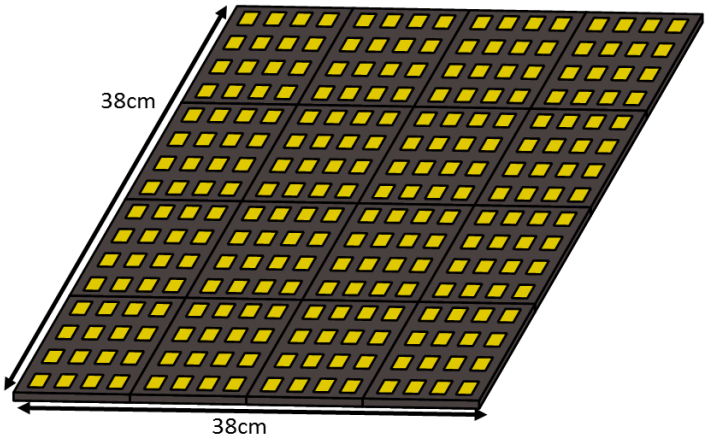

Figure 4.19: The 4x4 subarray was also placed in a full array environment to analyze its radiation characteristics. This was also compared to the previous two topologies.

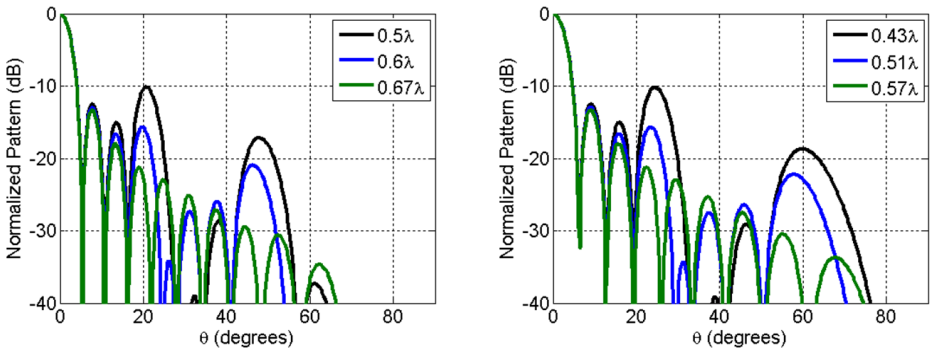

(a) **(b)**

Figure 4.20: The radiation pattern, $\phi = 0^o$ cut, of the 3x3 array without center element topology was also simulated using the UCLA DUAL program. Various element spacings were simulated in both the TX (a) and RX (b) frequencies.

4.5 Determination of Subarray Configuration

Now that each of the three topologies have been studied and investigated by simulating each of the subarray's radiation characteristics and designing a feed network, three subarray topologies can now be compared. Moreover, the subarray topologies radiation characteristics are compared in the full array environment. The 3x3 subarray topology, was able to provide a maximum directivity of 30.12 dB in the RX and 31.50 TX. The disadvantage of the 3x3 subarray topology is that the design of a feed network was difficult

Table 4.6: Directivity (in dB) of the 4x4 Array Topology with Various Element Spacing

Spacing RX/TX	Directivity at RX	Directivity at TX
0.43λ/0.5λ (17.80mm)	28.39 dB	29.72 dB
0.51λ/0.6λ (21.37mm)	29.77 dB	31.18 dB
0.57λ/0.67λ(23.86mm)	30.24 dB	31.64 dB

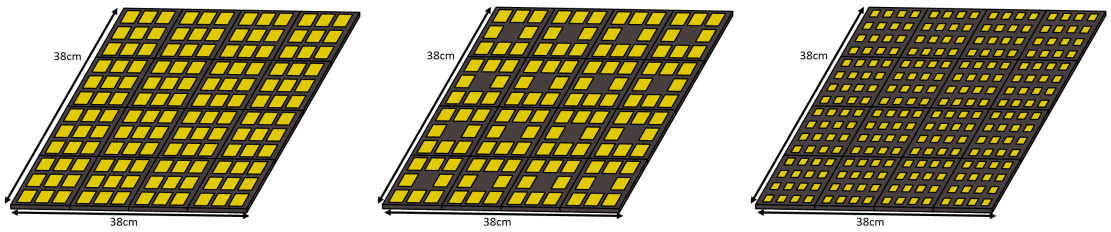

(a) **(b)** **(c)**

Figure 4.21: The three subarray topologies will be compared based on their radiation characteristics in the full array environment such as its sidelobe levels and directivity and feed network design.

and a systematic approach could not be formed. The 3x3 without the center element, however, was able to maintain a systematic feed network design that was able to achieve good S_{11} levels with equiphase characteristics. However the maximum directivity achieved at the RX of 29.53 dB does not achieve system requirements even though the maximum directivity achieved of 30.88 dB in the TX frequency does meet the requirements. Finally, the 4x4 subarray topology also offers a systematic design of a feed network with good S_{11} levels. And most importantly, the maximum directivity achieved is also greater than the required 30 dB necessary for Mars rover DTE communications, 30.24 dB in RX and 31.64 dB in TX. Of course in all three of the designs, the determination of the effect mutual coupling is still left to be determined. However, the only subarray topology that is able to maintain a systematic feed network design yet still meet the directivity and gain requirements is the 4x4 subarray topology. Because of this, the 4x4 subarray was chosen for the overall subarray topology in the Mars rover DTE communications system.

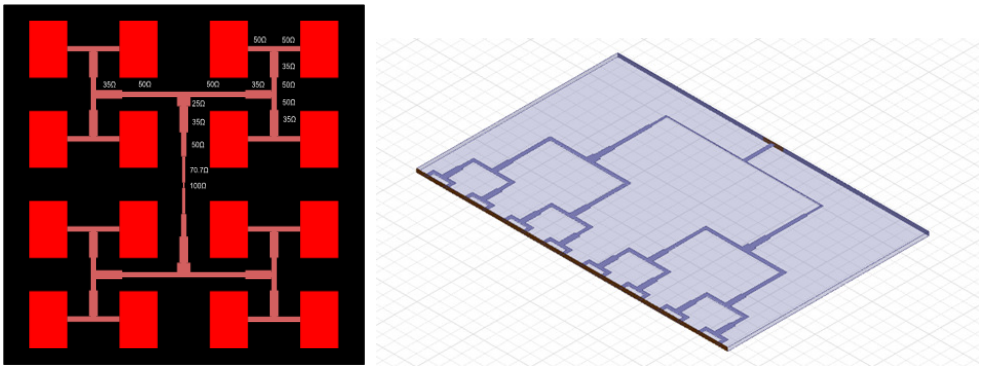

(a) (b)

Figure 4.22: The original design was simplified in HFSS in order to test the performance of the 4x4 subarray's feed network.

4.6 4x4 Subarray Network Design

In order to test the 4x4 subarray impedance matching performance further, a full-wave analysis is used using Ansys HFSS [27]. However, the layout was simplified, as seen in Fig. 4.22b, using an equivalent configuration. This is possible for testing purposes because through a transmission line analysis, both would yield comparable results. This also enables a simplified layout for prototyping purposes in this study. During the design process in HFSS, it was noticed that the S_{11} performance can be improved further at TX by sizing the quarter wave transformers at different frequencies than the TX frequencies. It was found that using 8.25 GHz is best as shown in Fig. 4.27. In this figure, the S_{11} for the TX frequency improved however at the cost of increased S_{11} levels at the RX frequency. Perhaps using more complex impedance transformers than that of quarter wave transformers can improve S_{11} levels. But for now, this performance is adequate for comparison.

As previously stated in the last sections, an equimagnitude and equiphase design is required for the feed network. The reason for this is twofold: to radiate the array in the broadside and to simplify the feed network design. Obviously through the use of more complex amplitude element patterns within elements [7], one can alleviate side lobe levels or reduce side lobe level beam widths. However, uniform arrays, which contains

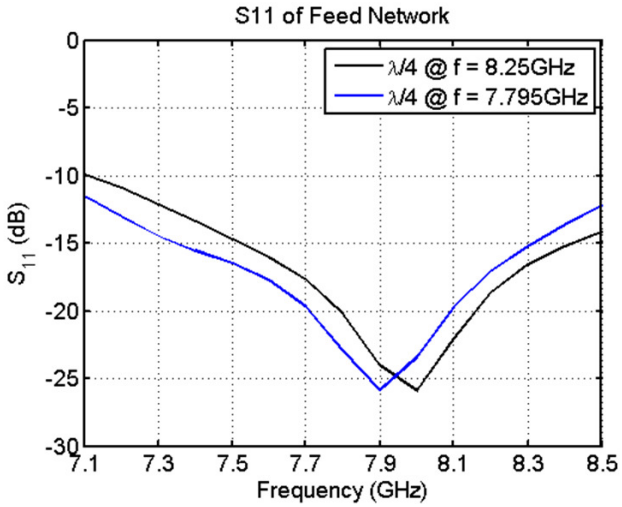

Figure 4.23: The S_{11} simulated performance of the feed network in HFSS show acceptable levels for Mars rover DTE communication.

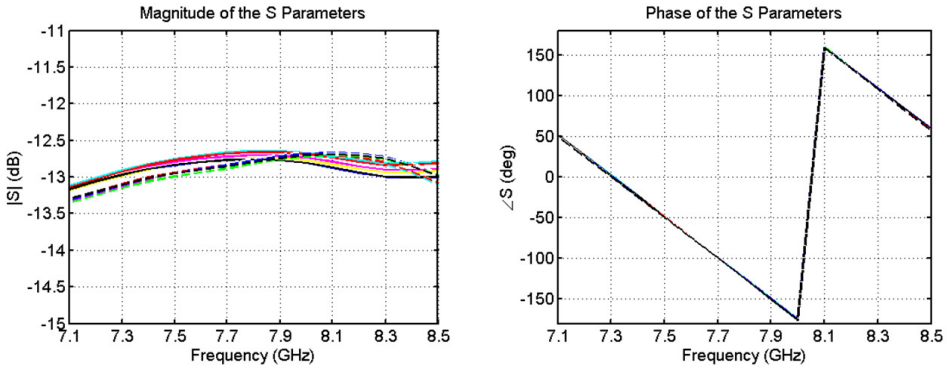

(a) **(b)**

Figure 4.24: The feed network was successful in being able to divide the input power equally into all the sixteen ports. Also, the feed network also has equiphase excitation within RX and TX.

equimagnitude amplitude coefficients, posses the largest directivity. In the Mars rover DTE requirements, side lobe levels, though can be important, are not as important as achieving high gain. Moreover, electronic beam scanning is not necessary in the Mars rover design. The beam can be mechanically steered through the use of a gimbal. Hence, a successful feed network design will depend on if equimagnitude and equiphase excitation coefficients can be maintained within the RX and TX frequencies. From the simulations as shown in Fig. 4.24, the excitation coefficients, which are represented by S_{1n} where

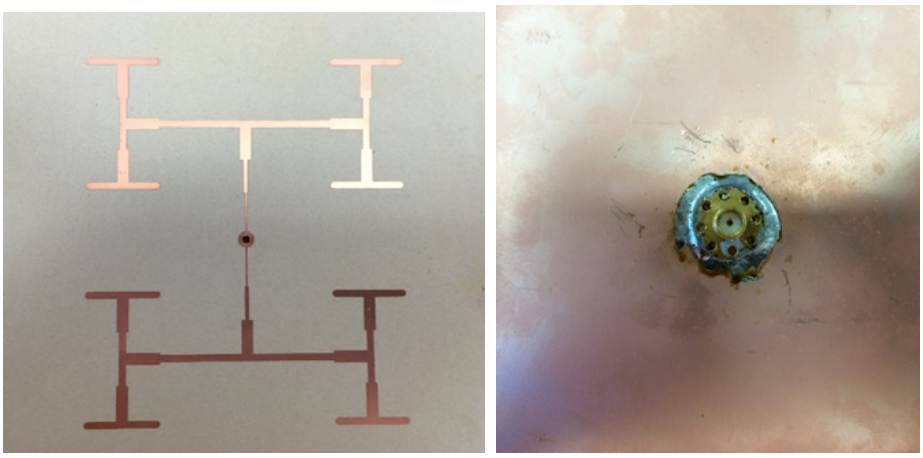

(a) Top View **(b)** Bottom View

Figure 4.25: The fabricated 4x4 subarray feed network design.

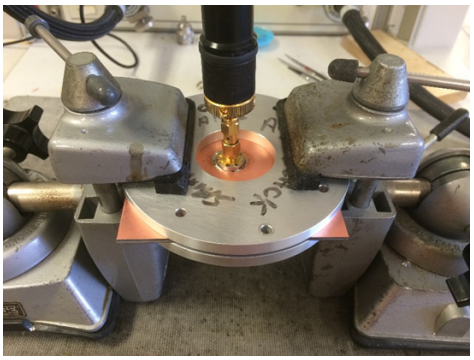

Figure 4.26: Clamps were used to connect the top and bottom ground planes of the stripline network.

n is the output port, achieve an equimagnitude response, with levels around -13 dB. This is close to the theoretical value because each output port should receive 1/16 of the original input power, which is equivalent to -12.04 dB. Another result in Fig. 4.24, is that the output ports all have equiphase responses in the RX and TX frequencies. This was primarily achieved because of the symmetry of the feed network design and the stripline to SMA connector being placed at the center of the feed network.

Now that the effect of the designed feed network has been tested using a full-wave simulation tool, the feed network was fabricated to see if the feed network was functional. The fabricated design, as shown in Fig. 4.25, used the actual layout seen in Fig. 4.22a

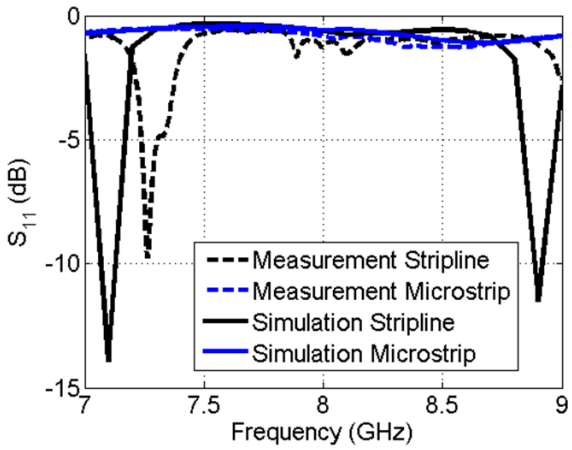

Figure 4.27: The simulation and measurements show similar results using a 4x4 subarray open circuit case for both stripline and "microstrip" scenarios.

because the simplified model would not be schematically possible because of the placement of the subarray elements. The prototype was tested without having to load all the sixteen elements. In order to do this, an open circuit case was fabricated. This offers a good way to compare if actual measurements can match simulation results. For this stripline, clamps were used in order to connect the top and bottom ground planes together. The stripline is located in the center of this configuration. From this, the S_{11} of this stripline was measured and is compared to the HFSS simulation of the open circuit case of the 4x4 feed network. A "microstrip" scenario where the the top ground plane of the stripline was removed was also considered.

From these graphs shown in Figure 4.27, the measurements were much more lossy than the simulation case, almost by about 5 dB. However, the measurements and simulation agreed for both the stripline and microstrip case. In fact, similar minimums for the stripline case for both the measurement and simulations occur within the RX frequency. The comparison shows that the feed network designed can be fabricated and provide results similar results to those of simulations.

At first, a simplified 1:16 power divider, shown in Fig. 4.22b, was simulated in HFSS to see if a 4x4 subarray can be fed uniformly with equiphase and equimagnitude character-

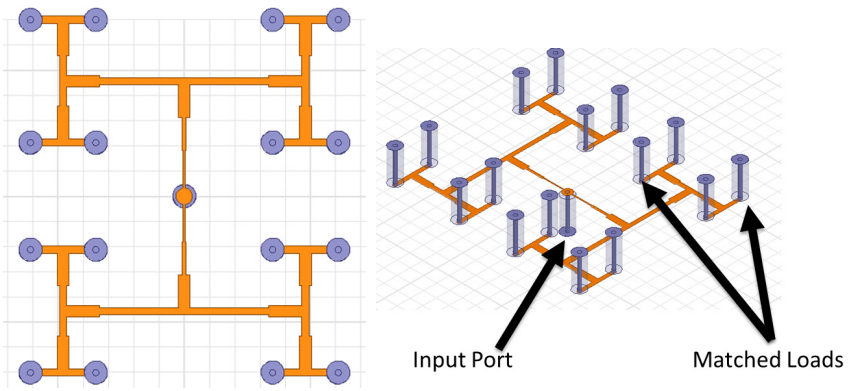

Figure 4.28: The HFSS model of the 4x4 stripline network (a) Top View (b) Side View.

istics. The results indeed showed that the simplified 1:16 stripline network had desirable S_{11} and S_{1n} characteristics. However, as was stated during the fabrication process of the 4x4 subarray feed network open circuit case, the simplified model is not a possible practical design because schematically, the elements are not placed along a line. Instead, the elements are placed as shown in Fig. 4.22a. Therefore, the proposed 4x4 feed network has to be simulated using the actual layout to show that the results are still desirable. In the actual layout seen in Fig. 4.22a, the feed point is placed at the center so that each feed point to each element is equidistant among each other. In the first stage of the power divider, a quarter transformer was designed to match 50Ω line with two parallel lines which are designed at 100Ω. In order to circumvent the use of 100Ω lines because of the their narrow line widths in the operating frequency, the quarter wave transformer, designed using equation 4.6, was placed immediately after the coaxial input in both parallel lines. This impedance is 70.7Ω. In order to retain symmetry, a 50Ω lines were placed until another quarter wave transformer designed at 35Ω to match two parallel 50Ω lines is placed for the next 1:2 power divider. This is essentially a two stage binomial transformer. After this quarter wave transformer, two 50Ω lines are again placed until a quarter wave transformer at 35Ω is placed before two more parallel 50Ω lines. This is done until 50Ω lines are placed to feed the elements at the designed element feed position. This ensures

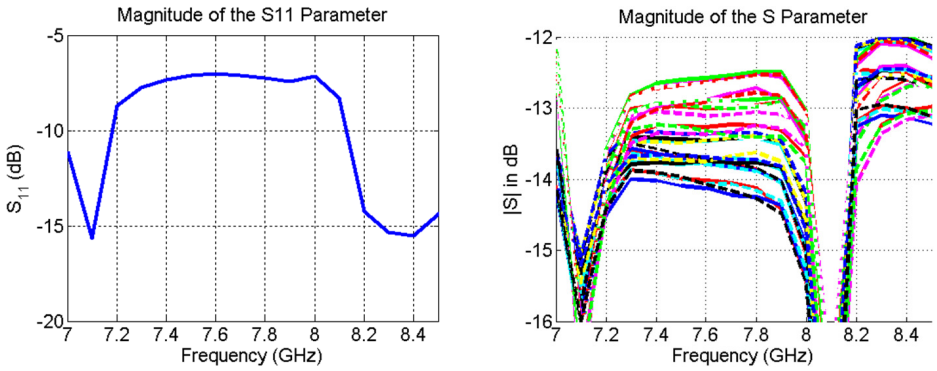

(a) (b)

Figure 4.29: The S_{11} and S_{1n} performance of the 4x4 feed network. The S_{1n} performance shows unwanted radiation at the RX band because minimum feature in 7.1 GHz and 8.1 GHz.

an symmetrical and equidistant four stage 1:16 power divider design. The impedances of the stripline were first calculated through the use of approximate solutions from [32] and is listed below in equation 4.7 where Z_0 is the characteristic impedance of the line and is set to 50Ω, b is the substrate height, ϵ_r is the relative permittivity of the substrate, W_e is the stripline width. These were tuned until good performance is met. The widths of the transmission lines with their impedances is shown also in Table 4.7.

$$Z_1 = \sqrt{Z_0 R_L} \tag{4.6}$$

$$Z_0 = \frac{30\pi}{\sqrt{\varepsilon_r}} \frac{b}{W_e + 0.441b} \tag{4.7}$$

Table 4.7: Stripline Widths Used in the Feed Network

Impedance	Width
70.7Ω	30 mils (0.08 cm)
50Ω	50 mils (0.14 cm)
35Ω	95 mils (0.23 cm)

In our first test of the feed network, a 1:16 power divider was designed with coaxial lines, shown in Fig. 4.28, at the output ports, simulating matched loads. This first design

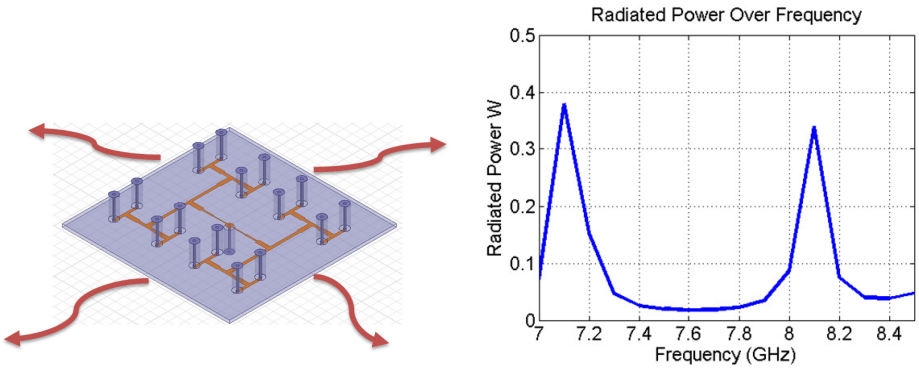

(a) (b)

Figure 4.30: From the simulations, 40% of the input power is being radiated from the stripline network.

did not include vias, which are typically used to avoid parallel plate mode excitation in striplines, because it complicates fabrication and may not be necessary. To test this, an HFSS simulation of this 1:16 divider was created to understand the S_{11}, S_{1n} performance of such a structure. In looking at the S_{11} performance in Fig. 4.29a, the required levels were achieved in both RX and TX bands. For the S_{1n} performance, the results were similar to expectations although with more variation among the sixteen ports, about 1 dB loss. However, at the RX frequency, there is about a 2 dB loss as shown in Fig. 4.29b. In fact towards the lower end of the frequency the performance worsens. The question that must be answered is where are the extra losses coming from? The particular losses are occurring at 7.1 GHz, which is the RX band, and at 8.1 GHz.

This could only mean that there is some unwanted radiation occurring from the feed network. The way this can be checked is by simulating what the radiated power is measured to be along the frequency bands. According to HFSS simulations, almost 40% of power is lost at these frequencies as shown in Fig. 4.30. When using more realistic conductivities and adding losses, more radiation is observed. Therefore, this explains the losses in S_{1n} in these frequency bands. This observation can be explained through the excitation of spurious parallel plate modes that contribute to radiation [32], especially with stripline designs.

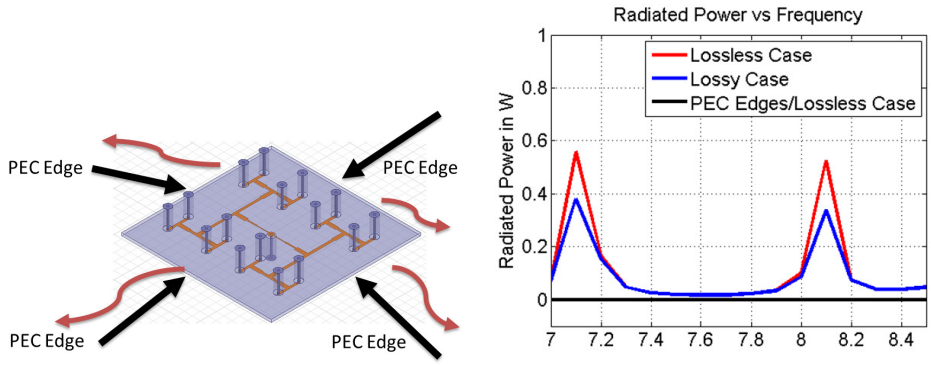

(a) **(b)**

Figure 4.31: Because the radiation is occurring at the edges, the edges were simulated as PEC to see if the radiation away from the structure can be stopped.

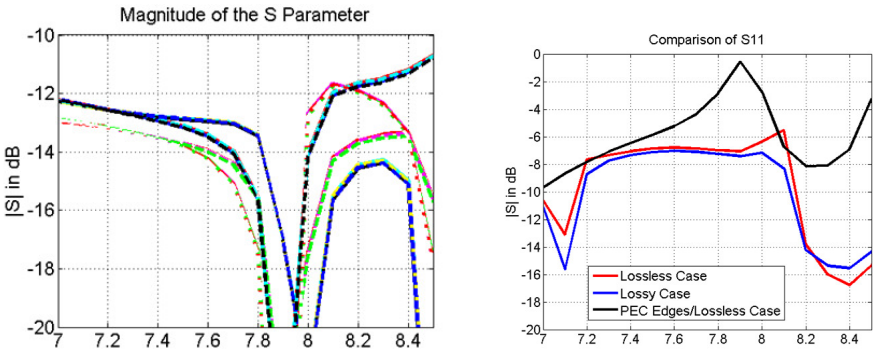

(a) **(b)**

Figure 4.32: Even though the unwanted radiation was essentially stopped by the PEC edges, the S_{11} performance worsened.

Since the radiation is occurring at the edges, the edges of the stripline network were made to be PEC so that fields cannot exit the structure as seen in Fig. 4.31a. By doing so, the radiated power is effectively decreased to 0 dB as shown in Fig 4.31b. The radiating modes could be removed through this method. However, what is the effect of PEC edges on the S_{11} and how do the S_{1n} parameters react to PEC edges? In looking at the simulations, the insertion of the PEC edges worsened the performance of both S_{11} and S_{1n} seen in Fig. 4.32. This shows that the PEC walls is not adequate in meeting required performance.

Because the excitation is a parallel plate mode, the mode comes from the potential

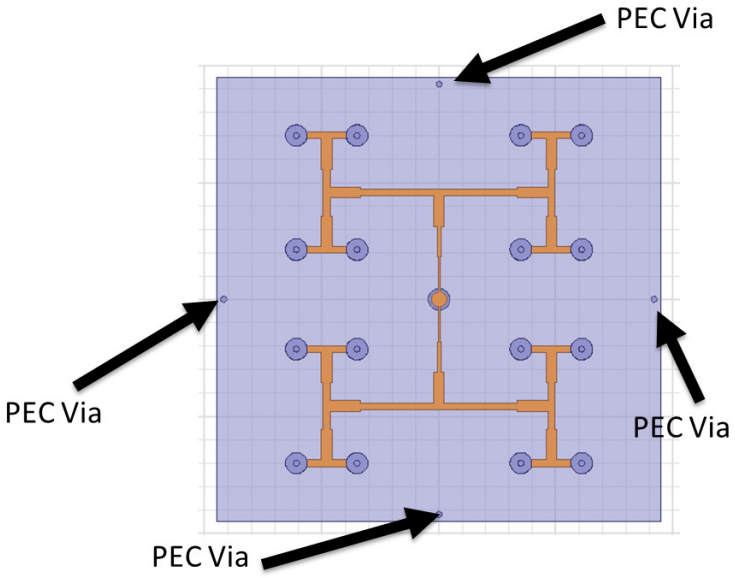

Figure 4.33: Vias were inserted into the design to remove unwanted radiation from parallel plate modes.

Table 4.8: Comparison on the S_{11} Levels When Using Vias

Magnitude of S_{11}	f = 7.15 GHz	f = 8.4 GHz
Lossy Case without Via	-12.19 dB	-15.55 dB
Lossy Case with Via	-8.14 dB	-13.71 dB

difference between top and bottom ground planes. This causes a parallel plate mode to propagate between them. One way to disrupt this propagation is by forcing the boundary conditions so that the tangential electric fields are zero, hence removing the modes. Metallic vias can be inserted to connect the two ground planes so that this mode can be suppressed. At first attempt, four vias were inserted into the structure. One via was placed at each center edge of the structure. The vias had a radius of 0.63 mm and a height of 1.63 mm. This was simulated again in HFSS, modeling the transmission line and vias with finite conductivity.

In looking at Fig. 4.34, The S_{11} levels increased by at least 2 dB in using the vias seen in Fig. 4.34a. The levels can be improved by tuning the stripline and quarter wave transformer widths to better impedance matching. The most noticeable difference was

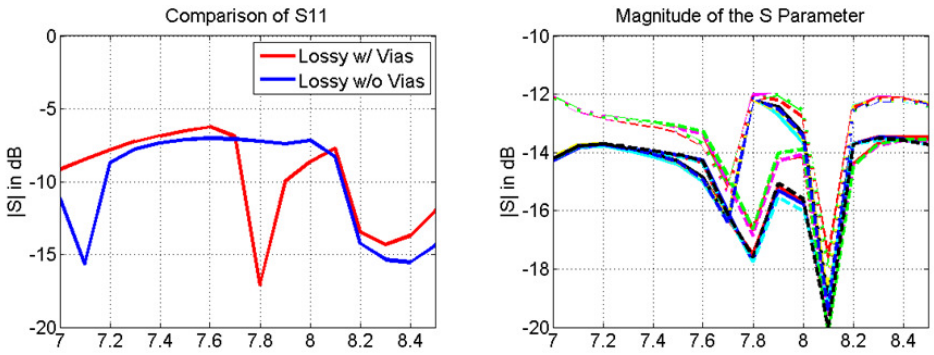

(a) **(b)**

Figure 4.34: Through the use of the vias, the S_{1n} performance was improved by 2 dB in the RX band.

Table 4.9: Comparison on the S_{1N} Levels When Using Vias

Magnitude of S_{1N}	f = 7.15 GHz	f = 8.4 GHz
Lossy Case without Via	-15.57 dB	-13.08 dB
Lossy Case with Via	-13.72 dB	-13.58 dB

in the S_{1n} performance, where the average S_{1n} performance increased by about 2 dB in the RX band shown in Fig. 4.34b. Tables 4.8 and 4.9 show the exact levels of both S_{11} and S_{1n}. This results showed that vias can help alleviate the loses due to radiation of the parallel plate mode excitation. Therefore, in order to keep eliminating the modes before they propagate, vias were placed near the coaxial input.

In practice, vias are placed along the transmission line, separated with a spacing, s, of greater than $\lambda/8$ of the highest frequency and less than the speed of light divided by twice the highest frequency $c/(2f_{max})$ to prevent a potential difference between the ground planes [44]. Therefore, the spacing was chosen to be $\lambda/6$ so that the vias are not fabricated too close to the transmission line. Moreover, only four vias were placed around the input and each of the output ports so that the amount of vias are reduced. This final proposed solution with vias was manually tuned until the desired characteristics are met.

Simulating this design seen in Fig. 4.35 with HFSS [27] yielded desired S_{11} performance for the feed network. The S_{11} levels in both RX and TX bands are more than acceptable.

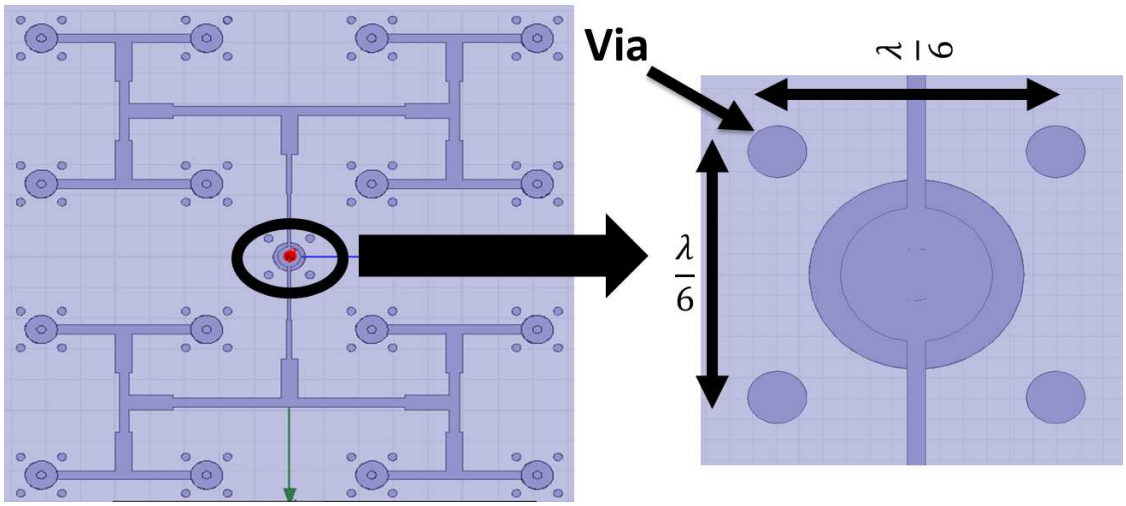

Figure 4.35: To improve the S_{11} and S_{1n} performance of the feed network, vias were placed around each output port and around the input port.

Table 4.10: S_{11} Levels With Loss Scenarios

Magnitude of S_{11}	f = 7.15 GHz	f = 8.4 GHz
Lossless Case	-13.54 dB	-20.12 dB
Dielectric Loss Only	-13.65 dB	-20.62 dB
All Losses	-14.19 dB	-20.54 dB

Table 4.11: S_{1N} Levels With Loss Scenarios

Magnitude of S_{1N}	f = 7.15 GHz	f = 8.4 GHz
Lossless Case	-12.62 dB	-12.47 dB
Dielectric Loss Only	-12.46 dB	-12.30 dB
All Losses	-12.35 dB	-12.21 dB

Again, the feed network needs to be tested to to ensure equimagnitude and equiphase characteristics are achieved in all sixteen ports. The results show decent performance. The feed nework was able to achieve nearly equivalent magnitudes, about 0.1 dB differences, are equiphase in both RX and TX frequencies.

To test the robustness of the feed network, losses are now simulated with the system to create a more realistic test. In the previous cases, losses were included into the feed network by adding the actual loss tangent of the dielectric and simulating the stripline

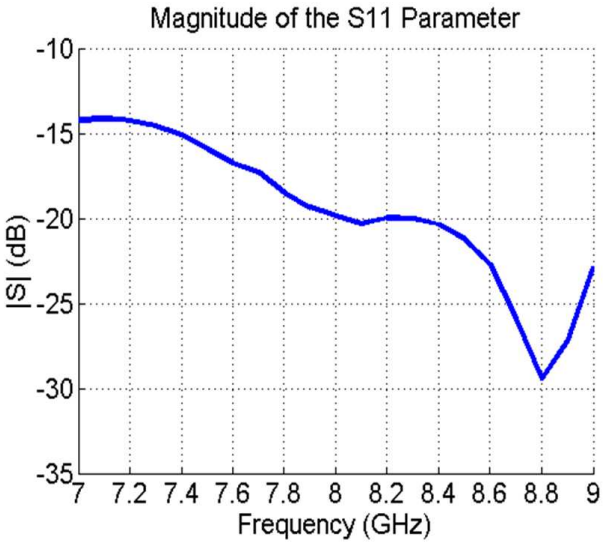

Figure 4.36: The S_{11} levels of the design with the vias around each port improved significantly, achieving desires levels.

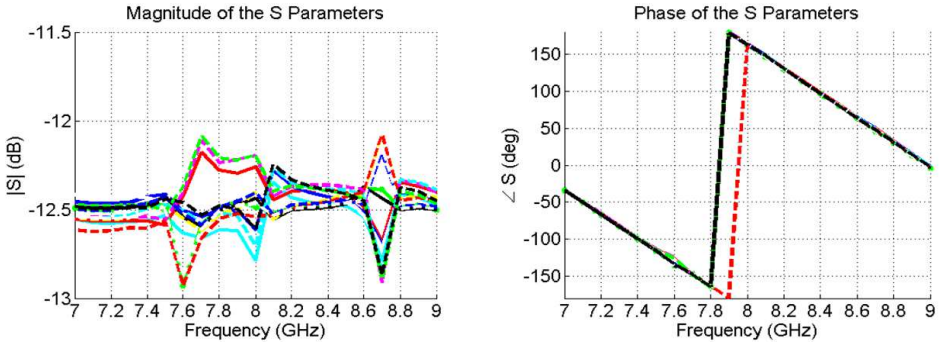

(a) **(b)**

Figure 4.37: The final design was also able to achieve equiphase and equimagnitude features.

as having some finite conductivity. In order to quantify the losses in the system, several simulations were performed. These experiment will give understanding on how the losses can affect the link budget required. This will be analyzed with both S_{11} and S_{1n} parameters. In this scenario three cases were investigated. A lossy case where the dielectric and ohmic losses were included (with finite conductivity materials including the loss tangent). Another case only involves the dielectric losses, so the ground plane and stripline were simulated as perfect electric conductors. And finally, the last case assumed all materials used were perfect electric conductors and that the dielectric did not have

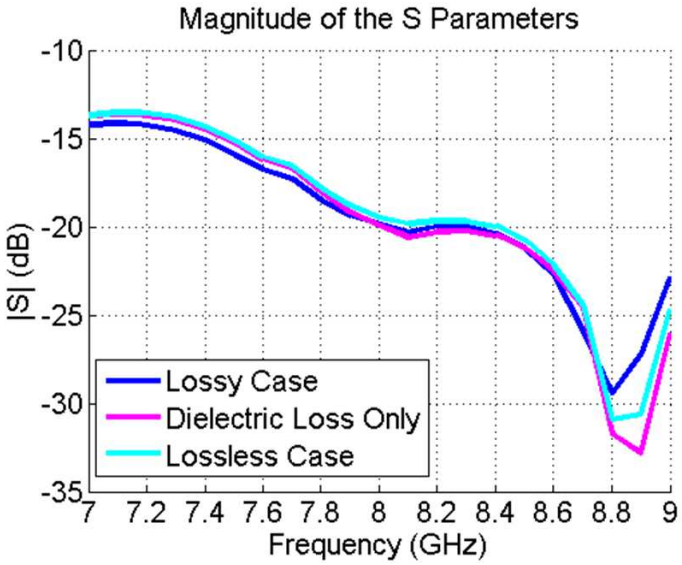

Figure 4.38: The S_{11} levels of the via design when including various losses did not vary too much from each other.

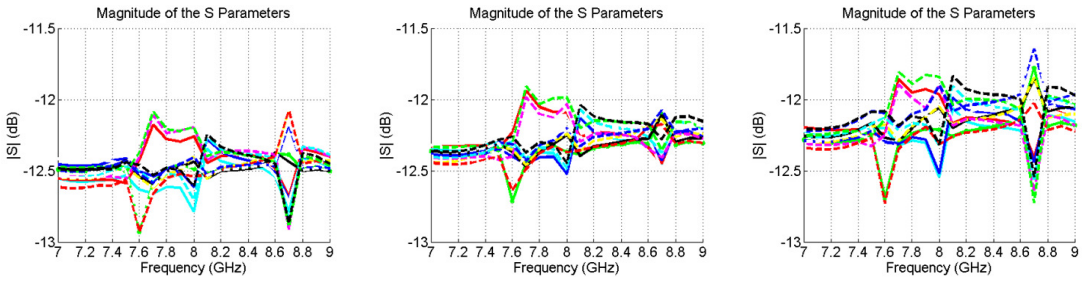

(a) **(b)** **(c)**

Figure 4.39: When adding losses into the system, the S_{1n} levels were only affected by at most, 0.4 dB.

any loss tangents.

In looking at the S_{11} performance among the loss scenario cases, the magnitude of S_{11} slightly changes as the losses are incorporated as seen in Fig. 4.38. At the RX band, the variation is about 0.6 dB and at the TX band, the variation is about 0.5 dB. The actual levels of S_{11} within the three loss scenarios are listed in Table 4.10. This improvement in S_{11} when incorporating losses shows that the more lossy the material is, more power will be absorbed by the lossy material. Similar results are shown for the S_{1n} performance seen Fig. 4.39, where the losses decrease performance about 0.26 dB at RX and 0.41 dB

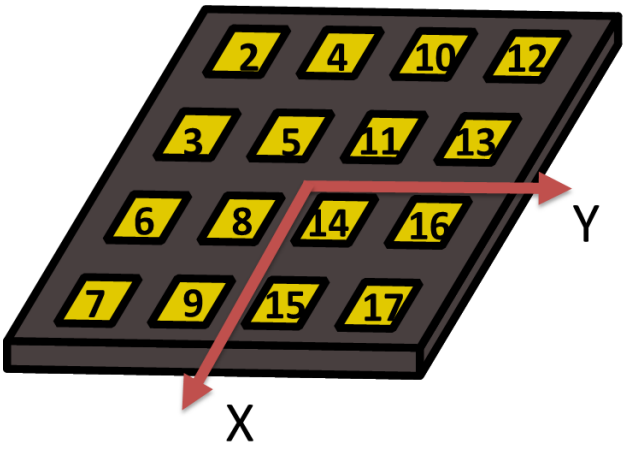

Figure 4.40: The element layout used in the UCLA DUAL program.

Table 4.12: Excitation Coefficients Achieved by the 4x4 Stripline Feed Network

	$f = 7.15$ GHz	$f = 8.4$ GHz
$S_{1,2}$	$0.235 \angle -61.8^o$	$0.238 \angle 93.3^o$
$S_{1,3}$	$0.234 \angle -61.4^o$	$0.238 \angle 93.5^o$
$S_{1,4}$	$0.235 \angle -61.6^o$	$0.238 \angle 93.1^o$
$S_{1,5}$	$0.235 \angle -60.8^o$	$0.240 \angle 93.8^o$
$S_{1,6}$	$0.237 \angle -61.3^o$	$0.238 \angle 92.5^o$
$S_{1,7}$	$0.238 \angle -61.2^o$	$0.239 \angle 93.0^o$
$S_{1,8}$	$0.239 \angle -61.2^o$	$0.240 \angle 92.5^o$
$S_{1,9}$	$0.237 \angle -61.3^o$	$0.237 \angle 92.7^o$
$S_{1,10}$	$0.236 \angle -61.5^o$	$0.239 \angle 92.9^o$
$S_{1,11}$	$0.236 \angle -60.7^o$	$0.241 \angle 93.5^o$
$S_{1,12}$	$0.236 \angle -61.4^o$	$0.240 \angle 93.2^o$
$S_{1,13}$	$0.234 \angle -61.1^o$	$0.239 \angle 93.4^o$
$S_{1,14}$	$0.238 \angle -61.3^o$	$0.240 \angle 92.5^o$
$S_{1,15}$	$0.237 \angle -61.3^o$	$0.238 \angle 92.4^o$
$S_{1,16}$	$0.236 \angle -61.5^o$	$0.238 \angle 92.5^o$
$S_{1,17}$	$0.237 \angle -61.5^o$	$0.240 \angle 92.5^o$

at TX, which is as expected. The S_{1n} levels are shown in Table 4.11. Overall, the feed network provides robust performance to meet the requirements of Mars rover system.

In previous tests, the feed network's S_{11} and S_{1n} were analyzed. The last test for the 4x4 feed network is to test its effect on directivity through the use of the S_{1n} coefficients

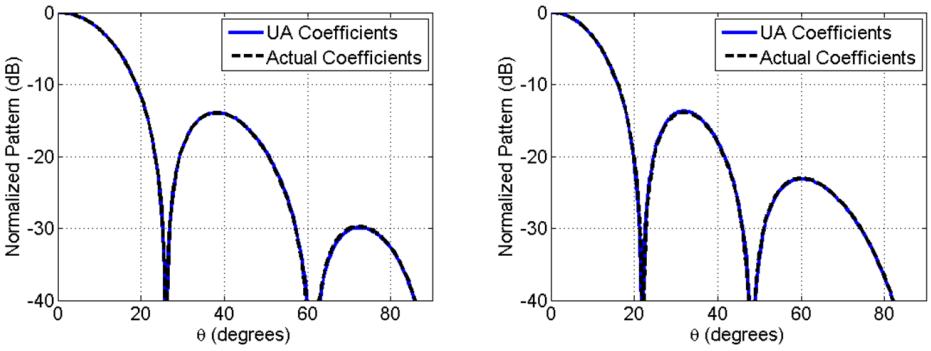

Figure 4.41: The subarray radiation patterns, $\phi = 0^o$ cut, from the excitation coefficient from the 4x4 feed network matches well with that of a subarray with uniform amplitude excitation in both RX (a) and TX (b) frequencies.

Table 4.13: Directivity Achieved Using the Excitation Coefficients from the 4x4 Stripline Network in the Subarray Environment

	$f = 7.15$ GHz	$f = 8.4$ GHz
Uniform Amplitude	18.5 dB	19.89 dB
Actual Coefficients	18.5 dB	19.89 dB

produced by the feed network. In order to test what radiation patterns and directivity is produced by these coefficients, a program called UCLA DUAL [45] will be used to perform the simulation. The UCLA DUAL program essentially calculates the directivity and radiation pattern using antenna theory based on the given excitation coefficients. As was stated before one of the reasons to require equiphase excitation is to ensure that the beam radiates towards the broadside. Because of the radiation requirements, the performance will be compared to a uniform amplitude element pattern array, which is also equimagnitude and equiphase. In theory, if the feed network can achieve as close to a uniform amplitude uniform phase array, the radiation characteristics will be met. The element layout is shown in Fig. 4.40. In looking at the excitation coefficients in Table 4.12, not only is equiphase excitation achieved, but also equimagnitude excitation. The results in Fig. 4.41 show great promise: the actual coefficients match the broadside radiation of a uniform amplitude array and in fact achieves the same directivity seen in

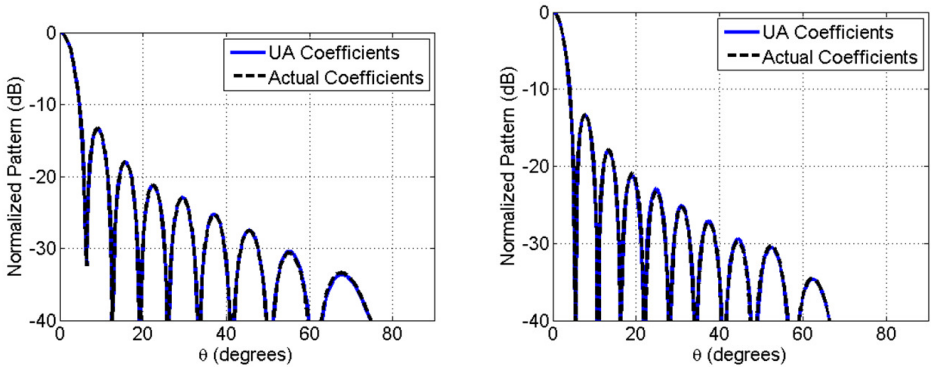

(a) **(b)**

Figure 4.42: The total array radiation patterns, $\phi = 0^o$ cut, from the excitation coefficient from the 4x4 feed network matches well with that of an array with uniform amplitude excitation in both RX (a) and TX (b) frequencies.

Table 4.14: Directivity Achieved Using the Excitation Coefficients from the 4x4 Stripline Network in the Full Array Environment

	$f = 7.15$ GHz	$f = 8.4$ GHz
Uniform Amplitude	30.24 dB	31.64 dB
Actual Coefficients	30.24 dB	31.64 dB

Table 4.13. This is comparable in both frequency bands. As was done before, the subarray was inserted into a full array environment to test if Mars rover radiation requirements are met. The excitation coefficients are used in a full array environment, therefore, the 4x4 feed network's excitation coefficients were used sixteen times in the same layout as Fig. 4.15. From the UCLA DUAL results shown in Fig. 4.42, the resulting radiation patterns from the actual excitation coefficients in both RX and TX bands still match that of the broadside pattern of the uniform amplitude array. In fact, in both bands, the directivity achieved by the 4x4 feed network matches exactly that of a uniform amplitude array seen in Table 4.14. With these results, the 4x4 feed network now has good impedance matching and radiation characteristics and can now be readily integrated with the 4x4 subarray.

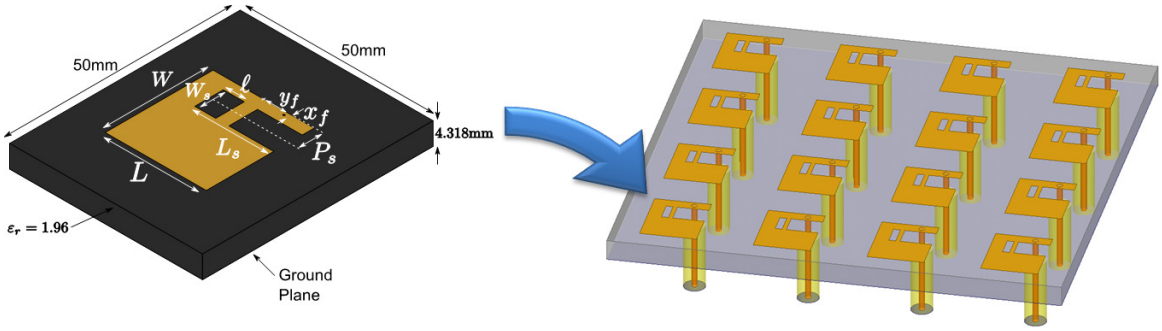

Figure 4.43: The optimized half E-shaped antenna was placed in a 4x4 subarray environment.

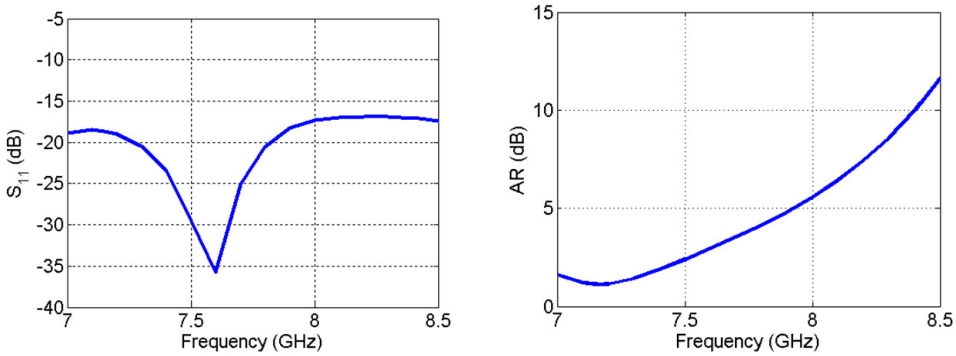

(a) **(b)**

Figure 4.44: Even though the S_{11} performance is adequate for both the RX and TX bands, the AR performance in the TX band requires further optimization within the entire subarray environment.

4.7 4x4 Subarray Using Optimized Patch Element

With the successful design of the feed network, another important aspect that must be developed is the actual 4x4 element subarray environment. Using the optimized element in the previous chapter, a 4x4 subarray topology consisting of the optimized half E-shaped patch elements was created as seen in Fig. 4.43. In this topology, each of the sixteen elements was excited with a 50Ω coaxial cable at each of the element's designated feed location. These coaxial cables is a representation of the sixteen vias that will be used to connect sixteen output ports of the 4x4 stripline feed network to the sixteen elements. This was then simulated in HFSS validate its performance [27]. In looking at the S_{11}

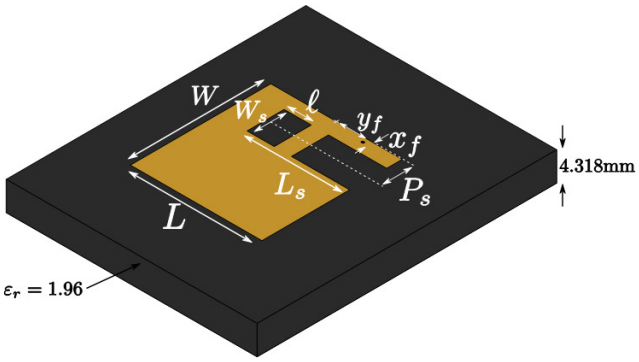

Figure 4.45: The half E-shaped antenna's parameters will be optimized within the subarray environment.

performance of the 4x4 subarray, decent levels were achieved in both RX and TX bands, well below the -10 dB limit seen in Fig 4.46a. The axial ratio performance is quite decent in the RX band. However, at the TX band, poor axial ratio levels are observed. The reason for this poor performance is because of the effect of mutual coupling in the subarray environment. Directly inserting the previously optimized element does not provide optimal performance. This can be alleviated through the use of a nature-inspired techniques, previously used for the element, to lower the axial ratio levels in this environment. In the design, Particle Swarm Optimization [28] was used to the HFSS model of the full subarray to optimized the design with the element interactions or mutual coupling in mind. The implementation of the PSO algorithm in conjunction with HFSS can be described with five steps. First, the parameters of the antenna design must be established. What this means is that the optimization engine must know which parameters of the antenna design will be optimized. Next, the optimization engine (PSO), selects the input parameters within the applicable bounds. This is where the PSO will be applied using the input boundary conditions and the position and velocity functions will be updated to reflect optimization steps. Thirdly, powerful and established computational solvers simulate the antenna performance for the given parameters. In this step, once the optimization algorithm outputs optimized parameters, HFSS was used to simulate the S_{11} and AR performance. Next, the fitness of the design is evaluated to determine if the design meets requirements. In this step, the fitness function inks the tested design to the

optimizer in order to distinguish the best design. If the requirements are not met, the third step is repeated. If the design requirements are met, the output gives the optimized antenna design solution.

The most important determination is the fitness function. The fitness functions must reflect the requirements of the design. The goals in this thesis are to develop an array with good S_{11} and AR performance at both RX and TX bands. This can be characterized by minimizing the maximum VSWR and AR of the frequency bands. The fitness function, as listed in equation 4.8, is a balance of importance between meeting S_{11} and AR goals.

$$F(\vec{x}) = \max\left(VSWR(f_{RX}), VSWR(f_{TX}), \sqrt{2}AR(f_{RX}), \sqrt{2}AR(f_{TX})\right) \tag{4.8}$$

The reason why the fitness function was formulated in terms of VSWR instead of S_{11} is because VSWR and AR are more numerically similar than S_{11} and AR. The VSWR can be related to the S_{11} as shown in equation 4.9.

$$|\Gamma| = |S_{11}| = \frac{VSWR - 1}{VSWR + 1} \tag{4.9}$$

In creating the fitness function, constraints must be added in order to retain the practicality of the design as shown in equations 4.10-4.14. This means that certain parameters must be within a certain range in order to retain the geometry and ease future fabrication of the antenna element and subarray topology.

$$L - L_s \geq 2mm \tag{4.10}$$

$$\frac{(P_s - W_s)}{2} \geq 2.5mm \tag{4.11}$$

$$\frac{(P_s + W_s)}{2} \geq W - 3mm \tag{4.12}$$

$$|y_f| \leq \frac{L}{2} \tag{4.13}$$

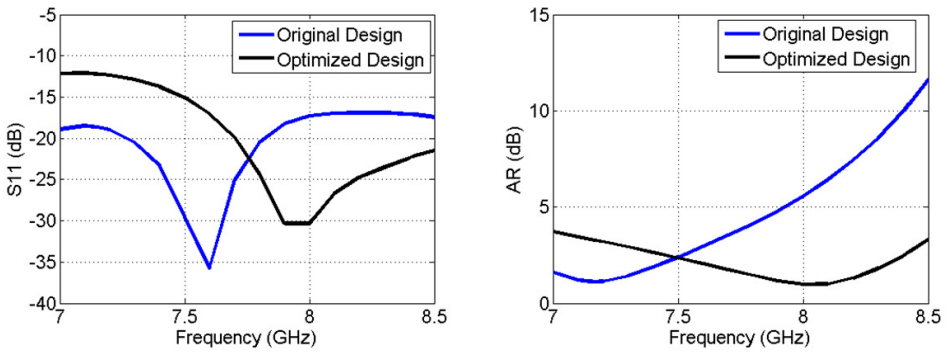

(a) **(b)**

Figure 4.46: Through the use of Particle Swarm Optimization, the axial ratio levels were lowered in the TX bands while maintaining adequate S_{11}/AR performance in both RX and TX bands.

$$L_s - l \geq 4mm \tag{4.14}$$

In order to adequately model the feed network and the entire 4x4 array, extensive computational resources are needed. To reduce computational time, we fed each element with coax and excited all elements simultaneously. Each coax is assumed to have equal magnitude and equal phase. The feed network and antenna mutual coupling effects were included through the use of a circuit model and S-matrices. Some assumptions that were made are: feed network is lossless, idealized S-parameters for the feed network at both RX and TX frequencies, and the feed network is reciprocal. Through this simplification, the feed network was excluded. However, the simulation time still was significant due to the computational volume of the array. As the results show, the optimization was successful in not only maintaining proper S_{11} levels in both RX and TX bands, but the AR levels were minimized in the TX band while remaining low in the RX band seen in Fig. 4.46. Thus, the optimization was successful in meeting Mars rover system requirements.

CHAPTER 5

Simulation and Fabrication of the X-band Subarray Antenna

5.1 HFSS Simulation of the Subarray Antenna

Each of the components for the subarray has been developed: the half E-shaped element, 4x4 subarray topology using half E-shaped elements, and the 4x4 stripline feed network. Each of these components are now going to be integrated together to form the final subarray assembly. In this chapter, the simulation of the subarray assembly, the fabrication and prototyping of the subarray, and the sensitivity analysis on the assembly will be discussed. The final specifications will be listed in the last section of this chapter.

Each of the components of the final subarray assembly have been developed in the previous chapters starting from the element to the feed network. In order to check the overall performance of the whole subarray assembly, seen in Fig. 5.1, all of these previously developed components are integrated together in HFSS. By doing so, the realized system can now be tested and tuned to meet requirements. The parameters that were tuned in this integrated assembly are the line widths of the stripline, dimensions of the patch elements, and the quarter wave transformer length. Using HFSS [27], the integrated assembly was tested to see if it is able to perform within the requirements. Looking at the results in Fig. 5.2, this integrated assembly achieved wide S_{11}/AR bandwidth. The specific levels at the frequency bands of interest are shown in Table 5.1. When looking at the radiation performance of this assembly shown in Fig. 5.3, good broadside radiation patterns were observed. In HFSS, three far field radiation characteristics can be measured

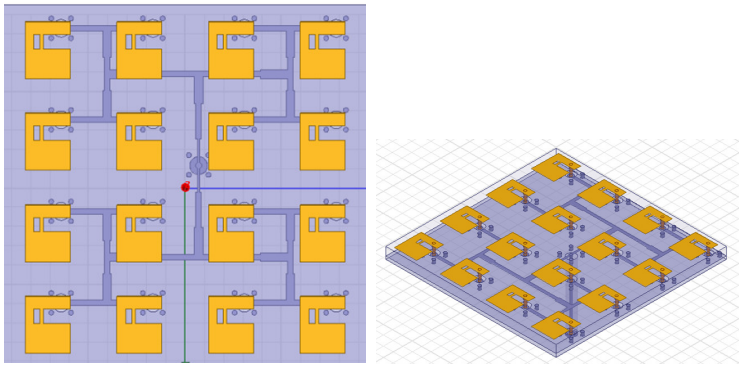

(a) (b)

Figure 5.1: All the previously designed components were integrated together to form the final subarray assembly (a) Top View (b) Side View.

Table 5.1: S_{11}/AR Simulated Performance of the Integrated Subarray Assembly

	RX (7.167 GHz)	TX (8.425 GHz)
S_{11}	-13.04 dB	-20.92 dB
Axial Ratio	2.04 dB	2.31 dB

for an antenna. HFSS defines directivity as the ratio of the radiation intensity in a given direction to the radiation intensity averaged over all the direction. Gain is defined as the ratio of the antenna's radiation intensity to the total power accepted by the antenna. Realized gain is the ratio of the antenna's radiation intensity to the total power incident upon the antenna port. These values are listed in Table 5.2. If the antenna is lossless, directivity and gain should be equivalent. In the subarray model, losses were included such as finite conductivity of the metals and loss tangent of the dielectric. Realized gain includes the S_{11} performance of the antenna [27]. In looking at these results, the realized gain, which includes S_{11} is still quite high, where losses account for about 0.35 dB in the RX band and 0.12 dB in the TX band. The radiation patterns still give decent broadside radiation and side lobe levels.

In Section 4.6, four vias were used around each port of the feed network to improve isolation and reduce unwanted radiation. This was necessary in order to reduce fabrication complexity. However, in order to see if the performance can be improved through better

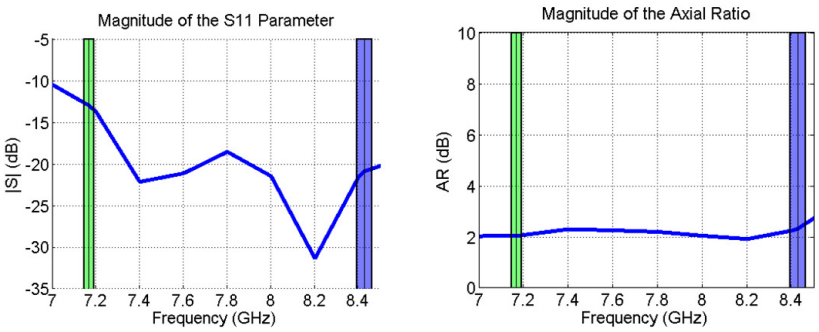

(a) **(b)**

Figure 5.2: The integrated subarray assembly's performance shows a wide S_{11}/AR characteristic.

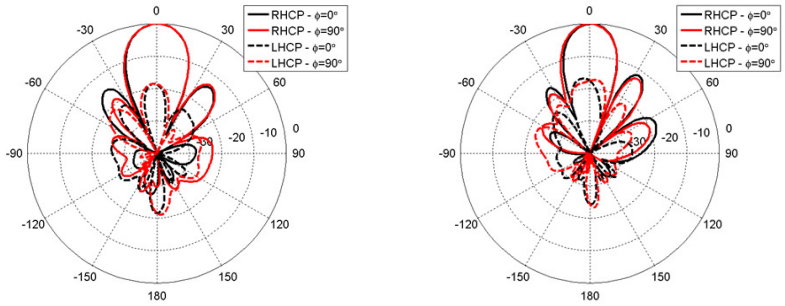

(a) **(b)**

Figure 5.3: The radiation pattern achieved by the integrated assembly achieves good broadside radiation with low cross polarization levels.

isolation and reduction of interaction among the lines, more vias were added along the transmission line path. This scenario is called the "via along the line" design seen in Fig. 5.4b. The design was simulated in HFSS to see if improvements can be made. As can be seen in the results, the original design still delivers adequate performance similar to the via along the line design In fact, the original design has a lower S_{11} level at the TX band, -20.54 dB compared to -19.76 dB as shown in Fig. 5.5a. Another important simulation was to check the radiated power levels from the stripline. Typically, by creating the via along the line design, isolation can be improved which should reduce radiated power. In fact, this was the results show in Fig. 5.5b, achieving an average of -55 dBW radiated power. This is quite low. However, a -20 dBW maximum and an average of -35 dBW radiated power for the original design is still quite low. This shows that even for the original

Table 5.2: Directivity and Gain Comparisons from HFSS Simulations and UCLA DUAL

	RX (7.167 GHz)	TX (8.425 GHz)
UCLA DUAL D_0	18.50 dB	19.89 dB
HFSS D_0	18.09 dB	19.19 dB
HFSS Gain	17.96 dB	19.10 dB
HFSS Realized Gain	17.74 dB	19.07 dB

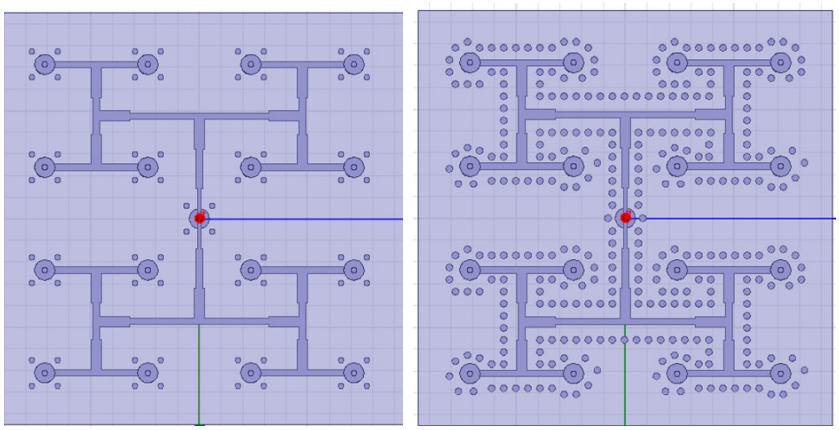

(a) **(b)**

Figure 5.4: In order to see if the performance can be improved the original design (a) is compared to the via along the line (b) design.

proposed design, the radiated power is still low and the radiation losses are small. The main difference is the S_{1n} performance. The original design exhibits a much more rough S_{1n} behavior, seen in Fig. 5.6a, over frequency. Even through this behavior, the original design still has equimagnitude response among the ports and still meets requirements. The via along the design is much more smooth over the frequency, shown in Fig. 5.6b, and is also equimagnitude at the frequency bands of interest and meets requirements. From these results, the original design is still retained in order to simplify fabrication.

To support a robust design, losses in the system are characterized. All the metallic layers in the system were set to copper with infinitesimal thickness and the vias were set to a brass material. The reason why vias was simulated as a brass material is because the actual vias that will be used in the assembly are made of brass. The brass vias are

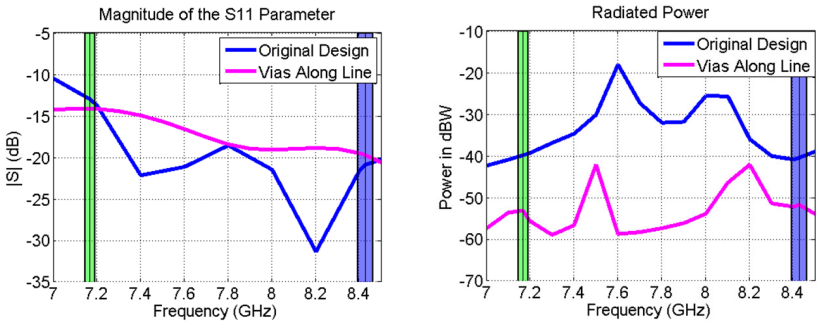

(a) **(b)**

Figure 5.5: The S_{11} (a) and radiated power (b) performance of both designs are compared. Though the via along the line offers much better impedance matching and suppression of radiated power, the original design still meets requirements.

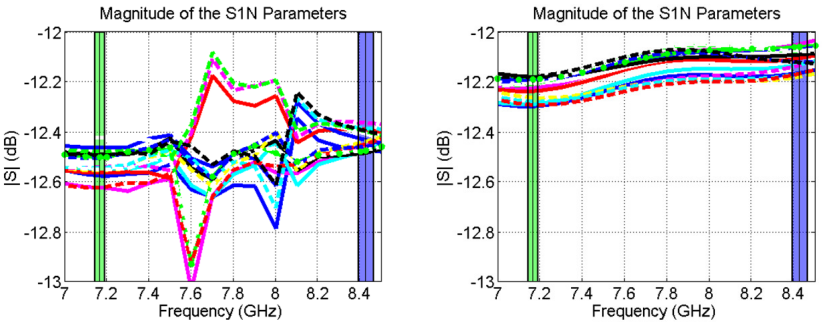

(a) **(b)**

Figure 5.6: The difference between the two designs is more apparent in the S_{1n} where the original design's, Figure 5.4a, S_{1n} (a) is much more rough over frequency versus the via along the line's S_{1n} performance (b).

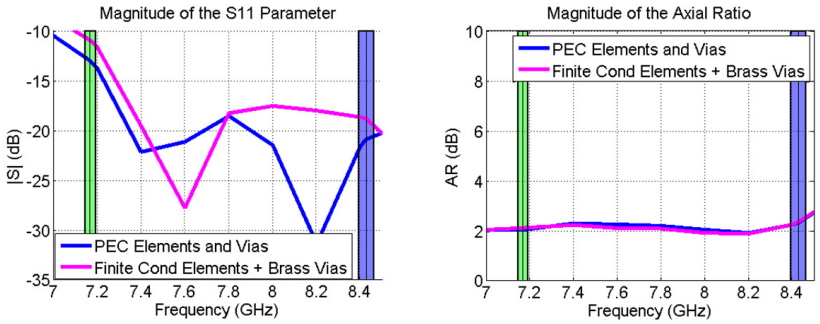

(a) **(b)**

Figure 5.7: Even with the inclusion of losses of finite conductivity and dielectric, S_{11} (a) and AR performance (b) is still adequate.

Table 5.3: S_{11} Levels at the RX and TX Bands With Losses

Magnitude of S_{11}	RX (7.167 GHz)	TX (8.425 GHz)
No Losses	-13.04 dB	-20.92 dB
All Losses	-10.99 dB	-18.86 dB

Table 5.4: AR Levels at the RX and TX Bands With Losses

Magnitude of AR	RX (7.167 GHz)	TX (8.425 GHz)
No Losses	2.04 dB	2.31 dB
All Losses	2.11 dB	2.35 dB

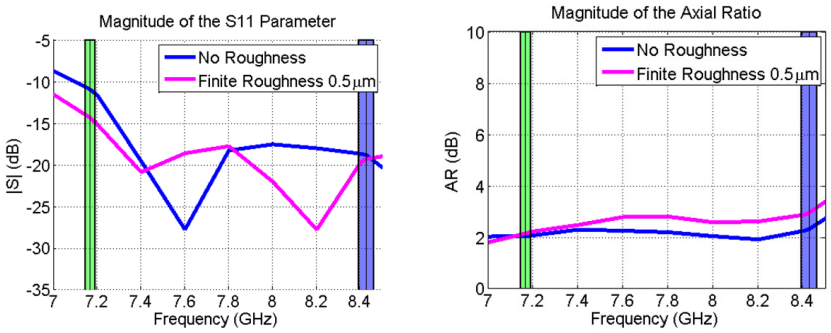

(a) **(b)**

Figure 5.8: Adding surface roughness into the model increases the AR levels at the TX band and increases S_{11} levels in both bands, but the design is still within requirements.

simulated with a radius of 0.75 mm. The results in Fig. 5.7 and Tables 5.3 and 5.4 show that lower S_{11} and AR are achieved at the TX band and higher AR magnitude in the RX band when including all the losses in the system.

In order to better quantify the effect of surface thickness in the system performance, the stripline was modified to include thickness. In HFSS, this was performed by adding a surface roughness of 0.5μm. The Groisse model was used to model this phenomenon. The results in Fig. 5.8 and Tables 5.5 and 5.6 show that the surface roughness affects the S_{11} by increasing the magnitude at the TX band by about 1.7 dB and about 1.4 dB in the RX band. The axial ratio is affected the most at the TX band, increasing the magnitude by about 0.6 dB.

Table 5.5: S_{11} Levels at the RX and TX Bands With Surface Roughness

Magnitude of S_{11}	RX (7.167 GHz)	TX (8.425 GHz)
No Roughness	-10.99 dB	-18.86 dB
With Roughness	-14.38 dB	-19.35 dB

Table 5.6: AR Levels at the RX and TX Bands With Surface Roughness

Magnitude of AR	RX (7.167 GHz)	TX (8.425 GHz)
No Roughness	2.11 dB	2.35 dB
With Roughness	2.14 dB	2.94 dB

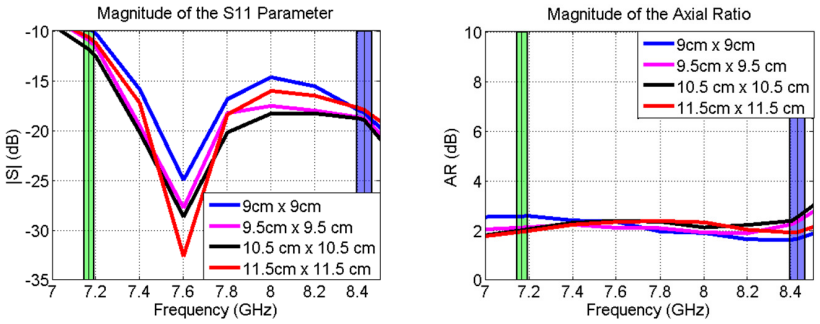

(a) **(b)**

Figure 5.9: Even with the current ground plane dimensions, S_{11} and AR requirements are achieved.

Another important test to perform is check whether the dimension of the ground plane was large enough for the subarray topology. Back lobe radiation due to diffraction may affect the directivity performance of the array if the ground plane is not large enough. In the previous designs, the ground plane was simulated to be 9.5 cm by 9.5 cm. The smallest edge to element distance of 4.89 mm is approximately equal to the height of the substrate which is 4.33 mm (170 mils). Three scenarios were used, a ground plane size of 9 cm by 9 cm, 10.5 cm by 10.5 cm, and 11.5 cm by 11.5 cm. In testing the S_{11} performance, increasing the ground plane improves the S_{11} levels in the RX band but worsens in the TX band. But even with the current size of the ground plane, the S_{11} levels were still achieved. The next performance test was done on the axial ratio. By

Table 5.7: S_{11} Levels at the RX and TX Bands with Different Ground Plane Sizes

Magnitude of S_{11}	RX (7.167 GHz)	TX (8.425 GHz)
9 cm by 9 cm	-9.80 dB	-18.25 dB
9.5 cm by 9.5 cm	-10.99 dB	-18.86 dB
10 cm by 10 cm	-11.91 dB	-18.99 dB
10.5 cm by 10.5 cm	-10.72 dB	-17.98 dB

Table 5.8: AR Levels at the RX and TX Bands with Different Ground Plane Sizes

Magnitude of S_{11}	RX (7.167 GHz)	TX (8.425 GHz)
9 cm by 9 cm	2.56 dB	1.65 dB
9.5 cm by 9.5 cm	2.11 dB	2.35 dB
10 cm by 10 cm	2.00 dB	2.53 dB
10.5 cm by 10.5 cm	1.94 dB	1.92 dB

increasing the ground plane, the AR also improves in the RX band but worsens in the TX band. Still, the current ground plane dimensions achieves requirements. As expected for the directivity, the performance worsens as the ground plane size is curtailed. In fact, the largest decrease occurs from the 9.5 cm by 9.5 cm change to 9 cm by 9 cm change. From this result, the current ground plane size is still adequately designed to meet the requirements for Mars rover communications.

5.2 Fabrication and Measurements of Prototype

Now that a final integrated design has been studied thoroughly and its performance meets required characteristics, a prototype can be assembled. In order to fabricate the prototype carefully and systematically, a procedure has been created. Therefore, the prototype was built in a manner that will be as close to the HFSS simulation as possible. These steps are listed in Appendix A. The facilities here at UCLA Center for High Frequency Electronics was used for the fabrication of the subarray using a chemical etching process.

For the measurement, a Vector Network Analyzer (VNA) was used to measure the

Table 5.9: Directivity Levels at the RX and TX Bands with Different Ground Plane Sizes

Magnitude of S_{11}	RX (7.167 GHz)	TX (8.425 GHz)
9 cm by 9 cm	17.74 dB	19.13 dB
9.5 cm by 9.5 cm	18.12 dB	19.15 dB
10 cm by 10 cm	18.41 dB	19.38 dB
10.5 cm by 10.5 cm	18.45 dB	19.66 dB

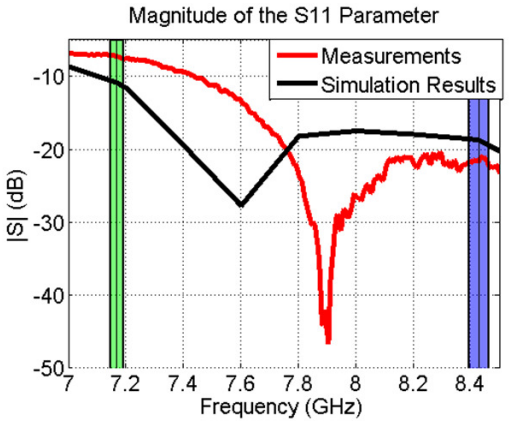

Figure 5.10: The measured S_{11} performance matches at the TX band but is about 3 dB higher on the RX band.

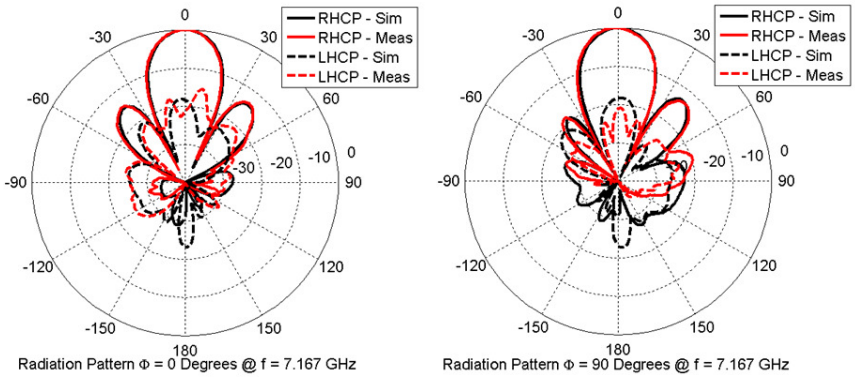

(a) **(b)**

Figure 5.11: Simulated and measured radiation patterns at both (a) $\phi = 0^o$ cut and (b) $\phi = 90^o$ cut at the RX band of 7.167 GHz.

S_{11} performance and the UCLA CHFE spherical near-field chamber was used to measure the AR, directivity, and radiation patterns. These measurements were then compared to simulation. In looking at the S_{11} measurements seen in Fig. 5.10, the results matches

Table 5.10: Simulated and Measured S_{11} Levels at the RX and TX Bands

Magnitude of S_{11}	RX (7.167 GHz)	TX (8.425 GHz)
Simulated	-10.99 dB	-18.86 dB
Measured	-7.38 dB	-21.76 dB

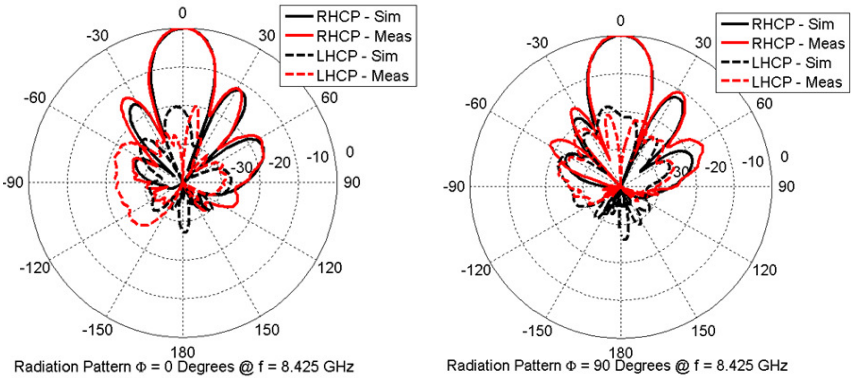

(a) **(b)**

Figure 5.12: Simulated and measured radiation patterns at both the (a) $\phi = 0^o$ cut and (b) $\phi = 90^o$ cut at the RX band of 8.425 GHz.

Table 5.11: Simulated and Measured AR Levels at the RX and TX Bands

Magnitude of AR	RX (7.167 GHz)	TX (8.425 GHz)
Simulated	2.13 dB	1.53 dB
Measured	1.53 dB	0.09 dB

Table 5.12: Simulated and Measured Directivity Levels at the RX and TX Bands

Magnitude of D_0	RX (7.167 GHz)	TX (8.425 GHz)
Simulated	18.11 dB	19.22 dB
Measured	17.85 dB	18.74 dB

well at the TX band, but it is about 3 dB higher on the RX band seen in Table 5.10. More importantly, the measured behavior of S_{11} over frequency is different of that of the simulations. Therefore additional studies may be necessary to investigate this discrepancy. For the radiation characteristics, the measured patterns in Figs. 5.11 and 5.12 match well with those of simulations. In fact, the measured axial ratio performs much better than

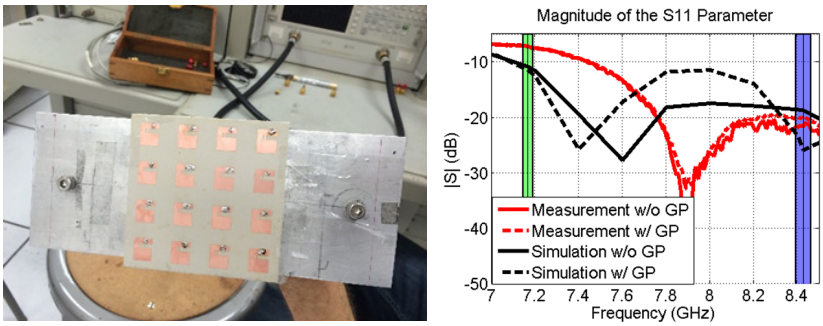

(a) **(b)**

Figure 5.13: The subarray was placed in the antenna mount to see the effect on the S_{11}.

simulated results as can be seen in Table 5.11. The directivity is well within the simulated results shown in Table 5.12. The discrepancy can mostly likely be attributed to the back lobes. Overall, the measured prototype was successful in meeting the Mars rover DTE requirements.

5.3 Sensitivity Analysis of Subarray Antenna

In the previous section, the measured radiation patterns, axial ratio, and directivity math well with simulation results and indeed meet requirements. The S_{11} level in the TX band meets requirements and is below -15 dB, but for the RX band, the measured S_{11} is about 3 dB higher than simulated. Therefore various sensitivity analysis were performed in order to understand and reconcile the differences between measured and simulated data. Some of the sensitivity analysis to be performed are: simulating a big ground plane around the prototype to match antenna mount in the spherical near field chamber, measuring actual stripline widths and including these into the simulation, including the via pin height in the stripline simulation, and combining all of these studies with the exception of the big ground plane scenario. This last case will incorporate finite conductivity, finite thickness, tolerances, and etc.

For the first scenario, the subarray prototype was attached to an antenna mount,

Table 5.13: Simulated and Measured S_{11} Levels at the RX and TX Bands for Big Ground Plane Analysis

Magnitude of S_{11}	RX (7.167 GHz)	TX (8.425 GHz)
Without Big Ground Plane	-10.99 dB	-18.86 dB
With Big Ground Plane	-7.40 dB	-26.0 dB

Table 5.14: Simulated and Measured AR Levels at the RX and TX Bands for Big Ground Plane Analysis

Magnitude of AR	RX (7.167 GHz)	TX (8.425 GHz)
Without Big Ground Plane	2.11 dB	2.35 dB
With Big Ground Plane	0.96 dB	1.27 dB

shown in Fig. 5.13a, from the spherical near field chamber. In this assembly, the S_{11} and AR were measured. The S_{11} curves are shown in Fig. 5.13b. From these results, the inclusion of the mount in the HFSS model as a larger ground plane does not have an adverse effect on the S_{11} and AR as seen in Tables 5.13 and 5.14. In fact, this verifies the previous simulation studies performed where it was observed that the ground plane does not affect the S_{11} and AR adversely. Therefore, this scenario can be ruled out as a cause of the lower S_{11} level at the RX band.

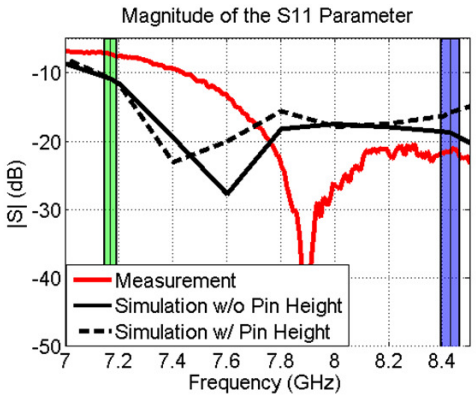

Figure 5.14: The measured S_{11} performance when including the finite via head height.

The next study to be performed is including the finite via head height into the simulations. In the actual prototype, the pin height was measured to about 6 mils. So this

Table 5.15: Simulated and Measured S_{11} Levels at the RX and TX Bands for Finite Via Head Analysis

Magnitude of S_{11}	RX (7.167 GHz)	TX (8.425 GHz)
Simulation w/ Finite Via Head Height	-10.92 dB	-15.89 dB
Measurement	-7.38 dB	-21.76 dB

Table 5.16: Simulated and Measured AR Levels at the RX and TX Bands for Finite Via Head Analysis

Magnitude of AR	RX (7.167 GHz)	TX (8.425 GHz)
Simulation w/ Finite Via Head Height	1.88 dB	1.84 dB
Measurement	1.53 dB	0.09 dB

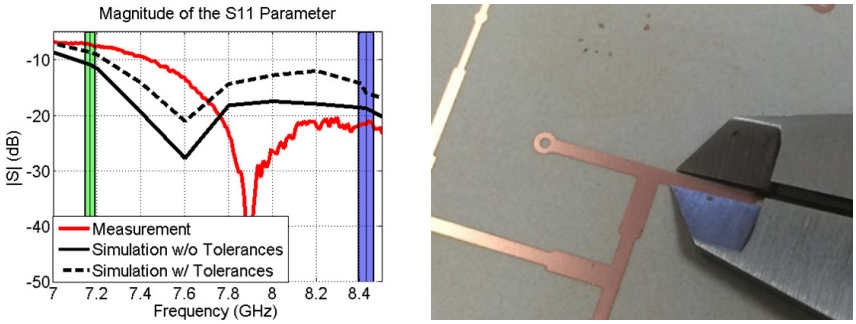

(a) **(b)**

Figure 5.15: When simulating the fabrication tolerances of the stripline, the S_{11} levels at the RX are more similar to the actual measurements.

was incorporated into the HFSS model. Again in looking at the results in Fig. 5.14 and in Tables 5.15 and 5.16, the pin height, but itself, does not have the ability to increase S_{11} levels on both frequency bands.

Another study performed is the fabrication tolerance analysis. When measuring the actual stripline widths, the width were not exactly the same length as those simulated in HFSS. The measurement of the actual stripline widths were performed using a microscope and a caliper. These measurements are shown in Table 5.17. In looking at the results in Fig. 5.15a and Tables 5.18 and 5.19, the tolerances do explain why the S_{11} deviates on the RX band and why it is lower than previously designed for. This seems difficult to

Table 5.17: Fabrication Tolerances of the Transmission Line

Line Impedance	HFSS Width	Actual Width	Difference
35Ω	90.5 mils	86 mils	4.6 mils (-4.97%)
50Ω	56 mils	48.5 mils	7.5 mils (-13.4%)
70.7Ω	32 mils	25 mils	7 mils (-21.9%)

Table 5.18: Simulated and Measured S_{11} Levels at the RX and TX Bands for Fabrication Tolerance Analysis

Magnitude of S_{11}	RX (7.167 GHz)	TX (8.425 GHz)
Simulation w/ Tolerances	-8.74 dB	-16.12 dB
Measurement	-7.38 dB	-21.76 dB

Table 5.19: Simulated and Measured AR Levels at the RX and TX Bands for Fabrication Tolerance Analysis

Magnitude of AR	RX (7.167 GHz)	TX (8.425 GHz)
Simulation w/ Tolerances	2.48 dB	1.94 dB
Measurement	1.53 dB	0.09 dB

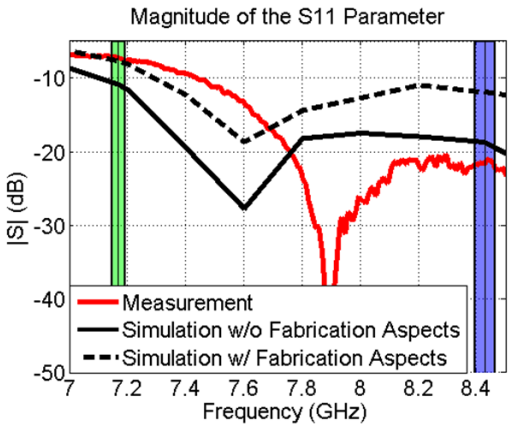

Figure 5.16: The simulated S_{11} performance when including all the losses of fabrication, via height, and conductivities.

conceptualize since the deviation seems so small. However, when looking at the percent difference, noticeable changes were made. The scenario becomes worse when every aspect of the previous sensitivity analysis was included as shown in Fig. 5.16 and Tables 5.20 and

Table 5.20: Simulated and Measured S_{11} Levels at the RX and TX Bands for All Losses Analysis

Magnitude of S_{11}	RX (7.167 GHz)	TX (8.425 GHz)
Simulation w/ All Losses	-7.82 dB	-12.01 dB
Measurement	-7.38 dB	-21.76 dB

Table 5.21: Simulated and Measured AR Levels at the RX and TX Bands for All Losses Analysis

Magnitude of AR	RX (7.167 GHz)	TX (8.425 GHz)
Simulation w/ All Losses	2.48 dB	1.51 dB
Measurement	1.53 dB	0.09 dB

5.21 . This has all the stripline width tolerances and element tolerances and the finite via pin head height. From these results, a combination of all the losses and tolerances cause a higher S_{11} level at the RX band. Therefore, this can explain why the final prototype has higher S_{11} levels at the RX band.

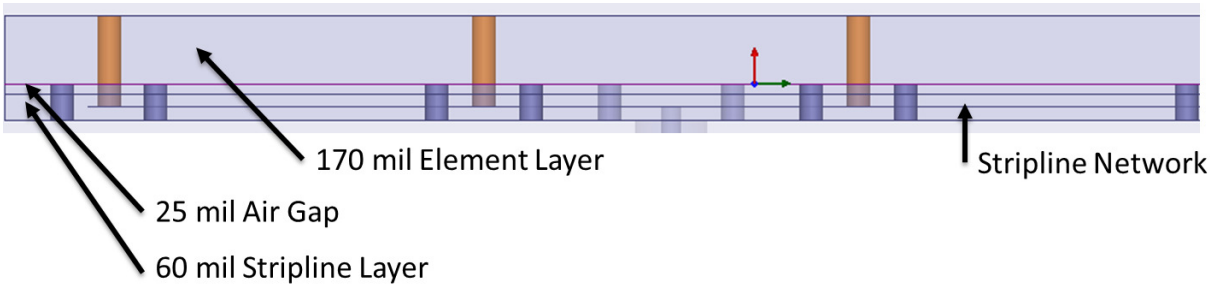

Figure 5.17: A simulation was performed to understand the effect of the air gap.

An interesting study performed was to understand the effect of the air gap on the final prototype as seen in Fig. 5.17. When assembling the prototype, finite air gaps were noticeable between the layers. In simulations, a 25 mil air gap was added to understand its effect on the performance. The results are shown in Fig. 5.18. On the TX band, the measured S_{11} level was about -21.8 dB whereas the air gap scenario yielded a S_{11} level of -21.5 dB. On the RX band, the results for the air gap are not as similar to either final prototype simulation or measured results. This may help explain why the TX band

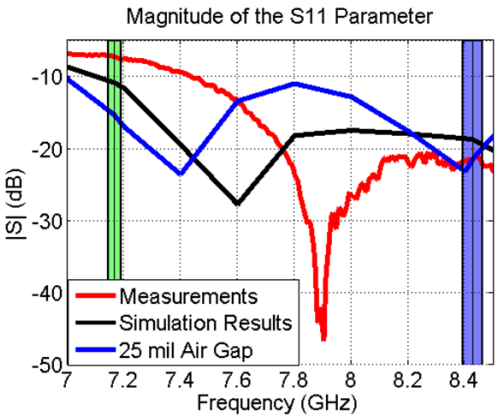

Figure 5.18: The simulated S_{11} performance of the air gap scenario when compared to simulations and measurements.

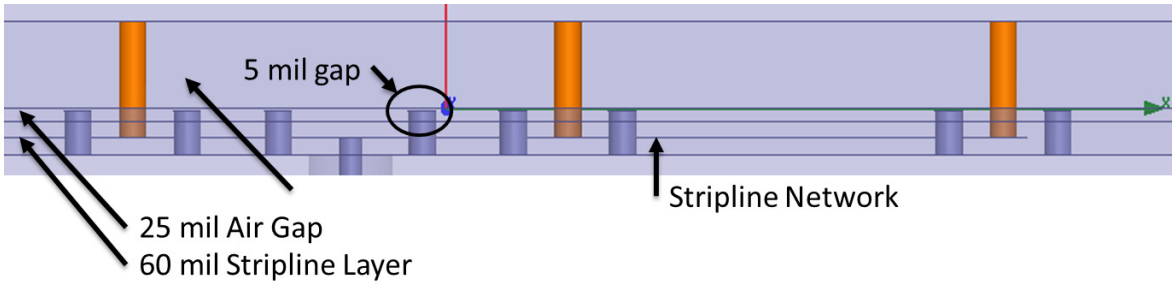

Figure 5.19: A simulation was performed to understand the effect of the air gap and via gaps.

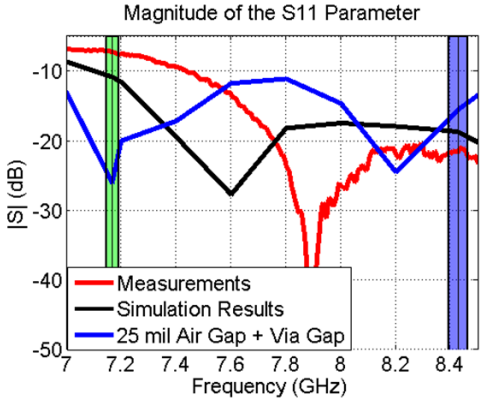

Figure 5.20: The simulated S_{11} performance of the air gap with via gap scenario when compared to simulations and measurements.

has good S_{11} even though fabrication tolerances erode S_{11} performance at the RX band. Further, another scenario as shown in Fig. 5.19 to consider is if the air gap does exist,

Table 5.22: Directivity Comparison of HFSS and NSI Calculation using MATLAB

8.425 GHz	D_0 dB	D_0 dB Front Lobe Only
HFSS Simulation	19.16 dB	19.27 dB
NSI Measurement	18.72 dB	18.84 dB

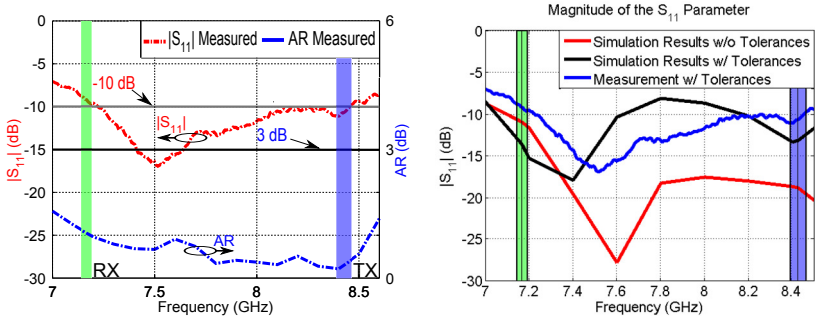

(a) **(b)**

Figure 5.21: By adding the fabrication tolerances ahead of time in the design, better S_{11} and AR performance can be achieved.

there might be a possibility that the small vias do not touch the ground plane of the element layer. In looking at the results in Fig. 5.20, the measured S_{11} level was -15.7 dB for this scenario at the TX band. This S_{11} behavior does not necessarily match either the measured or simulated S_{11} curves. Because of this, it may be probable that the 25 mil gap without the via gap scenario is much more close the actual prototype measurements.

Lastly, another investigation was made to understand why there exists a difference in directivity values from the HFSS simulation and the measured directivity. It was previously cited that perhaps the back lobes play a role in reducing the actual measured directivity. In order to verify this, measurement data in the far field was taken and was used to calculate the directivity using a MATLAB routine. In this case however, the calculation only includes the front lobe and ignores the back lobe. When comparing this with the HFSS calculation of directivity without the back lobes as shown in Table 5.22, the difference still remains.

To attempt to better the S_{11} performance of the prototyped subarray, a new subarray

Table 5.23: Final Specification of the Mars Rover Subarray

Physical Dimension	9.5 cm by 9.5 cm
Weight	2.8 oz (prototype) and 0.1 oz (connector)
Frequency of Operation	7144-7191 MHz and 8390-8460 MHz
Polarization	RHCP
S_{11}	-9.20 dB (RX) and -10.73 (TX)
AR	1.26 dB (RX) and 0.78 dB (TX)
Directivity	17.85 dB (RX) and 18.74 dB (TX)

was prototyped with the stripline widths and element tolerances included and accounted for. The new prototypes stripline widths were again measured under a microscope using a caliper. The new widths on the new prototype were much closer to the simulation widths. As can be seen in the measurement in Fig. 5.21a, the S_{11} performance is still not as good as expected. Now however, the S_{11} behavior over frequency is much more similar with simulation seen in Fig. 5.21b. Based on these results, the design is sensitive to the deviation in transmission line widths.

Because of these sensitivity analysis, the differences in S_{11} levels can be predominately explained due to the pin height of the vias in the stripline and the difference of the widths in the transmission line. Therefore, this design can be improved through more meticulous fabrication methods that could avoid these losses.

5.4 Final Prototype Specification

Overall, the second prototyped subarray closely meets requirements of the Mars rover DTE communications system. Again, the performance, especially the S_{11} can be improved through the use of more advanced fabrication methods that could minimize fabrication tolerances that can be introduced in the stripline widths and element dimensions.

CHAPTER 6

Conclusions

Mars rover Direct-to-Earth communication is an exciting new development that can maintain transfer of high volumes of scientific data from Mars to Earth in the event that orbiting relays become absent or non-existent. These orbiting relays typically have higher data rates than what DTE antennas attached on current Mars rovers offer. However, through the use of the multiband CP Half E-shaped subarray, Mars rover DTE communications may be possible. The antenna design in this scenario was complex, having to simultaneously support dual-band, high gain, high power handling, and circular polarization capabilities. In this thesis, many patch elements in literature were investigated and tested to determine their feasibility for a Mars rover DTE system. Through this exhaustive study, the CP Half E-shaped patch element was developed, containing important dual band S_{11}/AR performance in the required RX and TX bands. In addition to this, various subarray architectures were evaluated to determine if the gain requirements can be achieved. To meet this gain requirement, a 4x4 subarray topology was designed which allows a modular, scalable, and high gain design. To feed this subarray topology, a stripline feed network was developed, consisting of a binomial transformer and a four stage 1:2 power divider. This feed network supported a broadside radiation pattern for the subarray topology. These components were then integrated, first through a full wave simulation in HFSS. This rigorous study showed support for Mars rover DTE communications systems. This integrated subarray design was then fabricated and measured in the UCLA CHFE facilities where adequate performance was observed. A robust sensitivity analysis concluded that advanced fabrication methods can improve the performance

further. Overall this integrated subarray design was successful, showing dual-band, high gain, high power handling, and CP performance.

APPENDIX A

Appendix A - Fabrication Steps for the Mars Rovers Subarray Prototype

Careful and systematic steps were created in order to ease the fabrication and assembly of the X-band subarray prototype. These steps were also created in the case that replication was necessary. In this assembly, six layers exist. As shown in Fig. A.1, starting from the top layer is the element layer, then the stripline layer which has a top and bottom ground plane, and the bottom layer contains the SMA connector. The first step is to chemically etch each of the layers properly. This was done at the UCLA Center for High Frequency Electronics (CHFE). After each of the layers are fabricated, the following steps were taken to assemble the prototype. As a side note, two types of vias were used. A 62.5 mil long via was used as the via to create isolation in the stripline network and a 216 mil long via to connect the output port of the stripline network to the element feed position in the top layer.

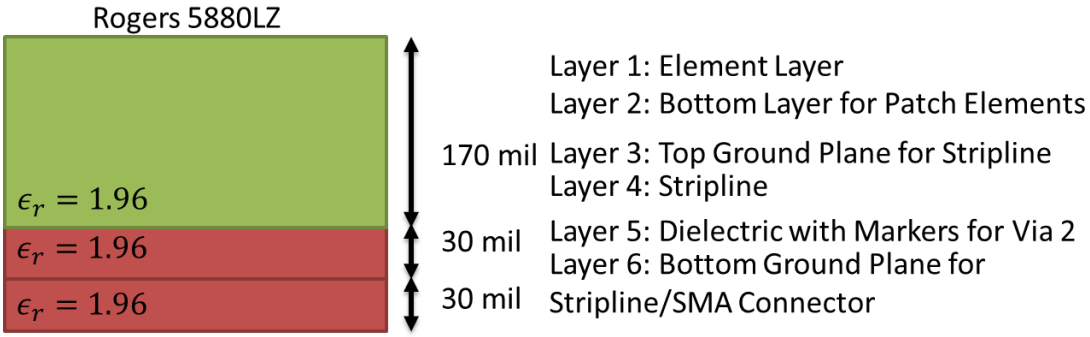

Figure A.1: The overall subarray assembly has six layers.

The first step is to drill 68 holes on layer 6 to place the 62.5 mil long via as shown

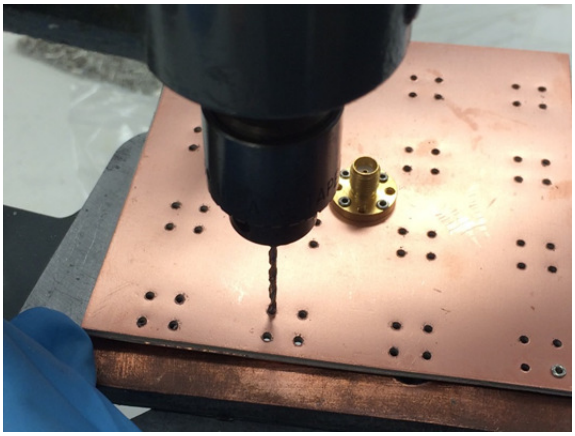

Figure A.2: Drilling the 68 holes on the bottom layer.

(a) **(b)**

Figure A.3: The via holes for the SMA and the input pin of the SMA are drilled.

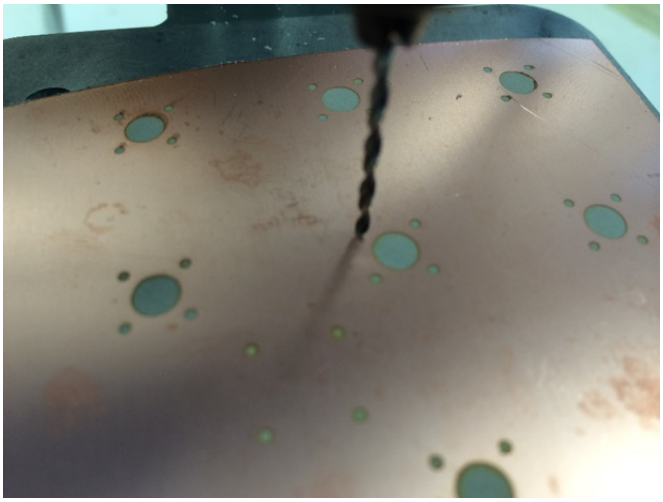

Figure A.4: Drilling the 68 holes on layer 3.

in Fig. A.2. Next, drill a hole on layer 6 to place the SMA connector seen in Fig. A.3. After this, drill 68 holes to place the smaller vias at layer 3 seen in Fig. A.4. Now, solder

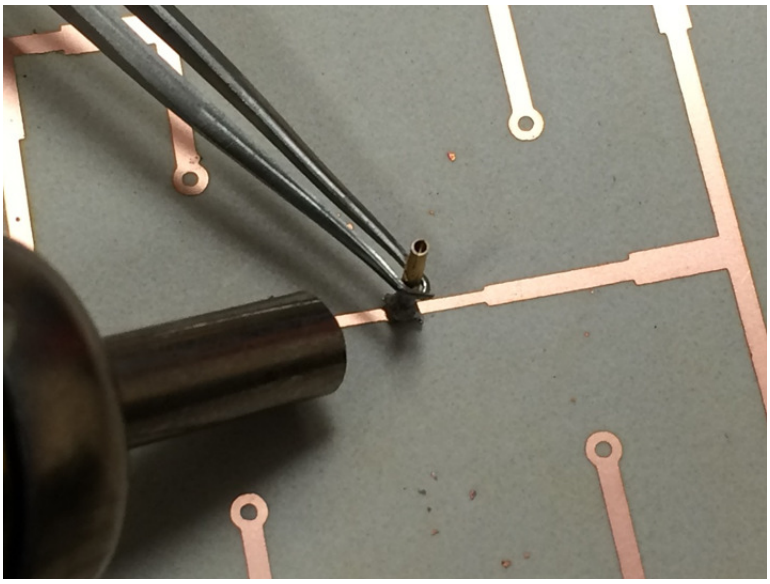

Figure A.5: Soldering the SMA pin using solder paste and hot air gun.

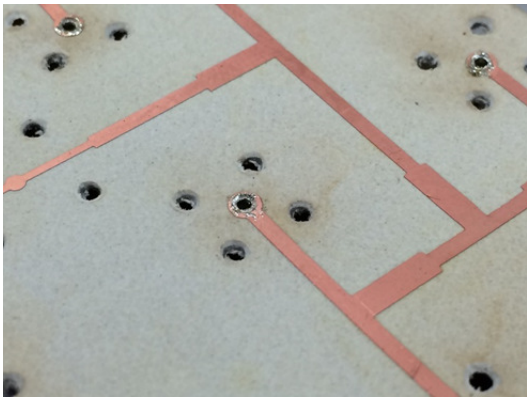

Figure A.6: Soldering the via head onto the feed network.

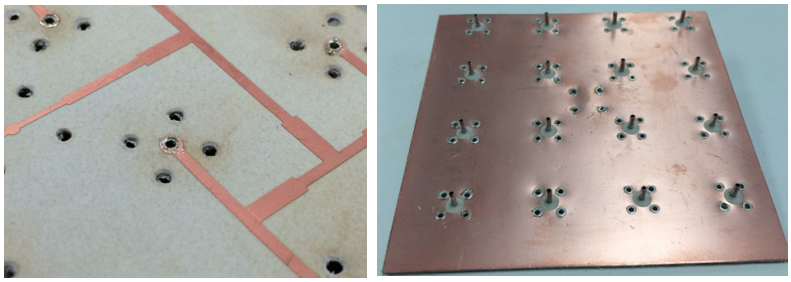

(a) **(b)**

Figure A.7: Attaching and soldering the 16 216 mil vias with the head attached on layer 4.

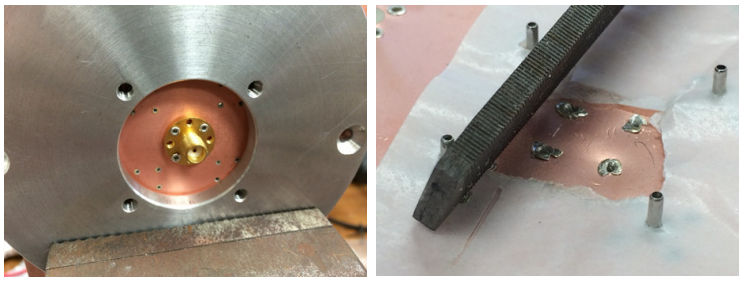

(a) **(b)**

Figure A.8: The vias were placed around the SMA connector using a clamp to remove any air gaps. The via heads were also shaved in order to retain good connection.

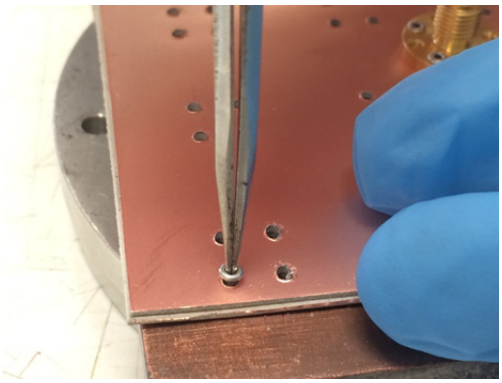

Figure A.9: Placing the small vias on layer 6.

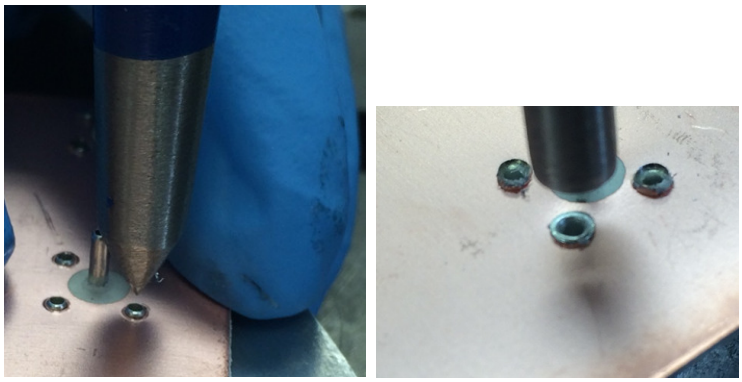

(a) **(b)**

Figure A.10: A via punch was used to flatten the vias to ensure connection with the ground plane.

the SMA pin onto layer 4 with end towards layer 6. This is shown in Fig. A.5. Using the 16 holes on the output end of the feed network, drill these holes from layer 4 for the longer vias. These holes should come out of layer 3 centered on the larger circles for use

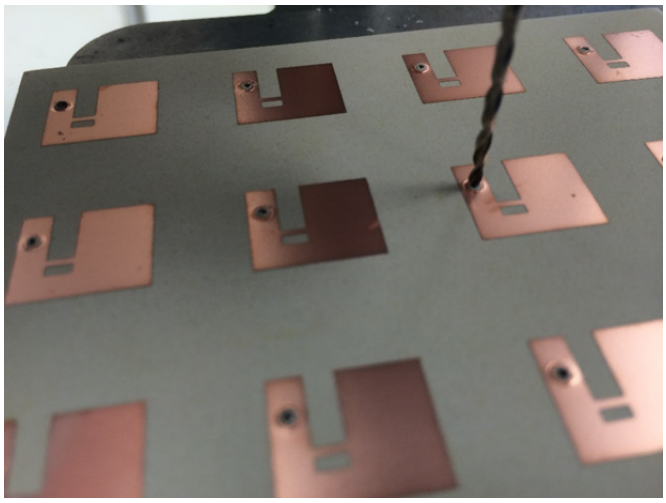

Figure A.11: Drilling holes for probe connection to feed network.

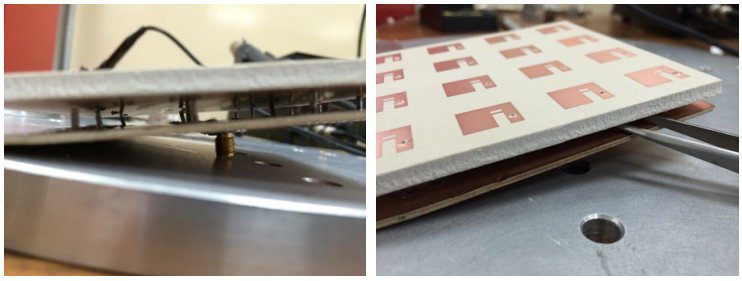

(a) **(b)**

Figure A.12: Aligning the layers can be a tedious task, so care must be exerted to align the layers properly.

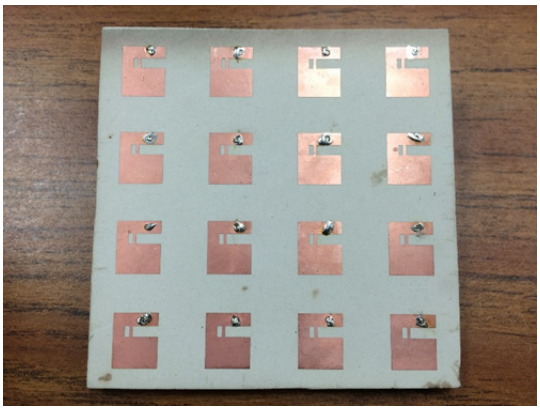

Figure A.13: The finished and assembled subarray prototype.

for the larger 216 mil vias seen in Fig. A.6. Consequently, attach and solder the 16 216 mil vias with the head on layer 4 as in Fig. A.7a. The result should look like Fig. A.7b.

Next, solder the SMA mount on layer 6. Also, place the vias around the SMA connector as shown in Fig. A.8a. On layer 4, punch down the vias and shave off as much of the head thickness so the vias are connected well seen in Fig. A.8b. The next step is to place the smaller vias. Putting the head of the vias on layer 6, place the vias in layer 6 with the end toward layer 3. This is seen in Fig. A.9. After this, a via punch was used to flatten the longer vias onto layer 3 such as in Fig. A.10. Next, from layer 1, drill 16 holes on the antenna elements based on the feed point location as can be seen in Fig A.11. Now, connect the 170 mil layer which contains layer 1 and 2 with the feed network layers which are layer 3 to 6, through use of the 16 longer vias seen in Fig. A.12. Once connected, solder the vias from the top layer. With this, the final prototype is finished, seen in Fig. A.13.

References

[1] NASA, "Technologies of Broad Benefit: Telecommunications." `http://mars.jpl.nasa.gov/mer/technology/bb_telecommunications.html`, November 2014.

[2] NASA, "How Fast and How Much Data the Rovers Can Send Back." `http://mars.nasa.gov/mer/mission/comm_data.html`, March 2015.

[3] W. J. Hurd, P. Estabrook, C. Racho, and E. Satorius, "Critical spacecraft-to-earth communications for mars exploration rover (mer) entry, descent and landing," in *Aerospace Conference Proceedings, 2002. IEEE*, vol. 3, pp. 3–1283–3–1292 vol.3, 2002.

[4] W. L. Stutzman, *Antenna Theory and Design*. Wiley, 2012.

[5] D. Hansen, M. Sue, C. Ho, M. Connally, T. Peng, R. Cesarone, and W. Home, "Frequency bands for mars in-situ communications," in *Aerospace Conference, 2001, IEEE Proceedings.*, vol. 3, pp. 3/1195–3/1208 vol.3, 2001.

[6] W. Langston and D. Jackson, "Impedance, axial-ratio, and receive-power bandwidths of microstrip antennas," in *Antennas and Propagation Society International Symposium, 2002. IEEE*, vol. 2, pp. 882–885 vol.2, 2002.

[7] C. Balanis, *Antenna Theory: Analysis and Design*. Wiley, 2005.

[8] K.-F. Tong and T.-P. Wong, "Circularly polarized u-slot antenna," *Antennas and Propagation, IEEE Transactions on*, vol. 55, pp. 2382–2385, Aug 2007.

[9] S. Bhardwaj and Y. Rahmat-Samii, "C-shaped, e-shaped and u-slotted patch antennas: Size, bandwidth and cross-polarization characterizations," in *Antennas and Propagation (EUCAP), 2012 6th European Conference on*, pp. 1674–1677, March 2012.

[10] T. Huynh and K.-F. Lee, "Single-layer single-patch wideband microstrip antenna," *Electronics Letters*, vol. 31, pp. 1310–1312, Aug 1995.

[11] Y. Ge, K. P. Esselle, and T. S. Bird, "A broadband e-shaped patch antenna with a microstrip-compatible feed," *Microwave and Optical Technology Letters*, vol. 42, no. 2, pp. 111–112, 2004.

[12] A. Khidre, K. F. Lee, F. Yang, and A. Elsherbeni, "Wideband circularly polarized e-shaped patch antenna for wireless applications [wireless corner]," *Antennas and Propagation Magazine, IEEE*, vol. 52, pp. 219–229, Oct 2010.

[13] F. Yang, X.-X. Zhang, X. Ye, and Y. Rahmat-Samii, "Wide-band e-shaped patch antennas for wireless communications," *Antennas and Propagation, IEEE Transactions on*, vol. 49, pp. 1094–1100, Jul 2001.

[14] J. Kovitz, H. Rajagopalan, and Y. Rahmat-Samii, "A novel optimized broadband reconfigurable rhcp/lhcp e-shaped patch antenna," in *Antennas and Propagation Society International Symposium (APSURSI), 2012 IEEE*, pp. 1–2, July 2012.

[15] J. Kovitz and Y. Rahmat-Samii, "Understanding the radiation pattern anomalies in the broadband cp reconfigurable e-shaped patch," in *Antennas and Propagation Society International Symposium (APSURSI), 2014 IEEE*, pp. 1580–1581, July 2014.

[16] N. Jin and Y. Rahmat-Samii, "Parallel particle swarm optimization and finite- difference time-domain (pso/fdtd) algorithm for multiband and wide-band patch antenna designs," *Antennas and Propagation, IEEE Transactions on*, vol. 53, pp. 3459–3468, Nov 2005.

[17] F. Yang, X.-X. Zhang, X. Ye, and Y. Rahmat-Samii, "Wide-band e-shaped patch antennas for wireless communications," *Antennas and Propagation, IEEE Transactions on*, vol. 49, pp. 1094–1100, Jul 2001.

[18] K.-F. Lee and K.-F. Tong, "Microstrip patch antennas: Basic characteristics and some recent advances," *Proceedings of the IEEE*, vol. 100, pp. 2169–2180, July 2012.

[19] C. Mak, K. Luk, K.-F. Lee, and Y. Chow, "Experimental study of a microstrip patch antenna with an l-shaped probe," *Antennas and Propagation, IEEE Transactions on*, vol. 48, pp. 777–783, May 2000.

[20] K. Luk, C. Mak, Y. Chow, and K. Lee, "Broadband microstrip patch antenna," *Electronics Letters*, vol. 34, pp. 1442–1443(1), July 1998.

[21] R. Chair, C.-L. Mak, K.-F. Lee, K.-M. Luk, and A. Kishk, "Miniature wide-band half u-slot and half e-shaped patch antennas," *Antennas and Propagation, IEEE Transactions on*, vol. 53, pp. 2645–2652, Aug 2005.

[22] M. T. Nguyen, B. Kim, H. Choo, and I. Park, "Effects of a cavity structure on a half e-shaped microstrip patch antenna," in *Antenna Technology (iWAT), 2011 International Workshop on*, pp. 310–313, March 2011.

[23] S. S. Yang, K. Lee, A. A. Kishk, and K. Luk, "Design and study of wideband single feed circularly polarized microstrip antennas," *Progress in Electromagnetics Research*, vol. 80, pp. 45–61, 2008.

[24] P. Hall, J. Dahele, and P. Haskins, "Microstrip patch antennas on thick substrates," in *Antennas and Propagation Society International Symposium, 1989. AP-S. Digest*, pp. 458–462 vol.1, June 1989.

[25] J. Kovitz and Y. Rahmat-Samii, "Using thick substrates and capacitive probe compensation to enhance the bandwidth of traditional cp patch antennas," *Antennas and Propagation, IEEE Transactions on*, vol. 62, pp. 4970–4979, Oct 2014.

[26] T. Brockett and Y. Rahmat-Samii, "Subarray design diagnostics for the suppression of undesirable grating lobes," *Antennas and Propagation, IEEE Transactions on*, vol. 60, pp. 1373–1380, March 2012.

[27] Ansoft, "Ansoft HFSS," 2007.

[28] Y. Rahmat-Samii, J. Kovitz, and H. Rajagopalan, "Nature-inspired optimization techniques in communication antenna designs," *Proceedings of the IEEE*, vol. 100, pp. 2132–2144, July 2012.

[29] J. Robinson and Y. Rahmat-Samii, "Particle swarm optimization in electromagnetics," *Antennas and Propagation, IEEE Transactions on*, vol. 52, pp. 397–407, Feb 2004.

[30] N. Jin and Y. Rahmat-Samii, "Design of e-shaped dual-band and wideband patch antennas using parallel pso/fdtd algorithm," in *Antennas and Propagation Society International Symposium, 2005 IEEE*, vol. 2A, pp. 37–40 vol. 2A, July 2005.

[31] R. Hall and J. Sanford, "Performance enhancements for aperture coupled microstrip antennas," in *Antennas and Propagation Society International Symposium, 1992. AP-S. 1992 Digest. Held in Conjuction with: URSI Radio Science Meeting and Nuclear EMP Meeting., IEEE*, pp. 1040–1043 vol.2, June 1992.

[32] D. Pozar, *Microwave Engineering*. John Wiley, 3 ed., 2005.

[33] N. Daviduvitz, U. Zohar, and R. Shavit, "Wide band and high gain planar array with a suspended stripline feeding network," in *Microwaves, Communications, Antennas and Electronics Systems (COMCAS), 2011 IEEE International Conference on*, pp. 1–7, Nov 2011.

[34] I. Karlsson, "Broadband microstrip array antenna," in *Antennas and Propagation Society International Symposium, 1980*, vol. 18, pp. 593–596, Jun 1980.

[35] Y. Ge, K. Esselle, and T. Bird, "Microstrip-fed e-shaped patch antennas and diversity pairs for wireless communications," in *Antennas and Propagation Society International Symposium, 2004. IEEE*, vol. 4, pp. 4152–4155 Vol.4, June 2004.

[36] S. Orfanidis, "A two-section dual-band chebyshev impedance transformer," *Microwave and Wireless Components Letters, IEEE*, vol. 13, pp. 382–384, Sept 2003.

[37] P. Sharma and K. Gupta, "Analysis and optimized design of single feed circularly polarized microstrip antennas," *Antennas and Propagation, IEEE Transactions on*, vol. 31, pp. 949–955, Nov 1983.

[38] N. Herscovici, "New considerations in the design of microstrip antennas," *Antennas and Propagation, IEEE Transactions on*, vol. 46, pp. 807–812, Jun 1998.

[39] F.-S. Chang, K.-L. Wong, and T.-W. Chiou, "Low-cost broadband circularly polarized patch antenna," *Antennas and Propagation, IEEE Transactions on*, vol. 51, pp. 3006–3009, Oct 2003.

[40] M. Manteghi, "Wideband microstrip patch antenna on a thick substrate," in *Antennas and Propagation Society International Symposium, 2008. AP-S 2008. IEEE*, pp. 1–4, July 2008.

[41] P. Hall, J. Dahele, and P. Haskins, "Microstrip patch antennas on thick substrates," in *Antennas and Propagation Society International Symposium, 1989. AP-S. Digest*, pp. 458–462 vol.1, June 1989.

[42] J. A. Ansari, S. Kesh Dubey, and A. Mishra, "Analysis of half e-shaped patch for wideband application," *Microwave and Optical Technology Letters*, vol. 51, no. 6, pp. 1576–1580, 2009.

[43] H. Rajagopalan, J. Kovitz, and Y. Rahmat-Samii, "Mems reconfigurable optimized e-shaped patch antenna design for cognitive radio," *Antennas and Propagation, IEEE Transactions on*, vol. 62, pp. 1056–1064, March 2014.

[44] Iulian Rosu, "Microstrip, Stripline, and CPW Design." `http://www.qsl.net/va3iul/Microstrip_Stripline_CPW_Design/Microstrip_Stripline_and_CPW_Design.pdf`, March 2015.

[45] R. Hoferrer and Y. Rahmat-Samii, "Ucla Dual," 1999.